

INFORMATION TO USERS

This manuscript has been reproduced from the microfilm master. UMI films the text directly from the original or copy submitted. Thus, some thesis and dissertation copies are in typewriter face, while others may be from any type of computer printer.

The quality of this reproduction is dependent upon the quality of the copy submitted. Broken or indistinct print, colored or poor quality illustrations and photographs, print bleedthrough, substandard margins, and improper alignment can adversely affect reproduction.

In the unlikely event that the author did not send UMI a complete manuscript and there are missing pages, these will be noted. Also, if unauthorized copyright material had to be removed, a note will indicate the deletion.

Oversize materials (e.g., maps, drawings, charts) are reproduced by sectioning the original, beginning at the upper left-hand corner and continuing from left to right in equal sections with small overlaps.

Photographs included in the original manuscript have been reproduced xerographically in this copy. Higher quality 6" x 9" black and white photographic prints are available for any photographs or illustrations appearing in this copy for an additional charge. Contact UMI directly to order.

Bell & Howell Information and Learning
300 North Zeeb Road, Ann Arbor, MI 48106-1346 USA
800-521-0600

UMI[®]

INFERRING FAULT RUPTURE DYNAMICS
FROM STRONG MOTION DATA

A DISSERTATION
SUBMITTED TO THE DEPARTMENT OF GEOPHYSICS
AND THE COMMITTEE ON GRADUATE STUDIES
OF STANFORD UNIVERSITY
IN PARTIAL FULLFILLMENT OF THE REQUIREMENTS
FOR THE DEGREE OF
DOCTOR OF PHILOSOPHY

Mariagiovanna Guatteri

March 2001

UMI Number: 3001996

UMI[®]

UMI Microform 3001996

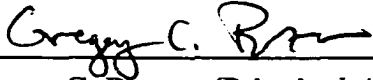
Copyright 2001 by Bell & Howell Information and Learning Company.

All rights reserved. This microform edition is protected against
unauthorized copying under Title 17, United States Code.

Bell & Howell Information and Learning Company
300 North Zeeb Road
P.O. Box 1346
Ann Arbor, MI 48106-1346

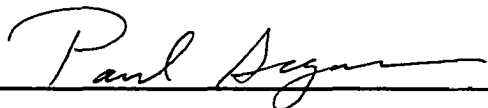
© Copyright by Mariagiovanna Guatteri 2001
All Rights Reserved

I certify that I have read this dissertation and that, in my opinion, it is fully adequate, in scope and quality, as a dissertation for the degree of Doctor of Philosophy.




Gregory C. Beroza (Principal Advisor)

I certify that I have read this dissertation and that, in my opinion, it is fully adequate, in scope and quality, as a dissertation for the degree of Doctor of Philosophy.



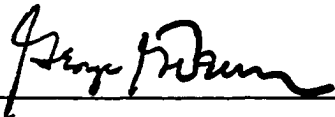
Paul Segall

I certify that I have read this dissertation and that, in my opinion, it is fully adequate, in scope and quality, as a dissertation for the degree of Doctor of Philosophy.



Paul Spudich

Approved for the University Committee on Graduate Studies:



Abstract

An inversion method is presented that combines a spontaneous rupture code and a linear programming algorithm to image earthquake rupture dynamics consistent with ground motion data. The spontaneous rupture code is converted into an inversion algorithm by imposing the slip required by the data as a boundary condition to the solution of the elastodynamics equation. The main objective of this procedure is to provide a solution of the rupture process in terms of stress and slip evolution over the fault plane through regularization of the inverse problem based on physical models of the faulting process.

This inversion procedure is used to investigate the resolution of parameters of a simple slip-weakening friction law: strength excess, $\sigma^y - \sigma^o$, and the slip distance over which the stress is released, D_c , that may be obtained from the analysis of strong-ground motions. Band-limited waveform inversion of synthetic strong motion data from a hypothetical M_w 6.5 event resembling the 1979 Imperial Valley earthquake cannot uniquely resolve both strength excess and D_c . This nonuniqueness derives from the trade-off between strength excess and D_c in controlling rupture velocity. However, fracture energy, G_c , might be relatively stably estimated from waveform inversions. If the stress drop is fixed by the slip distribution, the rupture velocity is controlled by fracture energy.

The dynamic rupture of the 1995 Kobe earthquake is investigated to determine its consistency with laboratory-derived rate and state variable friction laws. The Dieterich-Ruina friction law, with values of $d_c = 1-5$ cm for critical slip displacement, fits the stress change time series well. This range of d_c is 10-20 times smaller than D_c which previous studies have equated with the slip-weakening distance. The fracture energy for the 1995 Kobe earthquake is $G_c \approx 1.5 \times 10^6 \text{ Jm}^{-2}$, in agreement with estimates of previous earthquakes.

The effect of low absolute stress on earthquake dynamics is considered. The main difference between the dynamics of high and low stress events is the amount of coseismic temporal rake rotations occurring at given points on the fault. Temporal rake rotations can be considered low-stress phenomena and can be used as a tool to infer the initial stress (Spudich, 1992) before the earthquake initiated. Inference of low initial stress for the 1995 Kobe earthquake is presented.

Theoretical strong motion seismograms are obtained with dynamic models of hypothetical earthquakes consistent with the statistical properties of slip heterogeneity found in finite-source models of past events. These simulations show that including complexity in the rupture process consistent with dynamic rupture models has the potential to improve current strong ground motion prediction procedures.

Acknowledgements

I am deeply grateful to my advisor Greg Beroza for his support throughout my graduate school career. I have greatly benefited from his personal approach to the role of advisor, his ability to empathize with his students and the atmosphere of respect and encouragement which he fosters daily.

I owe a special debt of gratitude to Paul Spudich, who has guided me through my graduate career and was the inspiration and catalyst for most of the ideas contained in this thesis. He mentored me by generously sharing his vision, creativity and experience. I am grateful for his sense of humor for making me laugh, for his curious and humble mind for being ready to listen, and for his wisdom in guiding my decisions.

I am grateful to the members of the U.S. Geological Survey in Menlo Park where I have done most of my work while benefiting from its stimulating research environment. In particular, I wish to thank Jack Boatwright who has been a careful reviewer of all my work, offering continuous encouragement and keen insights along with generous doses of humor. Thanks also to Joe Andrews and Ruth Harris for sharing their expertise in earthquake dynamics, reviewing a number of sections of this work with insightful feedback and support. I am also grateful to Larry Baker, Howard Bundock, and Joe Fletcher for their help and patience in supporting my computing needs.

I am indebted to Paul Segall, Norm Sleep, and Mark Zoback who have always showed an encouraging interest in my research and provided numerous constructive comments and critiques. I would also like to thank the members of my examination committee (Greg Beroza, Paul Segall, Paul Spudich, Ruth Harris, and Allin Cornell) for their interest and suggestions for improving this work. I am thankful to Martin Mai for his collaboration and enthusiasm for the latest part of my work.

Thanks also to Massimo Cocco who guided my early studies in this field and who encouraged me to pursue this work at Stanford.

Many reviewers and readers have contributed to the improvement of my work. Among these, I am particularly grateful to Takeshi Mikumo, Raul Madariaga, Eichi

Fukuyama, Steve Day, Paul Okubo, Teruo Yamashita, Jim Dieterich and Michael Blanpied.

I am very grateful to my family for their constant support, love and encouragement. Thanks also to the seismo-group: Eva, Xyoli, David and Martin who have been always fun and helpful during our time working together.

This work was conducted while I was supported by the National Science Foundation (Grant EAR-9614168) and a Stanford-U.S.G.S. Fellowship.

Chapter 2, 3 and 5 were derived from papers co-authored with Paul Spudich. Greg Beroza and Paul Spudich are co-authors of work included in Chapter 4. Greg Beroza, Martin Mai and Jack Boatwright collaborated in Chapter 6. I thank S. Ide for providing his slip models used in Chapter 4 and Chapter 5 (Appendix), and T. Yoshida and D. Wald for providing their dislocation models used in Chapter 5 (Appendix).

Table of Contents

| | |
|--|-----------|
| Abstract | v |
| Acknowledgements | vi |
| Table of Contents | viii |
| List of Tables | xi |
| List of Illustrations | xi |
| Chapter 1 – Introduction | 1 |
| Chapter 2 – Dynamic Rupture Modeling and Inversion | 9 |
| Abstract | 9 |
| 2.1 Introduction | 9 |
| 2.2 What is a Dynamic Rupture Model? | 11 |
| 2.3 Inversion Method | 13 |
| Chapter 3 – What Can Strong-Motion Data Tell us About Slip-Weakening Fault-Friction Laws? | 19 |
| Abstract | 19 |
| 3.1 Introduction | 20 |
| 3.2 An Ideal Test Case | 22 |
| 3.3 Results | 25 |
| 3.3.1 Trade-off Between Strength Excess and Slip-Weakening Distance | 26 |
| 3.3.2 Apparent Fracture Energy | 27 |
| 3.3.3 Radiated Waveforms and Spectra | 27 |
| 3.3.4 Source Time Function and Rise Time | 29 |
| 3.3.5 Local Breakdown Time and Slip-Weakening Distance Resolution | 30 |
| 3.4 Discussion | 31 |
| 3.4.1 Interpretation of Previous Estimates of Slip-Weakening Distance and Strength Excess | 31 |
| 3.4.2 Implications for Resolution of Source Time Function Parameters | 32 |
| 3.4.3 How Can We Reduce the Dynamic Non-Uniqueness? | 34 |
| 3.5 Conclusions | 36 |
| Chapter 4 – Inferring Rate and State Friction Parameters from a Rupture Model of the 1995 Hyogo-ken Nanbu (Kobe) Japan earthquake | 53 |
| Abstract | 53 |
| 4.1 Introduction | 53 |
| 4.2 Rate- and State-Variable Friction | 56 |
| 4.2.1 Laboratory Observations of Friction During Dynamic Slip | 57 |
| 4.2.1.1 Critical Slip and Slip-Weakening Distance | 58 |

| | |
|---|------------|
| 4.3 Frictional Parameters from Ground Motion Data | 59 |
| 4.3.1 Overview of Ide and Takeo (1997) Results | 59 |
| 4.3.2 Our Method | 60 |
| 4.3.3 Fitting Procedure | 61 |
| 4.3.3.1 Grid Search Over d_c | 62 |
| 4.3.4 Caveats and Reliability of Stress Curves | 64 |
| 4.4 Results | 66 |
| 4.4.1 Full Model versus Simplified Model | 66 |
| 4.4.2 Critical Slip | 67 |
| 4.4.2.1 Interpretation | 68 |
| 4.4.3 $A\sigma$ and $B\sigma$ | 69 |
| 4.4.4 Apparent Fracture Energy | 70 |
| 4.4.4.1 Lower Bound for D_c | 71 |
| 4.5 Conclusions | 72 |
| | |
| Chapter 5 – The Effect of Absolute Stress on Rupture Dynamics: Modeling and Inference | 83 |
| Abstract | 83 |
| 5.1 Introduction | 84 |
| 5.2 Problem Statement | 87 |
| 5.3 Results | 91 |
| 5.3.1 Model 1 | 92 |
| 5.3.2 Model 2 | 95 |
| 5.3.3 Model 3 | 95 |
| 5.3.4 Model 4 | 96 |
| 5.3.5 Model 5 | 96 |
| 5.4 Discussion | 97 |
| 5.5 Appendix – Use of Observed Temporal Rake Rotations to Infer Tectonic Shear Stress During the 1995 Hyogo-ken Nanbu (Kobe) Earthquake | 111 |
| 5.5.1 Observational Evidence for Rake Rotations During the Kobe earthquake | 111 |
| 5.5.1.1 Striations | 111 |
| 5.5.1.2 Dislocation Models | 112 |
| 5.5.2 Method of Analysis | 113 |
| 5.5.2.1 Calculation of Stress Changes | 113 |
| 5.5.3 Results | 114 |
| 5.5.3.1 Stresses from Yoshida’s Dislocation Model | 114 |
| 5.5.3.2 Stresses from Striations on the Nojima Fault | 115 |
| 5.5.3.3 Comparison with Borehole Observations | 116 |
| 5.5.4 Implications of Low Shear Stress | 117 |
| | |
| Chapter 6 – Strong-Ground Motion Simulation with Stochastic-Dynamic Rupture Models | 125 |
| Abstract | 125 |

| | |
|--|-----|
| 6.1 Introduction | 126 |
| 6.2 Method | 128 |
| 6.2.1 Stochastic-Dynamic Rupture Modeling | 128 |
| 6.2.1.1 Stress Drop | 129 |
| 6.2.1.2 Friction Law | 129 |
| 6.2.1.3 Apparent Fracture Energy | 129 |
| 6.3 Models | 130 |
| 6.3.1 First Set of Dynamic Models | 131 |
| 6.3.2 Second Set of Dynamic Models | 132 |
| 6.3.3 Source Parameters | 132 |
| 6.3.3.1 Rupture Velocity | 132 |
| 6.3.3.2 Rise Time and Slip-Velocity Function | 134 |
| 6.4 Strong-Ground Motion Simulation | 136 |
| 6.4.1 Comparison with Empirical Response Spectral Acceleration Models | 136 |
| 6.4.1.1 Directivity Effects | 138 |
| 6.5 Discussion | 139 |
| 6.5.1 Implications for Strong-Ground Motion Prediction | 140 |
| References | 155 |

List of Tables

| | |
|---|-----|
| Table 5.1. Input Dynamic Parameters and Rake Rotation Results | 93 |
| Table 6.1. Mean Slip and Median Fracture Energy of Dynamic Models | 136 |
| Table 6.2. Summary of Modeling Approaches | 137 |

List of Illustrations

| | |
|---|-----|
| Figure 3.1. Slip-weakening friction law | 39 |
| Figure 3.2. Imperial Valley stations and faults | 40 |
| Figure 3.3. Rupture time distribution and moment rate functions for models A and B | 41 |
| Figure 3.4. Summary of dynamic and kinematic parameter distributions for models A and B | 42 |
| Figure 3.5. Slip-weakening curves for models A and B | 43 |
| Figure 3.6. Synthetic seismograms for models A and B | 44 |
| Figure 3.7. Amplitude spectra for models A and B | 45 |
| Figure 3.8. Ratio between the amplitude spectra of model A and model B | 46 |
| Figure 3.9. Slip-velocity histories for models A and B | 47 |
| Figure 3.10. Rise time distributions for models A and B | 48 |
| Figure 3.11. Local breakdown time distributions for models A and B | 49 |
| Figure 3.12. Slip-weakening distance resolution | 50 |
| Figure 3.13. Relation between strength excess, slip-weakening distance and f_{max} | 51 |
| Figure 4.1. Slip-weakening model | 74 |
| Figure 4.2. Slip distribution (Ide and Takeo, 1997) and selected subfaults | 75 |
| Figure 4.3. Stress versus slip curves at different depths | 76 |
| Figure 4.4 Procedure to select the best estimates of d_c and friction parameters (fast-weakening subfault) | 77 |
| Figure 4.5. Fitting results assuming the Dieterich model | 78 |
| Figure 4.6. Procedure to select the best estimates of d_c and friction parameters (slow-weakening subfault) | 79 |
| Figure 4.7. Estimates of d_c | 80 |
| Figure 4.8. Estimate of apparent fracture energy | 81 |
| Figure 5.1. Geometric relation between absolute stress, traction change and friction | 101 |
| Figure 5.2. Slip-weakening friction law | 102 |
| Figure 5.3. Dislocation for model 1 | 103 |
| Figure 5.4. Example of stress and slip-histories for model 1 | 104 |
| Figure 5.5. Subfaults contributing to the rake rotation at one subfault | 105 |
| Figure 5.6. Dislocation for model 2 | 106 |
| Figure 5.7. Dislocation for model 3 | 107 |

| | |
|--|-----|
| Figure 5.8. Distribution of strength parameter and dislocation for model 4 | 108 |
| Figure 5.9. Dislocation for model 5 | 109 |
| Figure 5.10. Dislocation for model with variable slip-weakening distance | 110 |
| Figure 5.A.1. Map of Njima fault on Awaji Island | 119 |
| Figure 5.A.2. Slip paths reconstructed from striations | 120 |
| Figure 5.A.3. Slip and initial stress for Yoshida et al. (1996) model | 121 |
| Figure 5.A.4. Stresses from boreholes observations | 122 |
| Figure 5.A.5. Stress magnitude vs depth from slip model, striations, and boreholes | 123 |
| Figure 6.1. Station distribution | 142 |
| Figure 6.2. Summary of dynamic simulations for models A, B, and C | 143 |
| Figure 6.3. Contours of depth-averaged slip-velocity vs time and distance along strike for models A, B, and C | 144 |
| Figure 6.4. Summary of dynamic simulations for models D1, D2, and D3 | 145 |
| Figure 6.3. Contours of depth-averaged slip-velocity vs time and distance along strike for models D1, D2, and D3 | 146 |
| Figure 6.6. Depth-averaged fracture energy for models B and D3 | 147 |
| Figure 6.7. Comparison of slip-velocity functions for models B, D1, D2, and D3 | 148 |
| Figure 6.8. Comparison of simulated and empirical average horizontal spectral acceleration | 149 |
| Figure 6.9. Comparison of simulated fault-normal component of spectral acceleration and empirical relation | 151 |
| Figure 6.10. Effect of longer rise time on simulated spectral acceleration with hybrid models | 153 |
| Figure 6.11. Effect of shorter dc on simulated spectral acceleration with dynamic model B | 154 |

Chapter 1 - Introduction

This thesis addresses the fundamental question of how to use measurements of ground motion at the Earth's surface to describe the earthquake rupture process in terms of stresses, fault frictional properties, and the governing equation of motion. Our understanding of the physics of earthquakes relies on contributions from three fundamental approaches: 1) interpretation of recorded ground motions and faulting (seismology/geodesy/geology), 2) analysis of controlled experiments on fault analogs (laboratory rock mechanics), and 3) theoretical modeling of the earthquake process. While these viewpoints have never been entirely separate, considerable insight can be gained by combining them.

Ground motion data represent the indirect physical observable of the earthquake process, and take the form of seismograms (time-series) and geodetic measurements of permanent movements of the Earth's surface. Inverse theory provides a framework to image the rupture process through minimization of the misfit between these observed data and data predicted by a model. During the past twenty years the availability and quality of ground motion recordings have noticeably improved and have correspondingly promoted an advance in seismic source imaging techniques. Nevertheless, the amount of information that we can infer from ground motion data is considerably limited by our inadequate knowledge of the forward physical theory relating the model space to the data space. A further fundamental limitation arises from the intrinsic non-uniqueness of finite-fault inverse problems, meaning that several source models can equally fit the data for a given earthquake. Traditional inversion procedures are based on a pure kinematic modeling of the rupture process in which the ground motion is mapped onto the spatial and temporal slip evolution over a prescribed fault plane, without specifically addressing questions about the physics of the rupture process. In these approaches, usually the solution is regularized by means of spatial and temporal smoothing constraints imposed on the slip history. These requirements are necessary in order to avoid a solution whose

complexity might be an artifact of the sparsity of the data set. An additional regularization based on the physics of the rupture process would add the potential to test specific ideas about the mechanics of earthquake rupture.

Complex rupture propagation and heterogeneous slip distribution are common characteristics of all dislocation models of the past earthquakes. Relating this kinematic variability to the stresses generated during rupture is fundamental to an understanding of earthquake physics. Theoretical and numerical approaches to study the earthquake process are based on spontaneous, dynamic shear-crack models (Andrews, 1976a, 1976b; 1985; Mikumo and Miyatake, 1978; Day, 1982; Das and Kostrov, 1987; Harris *et al.*, 1991). In these models the earthquake source is described as a running shear crack whose evolution is determined by the initial stress distribution, the fault frictional properties and by the governing equation of motion.

The first objective of this thesis is to develop an inverse method that provides a solution for the rupture process in terms of stress and slip evolution over the fault plane and allows regularization of the inverse problem based on physical models of the faulting process. The underlying idea of this procedure is that a spontaneous rupture code can be turned into an inversion algorithm by imposing the slip required by the data as a boundary condition to the solution of the elastodynamics equation.

The pioneering work of Quin (1990) started the effort of inferring the stress changes during real earthquakes through a *trial and error* procedure designed to match a dislocation model for the 1979 Imperial Valley earthquake by means of a spontaneous rupture calculation. Advances along this direction are provided by the work of Mikumo and Miyatake (1993), Ide and Takeo (1994) and Beroza and Mikumo (1996) based on iterative sequence of kinematic inversions and dynamic simulation to match the kinematic model. These approaches have greatly advanced our ability to image the rupture process in terms of physical parameters such as the change in stress level before and after the earthquake (stress drop), and before and after a given point on the fault starts slipping (strength excess). However these procedures are limited by the assumption of an unrealistic critical fracture criterion as the governing equation of failure process. A third type of approach (Ide and Takeo, 1997; Spudich *et al.*, 1998; Day *et al.*, 1998) derives the spatial-temporal evolution of stress parameters directly from a kinematic

model inferred from inversion of ground motion data. Unfortunately, these procedures result in a single dynamic solution, and carry all the inaccuracies and nonuniqueness of the kinematic description.

Results obtained from the application of all the aforementioned methods based on spontaneous rupture calculations suggest that the complex rupture process arises from non-uniform stress and fault strength distributions that may vary strongly for different earthquakes. Understanding the prevailing governing equation of the failure process (constitutive relation) during rupture could provide a unifying physical basis to understand the complexity of the rupture process. A constitutive relation specifies the dependence between stress, fault slip, slip rate, and other relevant physical properties.

A large number of laboratory measurements of rock friction at low sliding velocities (e.g. Dieterich, 1978; Weeks and Tullis, 1985) can be interpreted by rate- and state-variable friction laws (Dieterich, 1979; 1981; Ruina, 1983). These constitutive relations describe the evolution of frictional stress as function of slip, slip-rate, and state through coefficients depending on material and physical properties. Rate- and state-variable friction laws are capable of explaining a large range of faulting phenomena spanning the entire earthquake cycle. The critical slip displacement is related to the physical state of the fault and controls the evolution of stress toward its residual value when the fault sliding velocity is suddenly changed. A related slip parameter, the slip-weakening distance, is used to characterize a simpler constitutive relation, the slip-weakening model, used in some previous works of dynamic simulation (Ida, 1972; Andrews, 1976a, 1976b; Day, 1982). This idealized fault constitutive behavior is described also through local material properties such as fault strength and frictional stress.

At present, open questions concerning the scaling of constitutive parameters from laboratory to the field limit the application of laboratory-derived frictional laws to the rupture process of real faults. Ide and Takeo (1997) have addressed this problem with an application to the 1995 Kobe earthquake. From their calculated stress histories during rupture they inferred a slip-weakening distance up to 1 m for an assumed slip-weakening model. Following this work, Olsen *et al.* (1997) inferred a slip-weakening distance of 0.8

m for the 1992 Landers earthquake by matching a dislocation model through a *trial and error* spontaneous rupture calculation.

While these studies have made considerable progress towards investigating constitutive properties of the fault during dynamic rupture, the interpretation of their results is problematic for two main reasons. The first one concerns the validity of their estimates with respect to the actual resolution implied by the strong ground motion data set analyzed. The second reason arises from an apparent lack of consistency between their estimated values and those derived in laboratory experiments for the corresponding frictional parameters. This thesis addresses both these problems through the application of the inversion method outlined above.

The derivation of a physical model consistent with observations is an essential step toward our understanding of the physics of earthquakes; however, as the dislocation model that fits the data is nonunique, widely different dynamic models can fit band-limited data equally well. It is important to consider the resolution and stability of parameters related to fault constitutive relations when attempting to infer fault constitutive properties from observed ground motions. Building theories and drawing conclusions about earthquake mechanics can lead to useful information only if the nonuniqueness of the estimated fault properties is understood. In other words, once we derive a rupture model, we may want to ask: What other types of dynamic models can explain the observed ground motions? Are we ignoring alternative models that imply different fault properties and different rupture mechanics? Can we describe physical and frictional fault properties in terms of parameters that are uniquely linked to ground motion data? One objective of this thesis is to attempt to answer these types of questions.

The identification of specific trade-off between source parameters and competing models serves as a general guide toward an interpretation of estimated source properties. This approach should focus our efforts on general issues about earthquake physics rather than on details. For example, in a dynamic model, the speed of rupture propagation is determined by the fault resistance and by the amount of stress released. While the amount of stress released (stress drop) can be relatively stably estimated from the observations, the resistance of the fault is less easily quantified because different fault properties, such as the critical slip displacement and the fault strength, control it.

However, the value of fracture energy, defined as the energy required to create a unit area of fault by shear fracture, is determined by both these two parameters and the stress drop. Therefore, if the stress drop is known, the fracture energy can be chosen as the unique parameter representative of fault resistance and controlling rupture velocity.

While the ultimate test of a constitutive law should be its ability to model the behavior of real earthquakes occurring on real faults, results obtained from laboratory simulations of earthquakes provide the unique opportunity to interpret it in terms of known fault properties. Inconsistencies between laboratory results and parameter values derived for real faults should be investigated in an attempt to understand their origin in terms of the differences in the underlying physical process.

A simple slip-weakening model is considered a good approximation of the rate- and state-variable friction law for explaining dynamically propagating stick-slip events in the laboratory (Okubo and Dieterich, 1984; 1986). However, in order to adopt this approximation, we are urged to test whether a rate- and state- variable friction law can apply to the rupture dynamics of a real earthquake, and then we need to interpret the parameters of a slip-weakening model within the rate- and state-variable friction framework. This implies that the peak stress and the residual stress cannot be identified with material properties because they vary from place to place on a homogeneous rock sample (Okubo and Dieterich, 1984; 1986). Furthermore, the slip-weakening distance reflects physical fault properties, such as fault roughness, topography and gouge thickness (Okubo and Dieterich, 1986; Scholz, 1988; Marone and Kilgore, 1993), and is critical in controlling fault instability and the size of earthquake nucleation region (Rice and Ruina, 1983; Dieterich, 1986). How then can we reconcile the large values of critical slip proposed by dynamic rupture models of earthquakes (Ide and Takeo, 1997; Olsen *et al.*, 1997) with the values observed in laboratory experiments and their implied size of the smallest earthquake? Can we ascribe these discrepancies to specific differences in the underlying physical process? An objective of this thesis is to address these questions for a specific application to the 1995 Kobe earthquake, in an attempt to combine the different viewpoints involved in the study of earthquake physics. While it is necessary to consider how the limited resolution of ground motion inversions affects the reliability of estimated

frictional parameters, this should not completely undermine efforts to determine a unified picture of the earthquake process.

Source complexity manifests itself in various ways, and it is often impossible to isolate the causes of specific complex features. In this case, the role of theoretical simulations of earthquakes is critical to explain specific kinematic source attributes or ground motion characteristics through simple and general physical source properties. A rare opportunity to collect direct observables of ground motion is provided by striations engraved on faults during earthquakes. For a variety of events in different geological settings, the observed shape of these striations suggests that the direction of slip can change coseismically at a given position on the fault. Spudich (1992) found that this peculiar phenomenon provides an unexpected resource to infer the value of absolute shear stress before the earthquake initiated. The suggestion that temporal rake rotations are strictly interrelated to the value of initial shear stress prompts further investigation into this subject.

Previous studies of earthquake rupture dynamics (Das, 1981; Day, 1982) have specifically assumed that the value of absolute initial shear stress is high, that the initial stress level itself does not affect earthquake rupture, and therefore ground motion, and that the direction of slip does not vary coseismically. However, recent evidence suggests temporal rake rotations during the 1995 Hyogo-ken Nanbu (Kobe) earthquake (Otsuki *et al.*, 1997; Wald, 1996; Ide and Takeo, 1996; Yoshida *et al.*, 1996). This motivates a reconsideration of the initial stress usually assumed in dynamic rupture modeling in an attempt to simulate the rake rotation phenomenon and determine its relation with initial shear stress conditions on the fault. Learning about the value and characteristics of initial stress from ground motion data provides a valuable addition to the general objective of this thesis to infer fault rupture dynamics from ground motion data.

Improving our understanding of the physics of the rupture process would represent a significant step towards more realistic prediction of the intensity of ground motion in future earthquakes. The complexity of the rupture process (as revealed by finite-fault inversions) results in significant ground motion variability and affects the

level of damage, particularly in the extreme near-field of large earthquakes. A realistic prediction of the intensity of ground motion relies on our ability to generate hypothetical source descriptions consistent with our empirical knowledge of source complexity from past earthquakes. Somerville *et al.* (1998) and Mai and Beroza (1999) have recently taken some steps in this direction through an empirical characterization of slip complexity using dislocation models of past earthquakes. This approach aims to complement and improve the existing methodologies used to predict the intensity of ground motion through empirical relations (usually referred to as attenuation laws) (e.g. Abrahamson and Silva, 1997). As the severity of the strong ground motion caused by large recent earthquakes has proved to us (1994 Northridge, 1995 Kobe, 1999 Izmit), these attenuation laws are inadequate to predict strong ground motion intensity in the proximity of the source.

Slip heterogeneity, although in some respects the most important, is only one of several source attributes contributing to its complex behavior. Furthermore, spontaneous rupture simulations resulting in heterogeneous slip distribution imply corresponding inhomogeneous distribution of other relevant source parameters such as rupture velocity, rise time (the duration of slip at a point on the fault), and the shape of the slip velocity function. It is likely that the variability associated with these parameters affects the level of damaging ground motion in the proximity of the fault, and thus we must include it into generalized source models for strong ground motion prediction.

In contrast to kinematic source modeling, a dynamic description of the rupture process provides a self-consistent way of describing the variability of all the relevant source parameters without prescribing their spatial distribution a priori. Andrews and Boatwright (1998) introduced the idea of simulating far-field ground motion spectra through dynamic rupture simulations based on stress distributions generated as a random field. The final objective of this thesis is to develop this idea further through a more realistic description of the stress fields and the computation of strong motion seismograms for several realizations of scenario earthquakes at multiple observer locations. Ideally this will result in physically consistent rupture models that adequately reflect the slip heterogeneity found in finite-source models of past earthquakes.

In Chapter 2 I introduce the main ideas behind dynamic rupture modeling and describe the inversion procedure that provides a dynamic solution for the rupture process. I will present the mathematical formulation of the inverse problem and outline a set of constraints that can be applied to impose both kinematic and dynamic properties on the solution.

This inversion procedure will be applied in Chapter 3 to investigate the resolution of parameters related to fault constitutive properties that may be obtained from the analysis of strong-motions. In this chapter I address the problems that the nonuniqueness in dynamic source descriptions imply while investigating fault frictional properties from band-limited ground motion data.

Although the conclusions of Chapter 3 are not uniformly encouraging, Chapter 4 focuses on probing the consistency between laboratory-derived frictional laws and the constitutive relations implied by the analysis of strong-ground motion data. This effort aims to reconcile existing discrepancies and inconsistencies between frictional parameters derived from experiments on simulated faults and those inferred from ground motion observations. I consider a specific application to the 1995 Hyogo-ken Nanbu (Kobe) earthquake.

In Chapter 5 I focus on the dynamics of the 1995 Kobe earthquake, but with a specific look at the effect of absolute stress on the rupture process. In particular, I consider the relation between low initial shear stress on the fault before the earthquake initiated and observable coseismic temporal changes in slip direction. The Kobe earthquake is characterized by this low-stress phenomenon, and in this Chapter I infer a value of initial shear stress at given points on the fault before the earthquake.

The last chapter, Chapter 6, will turn earthquake rupture dynamic simulations into practical application for strong ground motion prediction. This chapter aims to contribute to the improvement of ground motion prediction in close proximity to large earthquakes, as traditional predictive equations (attenuation laws) are often inadequate.

Chapter 2 - Dynamic Rupture Modeling and Inversion

- 2.1 Introduction
- 2.2 What is a Dynamic Rupture Model?
- 2.3 Inversion Method

Abstract

In this chapter I introduce the main ideas about dynamic rupture modeling, and describe the inversion procedure that we have developed by combining a spontaneous rupture code and a linear programming algorithm. This inversion methodology is particularly suited to investigate and infer source rupture dynamics properties consistent with ground motion data and/or a set of constraints imposed on the solution. The versatility of the method arises from the possibility to formulate and apply several types of constraints that can include the fit of observed ground motion and the requirement that the solution satisfies given kinematic and dynamic source properties. In the following chapters I will present applications of this inversion procedure.

2.1 Introduction

The development of finite-source inverse methods has greatly enhanced our ability to image the earthquake source. These approaches determine the spatial and temporal distribution of fault slip during an earthquake using ground motion data, and have provided detailed images of seismic sources which revealed complexity and nonuniformity in the rupture behavior (Hartzell and Heaton, 1983; Beroza and Spudich, 1988; Wald et al., 1990; Beroza, 1991; Cotton and Campillo, 1995; Yoshida et al., 1996). However, these source models are parameterized by means of kinematic attributes of the faulting process (slip, rupture velocity and slip duration), without yielding direct physical insight into the causes of variations in the rupture process itself. An additional limitation of these methods arises from the intrinsic non-uniqueness of the finite-fault inverse problem, implying the existence of different descriptions of the source consistent with the data. In strong ground motion inversions, this problem is usually circumvented by just requiring the slip distribution to be spatially smooth.

In an effort to complement these kinematic inversion procedures and overcome some of their limitations, we have developed a versatile method that derives dynamic and kinematic characteristics of the rupture process from near-source seismograms and/or by imposing a set of constraints to the solution. Such procedure is particularly effective to test whether given dynamic properties of the source are consistent with observations.

Quin (1990) introduced the idea to derive a dynamic description of the earthquake source consistent with observed ground motions. Through a *trial and error* procedure, he obtained a spontaneous rupture model for the 1979 Imperial Valley earthquake that reproduced Archuleta's (1984) dislocation model consistent with observations. However, a *trial and error* approach is very inefficient and strongly depends on subjective strategies. More recently, Olsen et al. (1997) applied a similar but more efficient procedure to the 1992 Landers earthquake.

Fukuyama and Mikumo (1993), Ide and Takeo (1994), and Beroza and Mikumo (1996) have overcome the limitations of a *trial and error* approach by developing methods based on iterative sequence of kinematic inversions and dynamic simulation to match the kinematic model. Their goal was to determine the distribution of stress drop (the difference between initial and final stress) and strength excess (the difference between the peak stress at the onset of slip and the initial stress) that yield slip and rupture time distributions consistent with observed ground motions as a spontaneous rupture process. However, these procedures a specific fracture criterion is assumed in the dynamic simulation, so at a given point on the fault the behavior of stress is specified a priori.

A third type of approach (Ide and Takeo, 1997; Spudich et al., 1998; Day et al., 1998) derives the spatial-temporal evolution of stress parameters directly from a kinematic model inferred from inversion of ground motions data. With this procedure it is possible to derive the temporal evolution of stress at a given point and the relation between stress and slip and/or slip velocity. However, the stress distribution obtained depends completely on the kinematic parameterization assumed in the inversion, on which dynamic constraints cannot be directly imposed.

The method that we have developed can be easily adapted to work as any of the procedures listed above and can combine their strengths and advantages for different goals.

2.2 What is a Dynamic Rupture Model?

Dynamic descriptions of the earthquake source are based on models that satisfy the elastodynamics equation with a prescribed fracture criterion (Andrews, 1976; 1985; Mikumo and Miyatake, 1978; Day, 1982; Das and Kostrov, 1987; Harris et al., 1991). In the framework of fracture mechanics, an earthquake may be considered as a dynamically running shear crack that radiates seismic waves. The resulting motion (slip history) on the fault is related to a drop in shear stress. Its evolution depends on the failure criterion, the constitutive properties and the initial conditions on the fault surface. In contrast, kinematic models of the seismic source (for example Haskell, 1964) prescribe their displacement history of motion a priori, without an explicit attempt to investigate the physical causes of the rupture process.

Our inversion method uses a dynamic approach for the modeling and parameterization of the seismic source. It is based on the boundary integral (BIM) spontaneous rupture code (Boatwright and Quin, 1986; Das and Kostrov, 1987; Quin and Das, 1989) that was incorporated into an inversion procedure by Spudich and Boatwright (1990) and Guatteri and Spudich (1996).

In the following section we briefly introduce the main ideas underlying dynamic modeling and describe the method to calculate spontaneous rupture. A more detailed description can be found in Guatteri and Spudich (1998) [chapter 3]. In this method a shear crack lies in the plane $x_3 = 0$ in a Cartesian coordinate system. Let us discretize the crack plane onto a rectangular grid at locations ij (subfaults) and let the k -th time step be t_k . Let $u_{\alpha ij k}$ be the α -component of slip of the crack face at location ij and time step k , and let $\tau_{\alpha ij k}$ be the α -component of stress change at location ij and time step k caused by motions on the fault. The motions of the crack face at time step k is determined from stresses on the fault at previous time steps by:

$$u_{aijk} + \Delta t G_o \tau_{aijk} = L_{aijk} \quad (2.1)$$

where Δt is the time step $t_{k+1} - t_k$ and $\Delta t G_o$ is the compliance of the medium (Andrews, 1985). L_{aijk} is the "load" (Andrews, 1985), and it is the dynamic quantity that includes the contribution to slip caused at time step k by stress changes at *previous* time step. Equation 2.1 is the "unloading curve", which relates stress change to total slip at time step k , depending on the load exerted on point ij . Given a particular value of load L_{aijk} , several pairs of stress change τ_{aijk} and slip u_{aijk} can satisfy equation 2.1; stress change and slip are uniquely specified only when a boundary condition is specified. In forward dynamic modeling this boundary condition is given by the assumed constitutive relation (or failure criterion) relating slip, slip-velocity, stress, and any other relevant physical quantities. Therefore, the slip and stress change that occur at a point on the fault at time step k are given by the intersection of the unloading curve and the curve that parameterizes the constitutive relation. The forward calculation proceeds by looping over all points on the fault for each time step, and for each fault point it determines the intersection of the unloading curve and the assumed friction law.

We modified the BIM to include approximately the effects of a vertically heterogeneous velocity structure and a free surface reflection. We loosely followed the procedure of Quin (1990). The effect of vertical heterogeneity was included by multiplying the halfspace Green's functions by the ratio of impedances at the source and receiver locations. In addition, because in the BIM the subfault dimension is fixed to be the distance a P wave travels in 2 time steps, the actual vertical extent of each subfault varies with depth proportional to P velocity. To account for the free surface reflection we added the contribution of an image source to the halfspace Green's functions. Our implementation of the approximations performed better than that of Quin (1990), and we checked it through comparisons with finite-difference calculations.

2.3 Inversion Method

We convert the spontaneous rupture code into an *inversion* algorithm based on the idea that, rather than a completely specified constitutive law, we can impose the slip that satisfies other desired constraints as boundary condition to equation 2.1, and solve this equation for the stress change consistent with the calculated value of load. In this way we find the slip and stress change that must occur at each time step in order to satisfy a given set of desired properties. At each point on the fault, the load $L_{\alpha ij k}$ is determined from stress changes at previous time steps, according to equation 1 in Guatteri and Spudich (1998) (Chapter 3, equation 3.1). For the first time step the load is zero.

Let s be the subfault corresponding to the indices ij , and let us assume isotropic friction. This assumption means that the slip velocity is collinear with total traction (friction), so that the slip direction is predetermined at each time step. Therefore, we can remove the slip direction parameter (the index α in equation 2.1) from the problem, and for subfault s and time step k define the slip increment $\Delta u_{s k}$ along the direction determined by the total traction vector. We use a linear programming algorithm to solve for the slip increments $\Delta u_{s k}$ for the set of subfaults s that we place into a N_s -dimensional solution vector \mathbf{m} at time step k . At each time step we select constraints to apply to the motion of the fault on any point depending on the previous rupture history.

The general form of a linear minimization problem is stated as follows. Let \mathbf{x} be the solution vector composed by N independent variables; we find the \mathbf{x} that minimizes the *objective function* $\psi = \mathbf{c}^T \mathbf{x}$ subject to the primary constraints

$$x_i \geq 0, \quad i = 1, \dots, N \quad (2.2)$$

and to equality constraints

$$\mathbf{B}\mathbf{x} = \mathbf{d}, \quad (2.3)$$

where \mathbf{d} is the N_d -dimensional *data* vector, and \mathbf{B} is the $(N_d \times N)$ matrix that maps the model space (\mathbf{x}) into the data vector \mathbf{d} . Inequality constraints can be easily included by means of slack variables (Luenberger, 1984). In the following we discuss our choice of the constraints and their implementation in a linear minimization problem.

2.3.1 Constraints

The application of constraints allows us to obtain a set of dynamic models consistent with required properties. For example, in Chapter 3 our goal will be to show that a broad range of dynamic models satisfies important kinematic parameters such as rupture velocity, moment rate function and final slip. We accomplished this task by generating two source models satisfying the same *kinematic* constraints and subject to different *dynamic* properties.

It is important to note that at every time step k the load vector L_{aijk} is completely determined by quantities calculated at previous time steps; this means that the information about the past rupture process constrains the solution at the current time step.

We separate the constraints into *observation*, *kinematic*, *smoothing*, and *dynamic* constraints.

2.3.1.1 Kinematic Constraints

K1. Total slip increment at time step k equals a given moment-rate function. At time step k a moment rate function M_k can be applied as a constraint to the model. We require

$$\text{that } M_k = \sum_{s=1}^{N_s} \Delta u_{sk}.$$

K2. Rupture velocity. We can impose a rupture time distribution by prohibiting slip on each subfault until a desired time.

K3. Fit a given dislocation model. At each time step k and for each subfault s we can require that the incremental slip Δu_{sk} equals that one of a given dislocation model.

2.3.1.2 Smoothing Constraints

S1. Minimize the first difference between cumulative slip on adjacent subfaults. At each time step k we smooth the cumulative slip on adjacent subfaults along the strike and dip of the fault. $u_{s(k-1)}$ and $u_{(s+1)(k-1)}$ are the cumulative slip at the previous time step at two adjacent subfaults, and Δu_{sk} and $\Delta u_{(s+1)k}$ are the respective incremental slip

(unknown) at the current time step. Let $r_{s(s+1)k}$ be the first difference between cumulative slip on adjacent subfaults:

$$r_{s(s+1)k} = (u_{s(k-1)} + \Delta u_{sk}) - (u_{(s+1)(k-1)} + \Delta u_{(s+1)k}). \quad (2.4)$$

The objective function ψ is the L_1 norm of the vector of *residuals* \mathbf{r} formed by the $r_{s(s+1)k}$ for all the pairs of adjacent subfaults that enter the solution vector \mathbf{m} at time step t_k . To express the L_1 minimization problem in the standard form of the linear programming, we represent the residual vector \mathbf{r} as the difference of two vectors with nonnegative components (Das and Kostrov, 1990), $\mathbf{r} = \mathbf{r}^+ - \mathbf{r}^-$. Appending the vector \mathbf{r} to the vector of unknowns \mathbf{m} we form the solution vector $\mathbf{x} = (\mathbf{m} \ \mathbf{r}^+ \ \mathbf{r}^-)^T$. This constraint together with the requirement KI specify the basic formulation of our linear minimization problem. For each time step k , let $h_q = u_{s(k-1)} - u_{(s+1)(k-1)}$, $q = 1, \dots, N_q$ where N_q is the number of pairs of adjacent subfaults that enter the solution vector \mathbf{m} . Then, in equation 2.3 $\mathbf{d} = (M_k \ \mathbf{h})^T$ is the $N_d = N_q + 1$ - dimensional data vector, \mathbf{x} is the $N = N_s + 2 \times N_q$ - dimensional solution vector, and

$$\mathbf{B} = \begin{pmatrix} \mathbf{1}_{1 \times N_s} & \mathbf{0}_{1 \times N_q} & \mathbf{0}_{1 \times N_q} \\ \mathbf{D}_{N_q \times N_s} & \mathbf{I}_{N_q \times N_q} & -\mathbf{I}_{N_q \times N_q} \end{pmatrix}, \quad (2.5)$$

where \mathbf{D} is the first difference matrix, \mathbf{I} is the identity matrix, and $\mathbf{0}_{n \times m}$ and $\mathbf{1}_{n \times m}$ are the $n \times m$ matrices of zeros and ones.

From the following *dynamic* constraints we can calculate lower and upper bounds on the solution vector \mathbf{m} .

2.3.1.3 Dynamic Constraints

D1. The stress drop is bounded. At any time step k , stress drop can be calculated from the stress change calculated using equation 2.1. We can impose an upper bound on the stress drop in each subfault, which is the static stress drop of a given *reference* model, so that the stress drop distribution of the solution model has similar characteristics. Moreover, we can use this upper bound of stress drop to implement the constraint *D3*.

D2. Slip velocity is bounded. We assume isotropic friction (i.e. slip velocity is always collinear with total traction). This is a fundamental physical constraint that applies at all points and all time steps and determines the slip direction at each time step based on previous conditions. From this requirement Spudich (1992, equation 4-7 and 8b) derived an *upper bound* on the slip velocity.

D3. The rate of slip-weakening is bounded. We can impose bounds on the slope of the slip-weakening curve (Chapter 3, Figure 3.1) for different solution models. In particular, we can force one model to have a steep slip-weakening curve (fast weakening) and a second model to follow a slow weakening with a longer slip-weakening distance.

For simplicity here we show how the bounds on the rate of weakening are imposed for a pure strike-slip case. The more general case in which the rake of slip is not fixed a priori is easily approached using the collinearity requirement between slip velocity and friction (constraint *D2*). At a given subfault s let $\Delta\sigma_{max}$ be the upper bound on stress drop from constraint *D1*, σ^y be the yield stress found as the value of stress at this subfault at the onset of slip, and D_{cmin} and D_{cmax} be the minimum and maximum slip-weakening distances, respectively, that we wish the resulting slip-weakening curve governing the dynamics of the model to have. From these parameters we can calculate the maximum rate α_1 and the minimum rate α_2 of weakening that we impose to our solution at each time step:

$$-\alpha_1 = \frac{C(\sigma^y - \sigma^o + \Delta\sigma_{max})}{D_{cmin}}, -\alpha_2 = \frac{C(\sigma^y - \sigma^o + \Delta\sigma_{max})}{D_{cmax}}, \quad (2.6)$$

where $C = G_o\Delta t$.

From these we can derive an upper and lower bound to the incremental slip Δu_k that is the solution of our linear programming problem at time step t_k at the given subfault. In fact, once the subfault starts slipping, we want that

$$-\alpha_2 \leq \frac{T_k - T_{k-1}}{\Delta u_k} \leq -\alpha_1, \text{ where } T_k = C\tau_k, \quad (2.7)$$

and from equation 2.1 substituting $T_k = L_k - u_k$, and $u_k = u_{k-1} + \Delta u_k$ we obtain

$$\frac{T_{k-1} + u_{k-1} - L_k}{1 - \alpha_2} \leq \Delta u_k \leq \frac{T_{k-1} + u_{k-1} - L_k}{1 - \alpha_1}, \quad (2.8)$$

where we have omitted the s subscript for simplicity.

2.3.1.4 Observation Constraints

O1. Fitting ground motion data can be accomplished by expanding the data vector \mathbf{d} in equation 2.3 to include a N_g – dimensional ground motion data vector, \mathbf{g} : $\mathbf{d} = (M_k \quad \mathbf{h} \mathbf{g})^T$. Let the predicted ground motion be $\mathbf{A}\mathbf{m}$, where \mathbf{A} is a matrix whose columns are Green's function time series relating slip at a point ij to ground motions at each observer (subfault synthetics). Correspondingly, $\mathbf{r}_g = \mathbf{d} - \mathbf{A}\mathbf{m}$ is the observation residual vector that can be represented as $\mathbf{r}_g = \mathbf{r}_g^+ - \mathbf{r}_g^-$ and is appended to the solution vector \mathbf{x} . Then, the matrix \mathbf{B} becomes:

$$\mathbf{B} = \begin{pmatrix} \mathbf{1}_{1 \times N_s} & \mathbf{0}_{1 \times N_q} & \mathbf{0}_{1 \times N_g} \\ \mathbf{D}_{N_q \times N_s} & \mathbf{I}_{N_q \times N_q} & -\mathbf{I}_{N_q \times N_g} \\ \mathbf{A}_{N_g \times N_s} & \mathbf{I}_{N_g \times N_s} & -\mathbf{I}_{N_g \times N_g} \end{pmatrix}. \quad (2.9)$$

Chapter 3 - What Can Strong Motion Data Tell Us About Slip-Weakening Fault Friction Laws?

Published in *Bull. Seism. Soc. Am.* (2000), **90**, 98-116. © Seismological Society of America

- 3.1 Introduction
- 3.2 An Ideal Test Case
- 3.3 Results
- 3.4 Discussion
- 3.4 Conclusions

Abstract

In this chapter I consider the resolution of fault constitutive parameters, such as strength excess, $\sigma^y - \sigma^o$, and slip-weakening distance, D_c , that may be obtained from the analysis of strong ground motions. I show that waveform inversion of a synthetic strong motion data set from a hypothetical M 6.5 event resembling the 1979 Imperial Valley earthquake cannot uniquely resolve both strength excess and D_c . Specifically, I use the inversion method described in Chapter 2 to find two rupture models, Model A having $D_c = 0.3$ m and high strength excess, and Model B having $D_c = 1$ m and low strength excess. Both models have the same moment-rate function and rupture time distribution, and they produce essentially indistinguishable ground motion waveforms in the 0-1.6 Hz frequency band.

These models are indistinguishable because there is a trade-off between strength excess and slip-weakening distance in controlling rupture velocity. However, fracture energy might be relatively stably estimated from waveform inversions. Models A and B had very similar fracture energies. If the stress drop is fixed by the slip distribution, the rupture velocity is controlled by fracture energy.

Estimates of slip-weakening distance inferred from kinematic inversion models of earthquakes are likely to be biased high due to the effects of spatial and temporal smoothing constraints applied in such inverse problem formulations.

Regions of high strength excess are often used to slow or stop rupture in models of observed earthquakes, but our results indicate that regions of long D_c and lower strength excess might alternately explain the slowing of rupture. One way to constrain D_c would be to model ground motion spectra at frequencies higher than those at which waveform modeling is possible. A second way to discriminate between regions of long D_c and large strength excess might be to assume that D_c is long where there are no aftershocks.

3.1 Introduction

Two major goals of seismology are the discovery of the stress conditions on faults before and during earthquakes, and the inference of a constitutive law that characterizes the material response to the applied stress. A constitutive relation represents the governing equation of the failure process, and specifies the dependence between stress, fault slip, slip rate and other relevant physical properties. While theoretical, numerical, and laboratory simulations of earthquakes have led to tremendous insights into possible constitutive laws, the ultimate test of a constitutive law is its ability to model the behavior of real earthquakes occurring on real faults in the Earth.

The constitutive relation is a key element of dynamic descriptions of the seismic source which are based on models that satisfy the elastodynamics equation (e.g. Andrews, 1976a; 1976b, 1985; Mikumo and Miyatake, 1978; Day, 1982; Das and Kostrov, 1987; Harris *et al.*, 1991). In the framework of fracture mechanics, an earthquake may be considered as a dynamically propagating shear crack that radiates seismic waves. The resulting motion (slip history) on the fault is related to a drop in shear stress. The slip history evolution depends on the failure criterion, the constitutive properties and the initial conditions on the fault surface. In contrast, kinematic models of the seismic source (for example Haskell, 1964) prescribe the displacement history of motion *a priori*, without an explicit attempt to investigate the physical causes of the rupture process.

In some previous works of dynamic simulation, the constitutive relation is assumed to be a simple slip-weakening model (Ida, 1972; Andrews, 1976a; 1976b; Day, 1982) which is completely characterized by initial stress σ^o , yield stress σ^y , dynamic frictional stress σ^f , and *slip-weakening distance* D_c (Figure 3.1). In this model the fault begins to rupture when the yield stress, σ^y , is exceeded. As the slip grows to the critical slip-weakening distance, D_c , the strength of the fault decreases to the dynamic frictional stress, σ^f . The strength excess, $\sigma^y - \sigma^o$, is the difference between the yield stress and the initial stress (Boatwright and Quin, 1986). The stress drop is $\sigma^o - \sigma^f$.

More complicated fault-constitutive laws are required to explain some aspects of earthquake behavior, viz. the re-strengthening of faults between earthquakes. However,

results of laboratory experiments on rock-on-rock frictional sliding at high-speed slip (Okubo and Dieterich, 1986) and of numerical modeling of dynamic rupture with laboratory-derived constitutive laws (Okubo, 1989) suggest that slip-weakening is the prevailing constitutive behavior during dynamic rupture. Therefore, in this study we adopt slip-weakening as a relatively simple model for which we can try to recover the defining parameters from observations of earthquakes.

The primary purpose of this study is to answer the following questions: Can the slip weakening distance and strength excess be uniquely determined by modeling ground motion data? Can the slip-weakening distance and the strength excess be inferred uniquely from a kinematic source model? How wide a range of these parameters is consistent with a given ground motion data set?

The answers to these questions have implications for published values of strength excess and slip weakening distance. Strength excess $\sigma^y - \sigma^o$ has been derived for many moderate earthquakes by Quin (1990), Fukuyama and Mikumo (1993), Ide and Takeo (1996), Beroza and Mikumo (1996), Bouchon (1997), Day *et al.* (1998), and others. Of particular interest are two papers that also estimated slip-weakening distance D_c . The first is Ide and Takeo (1997), who derived a constitutive relation from inversion of strong ground motion data from the 1995 Hyogo-ken Nanbu (Kobe), Japan, earthquake. They inferred a $D_c \approx 1m$ for the shallow part of the fault, and they estimated an upper bound of 0.5 m for D_c on the deeper part of the fault. The second paper is Olsen *et al.* (1997), who estimated $D_c = 0.8$ m for the 1992 Landers, California, earthquake by dynamically simulating previously obtained kinematic models of the Landers event. These estimates of D_c are quite high compared to values measured in the laboratory, typically of the order of $10\mu m$ (e.g. Dieterich, 1978). While there are reasons to expect that d_c on real faults might be much larger than in the laboratory (Scholz, 1988; Okubo and Dieterich, 1984; 1986), it is also important to assess the reliability of the estimates of d_c derived from strong motion data.

In this study we present an inversion method for deriving dynamic rupture models that satisfy both a given kinematic source model and constraints on desired properties of fault constitutive parameters. This inversion method can be generalized to invert seismograms. We use this procedure to demonstrate that there is a strong trade-off between the strength excess and the slip-weakening distance in controlling rupture velocity. We find that many different combinations of these two parameters cause the same rupture time distribution, and consequently radiate similar ground motions. We show that waveform inversion of a synthetic strong motion data set from a hypothetical M 6.5 event in the frequency band 0 - 1.6 Hz cannot uniquely define stress parameters and slip weakening distance D_c . Specifically, we use our inversion method to produce two rupture models having a $D_c=0.3$ m and $D_c=1.0$ m, and we find that these two rupture models produce indistinguishable ground motion waveforms in the 0 - 1.6 Hz band. Moreover, these rupture models have identical rupture times and very similar slip distributions and rise times (the time required to accumulate 10% to 90% of the total slip at individual points). Given these difficulties, it may be necessary to resort to broad-band spectral domain studies in order to define constitutive relations for moderate-sized earthquakes.

We will demonstrate our results using theoretical seismograms from a hypothetical test earthquake designed to resemble the M 6.5 1979 Imperial Valley, California, earthquake. Our initial goal had been to apply the new inversion method to the observed ground motion data from the Imperial Valley earthquake in order to determine the constitutive law. In the process of preparing synthetic test rupture models in order to test the inversion method, we discovered the nonuniquenesses that we present in this study.

3.2 An Ideal Test Case

Our approach is to show that, in general, the relevant kinematic properties of a source, such as rupture velocity, final slip and moment rate function are consistent with a

broad range of slip-weakening constitutive laws. In general, slow rupture velocity is caused by either a long slip-weakening distance or a high strength excess, and the opposite is true for a fast rupture propagation. A simple way to state this type of ambiguity is that a high strength - short slip-weakening distance model is “equivalent” to a low strength - long slip-weakening distance model. We have generated two dynamic models that represent these two extremes and conform equally to the important kinematic parameters. The first step to accomplish this task was the design, by means of a spontaneous rupture calculation, of a *reference* model whose dynamic properties lie between those two extreme characterizations. The resulting rupture velocity, moment rate function and final slip represent the reference kinematic properties which the two equivalent dynamic models must both satisfy.

Ideally, an earthquake that has relatively long rise times (the duration of slip at individual points) and ground motion data that can be modeled accurately at high frequencies would present the best opportunity to resolve details of the rupture process. In order to decide which earthquake we should try to simulate, we surveyed published waveform inversion studies. We visually examined the waveform fits of Hartzell and Heaton (1983), Archuleta (1984), Hartzell (1989), Beroza (1991), Steidl *et al.* (1991), Wald *et al.* (1991), Fukuyama and Mikumo (1993), Cohee and Beroza (1994), Wald *et al.* (1994), Cotton and Campillo (1995), Wald (1996), Ide *et al.* (1996), and Ide and Takeo (1997), and we determined that for all of these, with the possible exceptions of Ide *et al.* (1996) and Ide and Takeo (1997), the shortest modeled period was equal or longer than the main asperity rise time in the published kinematic model, meaning that these studies cannot be used to infer fault constitutive relations. In the latter two papers on the Kobe earthquake, almost all the modeled data were long period, but two short period stations were modeled to periods of about 2 s. Cotton and Campillo (1995) showed spectra of their waveform misfits, a laudable practice which should be encouraged in future inversions.

We chose to simulate an earthquake that resembles the 1979 Imperial Valley earthquake because that event offers possibly the best data set for determination of constitutive relations. In fact, Hartzell and Heaton (1983) obtained a good waveform fit

at 1.5 s period at several stations, and they and Archuleta (1984) found a rise time of 1.7 and 1.8 s, respectively, on the main asperity. Given the excellent station geometry (Figure 3.2) and the approximately laterally homogeneous local velocity structure (Fuis *et al.*, 1984), there is hope that its waveforms could be modeled to periods of 1 s or shorter at many stations.

Figure 3.2 shows the map view of the Imperial Valley area with the station distribution, the fault trace and the epicenter *location*. The Imperial Valley earthquake had substantial surface slip (Sharp *et al.*, 1982) and a well-determined epicenter (Archuleta, 1982), thus giving a fault length of about 35 km northwest of the epicenter (Archuleta, 1984). The inversion results of Olson and Apsel (1982) indicate that slip occurred also on a 10-km segment south of the epicenter.

For the parameterization of our models, we assume a fault plane that extends about 33 km north of the epicenter and 8 km south of the epicenter along a strike of 323°, and reaches a depth of 14 km with a 80° NE dip. We used the hypocenter of Archuleta (1982) at depth of 8 km. We gridded the fault plane into 988 subfaults (52 along strike and 19 along dip) each about 0.8 km square.

The first step in our investigation was the creation of a reference dynamic rupture model. Specifically, on our simulated Imperial Fault we had to find distributions of strength excess, stress drop, and slip weakening distance which would lead to a rupture that had approximately the same slip and rupture time distributions as those determined by Archuleta (1984) for the 1979 Imperial Valley earthquake. This task was accomplished by trial-and-error forward modeling using the boundary integral spontaneous rupture computer code developed by Boatwright and Quin (1986), Quin and Das (1989), Quin (1990), and modified by Spudich *et al.* (1998) to include free-surface reflections and vertical variations of the velocity structure. We applied the method of Spudich *et al.* (1998) to derive the stress drop $\sigma^o - \sigma^f$ distribution from the slip distribution of Archuleta's model (1984), and by trial and error we found that a spatially uniform strength excess of about 4 MPa and a uniform slip-weakening distance of about 0.5 m yielded slip and rupture time distributions similar to Archuleta's kinematic model. Our reference model lacked the super-shear rupture velocity observed by Archuleta, but this discrepancy was irrelevant to our subsequent use of the reference model.

Then we used the inversion method described in Chapter 2 to generate two rupture models - one characterized by a short slip-weakening distance (~ 0.3 m) and high strength excess (Model A), and the other by a long slip-weakening distance (~ 1 m) and low strength excess (Model B), both of which are consistent with the moment rate function, rupture time and slip distributions of the reference model. Although these values of slip-weakening distance are large compared to the values implied by results of rock friction experiments, the scaling of this constitutive parameter for real faults during dynamic rupture is still not known, and recent proposed estimates based on waveform inversion are of the order of 0.5 m (Ide and Takeo, 1997; Olsen *et al.*, 1997). In general, we can only hope to resolve these very large slip-weakening distances from waveform inversion. If we cannot distinguish a slip-weakening distance of the order of 0.3m from one of about 1m, clearly shorter slip-weakening distances cannot be distinguished.

3.3 Results

In this section we analyze the characteristics of the two dynamic models A and B obtained with the inversion described in Chapter 2. These models are kinematically equivalent because both have the same moment rate function and slip distribution and rupture time, but they differ in the two critical parameters of the fault constitutive relation, the strength excess distribution and the slip-weakening distance. We shall show later that their ground motion waveforms are very similar.

Figure 3.3a shows the rupture time distribution common to both models imposed through constraint K2 (Chapter 2), and the similarity of the moment rate functions is evident in Figure 3.3b. Figure 4 shows all the relevant dynamic and kinematic parameters for the two models. The final slip distribution (Fig 3.4a and 3.4b) is remarkably similar; model B shows larger slip maxima than model A, but these differences would probably be too small to be resolved by either geodetic observations or low frequency waveform data, given that both models basically satisfy the same moment rate function (Figure 3.3b). The static stress drop distributions (Fig 3.4c and 3.4d) are bounded by the static stress drop distribution of the reference model (constraint D1,

Chapter 2). They have small differences caused by the different scaling used in the two cases.

3.3.1 Trade-off between Strength Excess and Slip-weakening Distance

The strength excess (Figure 3.4e and 3.4f) and the slip-weakening distance distributions (Figure 3.4g and 3.4h) differ substantially and their analysis is important to understand the origin of non-uniqueness in the problem of fitting kinematic properties with spontaneous rupture modeling. Model A has a slip-weakening distance of the order of 0.3 m (as required by constraint D3, Chapter 2), and for model B this constraint results in a slip-weakening distance of the order of 1m; on the other hand the strength excess in model A is substantially larger than that in model B. It is important to note that the strength excess is not directly constrained by any imposed requirement; at each point it is simply the stress at the instant that point is allowed to rupture (Miyatake, 1992). In Figure 3.5 we depict the slip-weakening curves for selected subfaults over different depths and distances along the strike of the faults. From this figure it is possible to appreciate the differences in the rate of weakening as imposed by constraint D3.

Let us consider the strength parameter S and its role in controlling the rupture velocity. Andrews (1976b; 1985) showed that for $S > 1.77$ the limiting rupture velocity in plane strain is the Rayleigh velocity. If $S < 1.77$, however, when the crack has propagated a sufficient distance, the rupture velocity can become larger than the S-wave velocity (Andrews, 1976b, Das and Aki, 1977, Day, 1982). In a slip-weakening model the transition in rupture velocity depends on the half-length of a critical crack L_c (equation 10 in Day, 1982 and equation 43 in Andrews, 1985), and therefore on D_c . This means that in these studies the effect of D_c on the rupture velocity was implicitly taken into account through the length scale L_c . Our simulations show that, in a spontaneous rupture calculation of a finite source, a sub-shear rupture velocity can be equally attained by combining a relatively low S parameter and a large slip-weakening distance, or a high S with a short slip-weakening distance. If the stress drop is fixed, then the relevant parameters that trade-off are the strength excess and the slip-weakening distance

3.3.2 Apparent fracture energy

Figures 3.4i and 3.4l show the distribution of the apparent fracture energy G_c for the two models. The shear fracture energy is defined as the amount of energy needed to create a unit area of fault by shear fracture, and in a simple slip-weakening model is calculated as

$$G_c = \frac{1}{2}(\sigma^y - \sigma^f)D_c \quad (3.1)$$

(Andrews, 1976a).

Estimates of shear fracture energy have been calculated for many earthquakes (e.g. Ida, 1973; Hussein *et al.*, 1975; Aki, 1979; Beroza and Spudich, 1988), yielding a range from 10^2 to 10^8 J/m². Our models yield an apparent fracture energy of the order of 10^6 J/m², and this value may provide a rough estimate of this parameter for a moderate size event such as the 1979, Imperial Valley earthquake. The distributions of G_c for the two models are remarkably similar and resemble the respective stress drop distributions, suggesting that the apparent fracture energy might be stably estimated from waveform inversions.

3.3.3 Radiated Waveforms and Spectra

We compare the seismograms and the spectra calculated from model A and model B up to ~ 2 Hz at 14 observer locations well distributed around the rupture area of the 1979 Imperial Valley earthquake (Figure 3.2). These seismograms were calculated using the methods of Olson *et al.* (1984) and Spudich and Archuleta (1987) assuming the velocity structure of Archuleta (1984). We calculated the seismograms in the frequency band 0 - 1.8 Hz and we lowpass filtered them with a cosine taper between 1 and 1.8 Hz.

Figure 3.6 shows the seismograms calculated from model A and model B. In general they are nearly identical, especially for the low frequency part of the signals. This similarity shows that it will be very difficult to resolve constitutive parameters from waveform inversion in this frequency band. A detailed analysis of the waveforms reveals some differences. In general, the seismograms from model A are richer in high

frequency than those from model B. This enhanced short period content is particularly evident for stations close to the fault (e.g. EMO) that are in the forward directivity region (BRA and PTS), and at stations like AGR and MEX which fall in the backward directivity zone where the details of the rupture process (close to the hypocenter) are better resolved.

For waveform inversions, these distinctions would not be sufficient to discriminate the details of the rupture process, mainly due to the inherent difficulty of modeling high frequency signals given our usually inadequate Green's functions. The differences between the model A and model B seismograms are substantially smaller than the misfit usually accepted in modeling real waveform data. However, this analysis suggests that the frequency content of acceleration data might help bound the parameters of interest of fault constitutive behavior.

In Figure 3.7 we show the displacement amplitude spectra for the three components of ground motion at some stations in different positions around the fault. The differences in frequency content and relative amplitude already discussed in the seismogram analysis are especially evident in the spectra. Above ~ 1 Hz the amplitude spectra from Model A are larger than those from Model B, especially at stations close to the fault (e.g. EMO and AGR), in the forward directivity region (BRA) and in the backward directivity region (AGR and MEX). However, neither the spectra nor the waveforms for stations distant from the fault (e.g. E05 and E11) show systematic differences.

Figure 3.8 summarizes the spectral content of the three components of motion for all 14 stations used in this study. For each component we show the ratio of the smoothed amplitude spectra of model A and that of model B; the thick line represents the mean of these ratios, and the dashed lines correspond to the mean \pm the standard deviation. For the vertical component the differences in the spectral amplitudes between the two models are negligible, as shown by the ratio of amplitude spectra having a mean value of about 1. On the other hand, for the two horizontal components there is a systematic increase in the ratio of amplitude spectra above 1 Hz, reaching a mean value of about 2.5 at 1.6 Hz. This analysis demonstrates that the two dynamic models are equivalent from the point of view

of fitting the low frequency content of the observational constraints, while the specific characteristics that distinguish them affect only the short period part of the data.

In the following section we analyze the resulting discrepancies in the source time functions in order to explain, in term of the physics, the differences noted in the waveforms and in the spectra.

3.3.4 Source Time Function (STF) and Rise Time

The analysis of the resulting source time functions highlights that the two source dynamic descriptions, while consistent with the kinematic constraints K1 (moment rate) and K2 (rupture time), differ in other, more detailed, kinematic parameters that mostly affect the short period content of ground motions data. The features that characterize and distinguish the source time functions of the two models (Figure 3.9) can be generalized as follows: for Model A the source time function follows a typical Kostrov-like functional form with large peak slip velocity (and fast decay); for Model B the source time function shows a typical triangular shape (or an overlapping of different triangular functions) with lower peak slip velocity than for model A. The large peak slip-velocity in model A is related to a large peak stress (strength excess) as shown by Andrews (1976a) and Ohnaka and Yamashita (1989). At every subfault the total slip implied by each model is about the same, meaning that the zero frequency part of the data is not affected by these differences.

The STF for model B can be interpreted as a low-passed version of the STF for model A, therefore, the ground motions data calculated from the two models is equivalent for the low frequency part of the signal (in this case up to ~ 1 Hz). At higher frequencies, the differences in the details of the rupture process will affect the seismograms.

The differences in the shapes of the STF resulting from the two models suggest that there might be a specific time parameter that distinguishes the two cases. The rise times (here defined as the time required to accumulate from 10% to 90% of the total slip) for both models are very similar (Figure 3.10). The similarities between the two distributions imply that the analysis of this parameter (as it is defined here) would not help resolve the dynamic non-uniqueness discussed in this study, at least for differences in the value of slip-weakening distances such as those considered in this study.

3.3.5 Local Breakdown Time and Slip-Weakening Distance Resolution

An important time parameter that characterizes and distinguishes the two dynamic models is the local breakdown time T_c , defined as the time over which the weakening occurs (Ohnaka and Yamashita, 1989) (Figure 3.11). In a slip-weakening model, this is the shortest period that characterizes the rupture process. Because the generation of high frequency radiation is directly related to details of the rupture process, the larger generation of short period radiation of Model A compared to Model B is caused by the rate of weakening (and therefore the breakdown time). From Figure 3.11 we observe that T_c for Model A is much shorter than that of Model B over the fault plane, this short breakdown time being caused by both a short slip-weakening distance and a high strength excess (Figure 3.5 and Figure 3.11). The differences in the rate of weakening between Model A and Model B are evident in the rate of decay of their respective slip-velocity histories.

The local breakdown time is the period that we must resolve if we aim to learn something about the weakening process. The shortest modeled period in the ground motion data is the shortest resolvable period in the rupture process, $T_{c\min}$. From $T_{c\min}$ it is possible to estimate the shortest resolvable slip-weakening distance $D_{c\min}$ from a given data set. At a given point on the fault, let T_c be the true breakdown time, and \bar{s} be the average slip velocity over T_c ; then the true slip-weakening distance D_c is $D_c = \bar{s}T_c$. If we can roughly estimate \bar{s} from ground motions data, then

$$D_{c\min} = \bar{s}T_{c\min}. \quad (3.2)$$

This relation is plotted in Figure 3.12 for different values of \bar{s} .

Based on the above results, it appears that the estimate of the slip-weakening distance from a kinematic source model might be influenced by the specific source time function chosen to parameterize the time dependence of the slip.

3.4 Discussion

3.4.1 Interpretation of Previous Estimates of Slip-weakening Distance and Strength Excess

Stress drop and rupture velocity are relatively well determined by fitting narrow band waveforms. On the other hand, the slip-weakening distance is not uniquely determined because in a dynamic slip-weakening model, resistance to rupture is obtained either from large strength excess or large slip-weakening distance.

Regions of high strength excess are often used to slow or stop rupture in modeling observed earthquakes. For example, the numerical methods of Fukuyama and Mikumo (1993), Mikumo and Miyatake (1993), Beroza and Mikumo (1996) and Ide and Takeo (1996) all use a critical stress fracture criterion, in which there is no slip weakening distance, so only a high strength excess can be used to stop rupture in these models. The levels of strength excess appearing in their models are upper limits on the values consistent with the data. Because the fracture energy in these critical stress fracture criterion models is ambiguous, we cannot estimate plausible combinations of strength excess and nonzero slip weakening distances for their models.

Our results suggest that slip weakening distances inferred from kinematic inversion models of earthquakes are biased high because such inversions are typically constrained to have a fairly smooth slip rate functions. Clearly, a slip rate function that initiates with a Kostrov-like $t^{-1/2}$ singularity will have a slip weakening distance of zero. Any slip rate function initiating more gradually will have a longer slip weakening distance. Slip rate functions consisting of overlapping triangular (e.g. Wald, 1996; Ide *et al.*, 1996) or box-car functions (Yoshida *et al.* 1996) necessitate a slow weakening behavior resulting in relatively long slip-weakening distance compared to the final slip. In addition, the spatial and temporal smoothing constraints applied in such inverse problem formulations average the slip-velocity, lowering possible high initial peak slip velocities typical of fast weakening. These effects combine and bias the estimate of the slip-weakening distance to one extreme (i.e. to large values) of the range of possible solutions consistent with the data. Moreover, from relation (2) and Figure 3.12 it appears

that the limited temporal resolution imposed by the shortest modelled period in the ground motion introduces another type of systematic error in D_c distributions inferred from inversions of narrow-band strong motion data. This systematic error causes D_c to be correlated with the average slip-velocity and possibly with the total slip in each subfault.

The use of triangular slip velocity functions and of temporal smoothing probably explains the inability of Ide and Takeo (1997) to resolve slip weakening distances less than 0.5 m. However, as they emphasize, the inferred differences in the rate of weakening between shallow and deep subfaults might be more informative of different slip-weakening behaviors than the estimated values of D_c which could be biased as indicated above. However, using the length of straight initial parts of striations observed on the Nojima Fault, Spudich (1999) provides estimates of the upper bound on the shallow slip weakening distance of 0.1 - 0.5 m, based on the numerical results of Guatteri and Spudich (1998).

The 0.8 m slip weakening distance obtained by Olsen *et al.* (1997) for the 1992 Landers earthquake is not well constrained (as they themselves noted) because these authors did not explore the range of strength excess and slip weakening distance consistent with Wald and Heaton's (1994) kinematic model. Olsen *et al.* (1997) found a dynamic model which duplicated Cotton and Campillo's (1995) rise times, but our Models A and B have the same rise time and show that the rise time parameter is not adequate to discriminate between long and short slip weakening distance models in the range of variation considered in our and their study.

Consequently, with the possible exception of Ide and Takeo's (1997) 1 m slip weakening distance (slow rate of weakening) for the shallow Nojima Fault, none of the presently available determinations of slip weakening distance or strength excess based on waveform inversion is unique.

3.4.2 Implications for Resolution of Source Time Function Parameters

The lack of resolution of constitutive parameters such as strength excess and slip-weakening distance from narrow-band waveform inversions implies that the inferred parameters of the source time function, such as peak slip-velocity, duration and time function, are also poorly constrained.

The peak slip velocity is an important strong motion parameter in broadband simulations of ground motion for engineering applications. Yet, from the comparison of the STFs of model A and model B (Figure 3.9), it is evident that constraining the slip-rate to be temporally smooth would likely cause its peak value to be underestimated from narrow-band ground motion data.

The STFs of model A and model B are both consistent with a slip-weakening behavior, and therefore the slip duration at a point on the fault in both models is controlled by the rupture dimension. In the two models, the total slip at each subfault is about the same, but in model A large slip-velocities occur over a much shorter period of time (controlled by T_c) than in model B. This difference affects the resulting ground motions only at high frequency, implying that the rates of growth and decay of slip-velocity are not uniquely constrained from narrow-band ground motion data (Spudich and Archuleta, 1987). Nonetheless, the shape of the STF may greatly affect the ground motion at high frequency.

We can speculate that a slip-weakening model consistent with the kinematic constraints applied to model A and B, and having a D_c of the order of mm would result in a STF with a relatively high peak slip velocity and fast decay, and with a long tail at very low slip-velocity compared to those of model A and B. The total duration of slip would still be controlled by the rupture dimension, but very low slip-velocity tail might be seismically invisible, causing this particular STF to be "seen" as a narrower slip function. Therefore, a simple slip-weakening model characterized by a very short slip-weakening distance might be consistent with observed slip pulses and the associated important directivity effects and their significant hazard.

For the 1984 Morgan Hill earthquake, for which there is strong evidence of a short rise time (Beroza and Spudich, 1988), Beroza and Mikumo (1996) have shown that a dynamic model governed by a critical fracture criterion can explain the observed waveforms. The slip-rate function associated with a critical fracture criterion can be

considered as an approximation of the slip-rate function resulting from a slip-weakening model with an extremely short D_c . Therefore, assuming that slip-weakening is the prevailing constitutive behavior during dynamic rupture, a short rise time and pulse-like slip function needed to fit the observed ground motion (Heaton, 1990) might suggest that D_c is very short, at least of the order of mm .

3.4.3 How Can We Reduce the Dynamic Non-Uniqueness?

One way to learn more about slip weakening distance would be to attempt to simulate the ground motion spectra in the frequency band above that in which waveform modeling is possible. Figure 3.8 shows that ground motion spectra are systematically elevated at high frequencies when slip-weakening distance is short. It might be possible to combine waveform and spectral criteria into the misfit function of future inversions.

Ohnaka and Yamashita (1989) found theoretical and experimental relations among strong motion parameters and frictional properties of the fault. By analyzing the high frequency radiation, these relations might help narrow the space of dynamic solutions consistent with low-frequency data. We write their equation (50) that specifies the relation between the local breakdown time T_c and the yield strength σ^y , the rupture velocity v and the slip-weakening distance D_c :

$$T_c \propto \frac{C(v)}{v} \frac{\mu}{\sigma^y} D_c \quad (3.3)$$

where $C(v)$ is a function of rupture velocity, and μ is the shear modulus. From this relation they found that T_c becomes shorter as both v and σ^y get higher and as D_c becomes shorter. From equation 3.3 the ratio

$$\frac{D_c}{T_c \sigma^y} \propto \frac{v}{\mu C(v)} \quad (3.4)$$

is expected to be equal for models A and B because the rupture velocity and the elastic properties of the medium are identical. We investigate the validity of this relation for our models by calculating the corresponding ratio in equation 3.4 at each subfault using,

instead of the yield strength, the respective values of strength excess, which is more relevant to seismic rupture propagation because the process is primarily controlled by stress differences. We estimate T_c from the slip and stress histories of the two models (Figure 3.9). In Figure 3.13 we plot the value of equation 3.4 calculated at each subfault for model A along the x axis and that for model B along the y axis. From this plot we can conclude that the relation in equation 3.4 holds for the two models analyzed in this study and from this result we can envision a feasible way to reduce the ambiguity in inferring a dynamic description of the source consistent with observations.

Ohnaka and Yamashita (1989), on the basis of empirical and theoretical results, determined $f_{\max}^S = 1/T_c$ as the cutoff frequency of the power spectral density of slip acceleration, and they argue that $f_{\max} \leq f_{\max}^S$, where f_{\max} is the upper limit of frequency of spectral band of strong motion accelerograms recorded in the near source region from an earthquake source (e.g. Brune, 1970; Ida, 1973; Hanks, 1982, Papageorgiou and Aki, 1983). Therefore, from relation 3.4 we can find a lower bound on the ratio between the strength excess and slip-weakening distance

$$\frac{(\sigma^y - \sigma^o)}{D_c} \geq f_{\max} \mathfrak{S}(v, \mu) \quad (3.5)$$

where $\mathfrak{S}(v, \mu)$ is a function of rupture velocity and the shear modulus. Once estimates of rupture velocity and slip distribution for a given earthquake source are found by waveforms analysis, we can speculate that the non-uniqueness of the corresponding source dynamic description can be reduced by imposing the lower bound from equation 3.5 on the ratio of strength excess and slip-weakening distance that characterize the fault constitutive behavior.

A second way to resolve the trade off of slip weakening distance with strength excess might be to follow a suggestion made by Scholz (1988) and Ide and Takeo (1997) that slip weakening distance is long where there are no aftershocks. Such an interpretation might resolve some paradoxes. Ide and Takeo (1996) correlated high strength excess in the 1993 Kushiro-Okii earthquake with an abundance of aftershocks,

whereas Fukuyama and Mikumo (1993) correlated high values of strength excess on the 1990 Izu-Oshima rupture surface with a lack of aftershocks. The spatial correlation of Ide and Takeo (1996, their Plate 2) is rather problematic, as they show a region of high strength excess on the west part of the fault having many aftershocks, but they show regions of high strength excess on the east corner of the fault having very few aftershocks and a region of low strength excess around the hypocenter having very few aftershocks. For both earthquakes a preferable interpretation would be that a region of long slip weakening distance rather than high strength excess stops the rupture in regions where there are few aftershocks. This possibility must not be ignored in future dynamic modeling of earthquake ground motion data.

Moreover, we can obtain the distribution of the upper bound of slip-weakening distance over the fault plane from the distribution of slip implied by the smallest detectable aftershocks mapped over the fault plane where the mainshock occurs (Aki, 1987). Of course, such an estimate of the upper bound should also account for the effects of the earthquake detection threshold, the time of surface contact on the slip-weakening distance (Nakatani, 1997; Aochi and Matsu'ra, 1999), and the structural changes of the fault surfaces occurring during rupture. Nevertheless, it would provide an estimate of the order of magnitude of the upper bound of slip-weakening distance that would certainly help reduce the non-uniqueness discussed in this study.

3.5 Conclusions

At present from strong ground motion studies we have very little information about constitutive relations because, with a few possible exceptions, it is not clear that any waveform modeling inversion of an earthquake source has resolved time scales shorter than the rise time.

The main result of our study is even more gloomy than the above conclusion, namely, waveform inversion of the best existing strong motion data set will probably be unable to determine the strength excess and slip weakening distance uniquely. The fundamental ambiguity is that strength excess and slip weakening distance have competing effects on rupture velocity, which largely controls the waveforms. In our

inversion we modeled the waveforms at periods that were one third of the rise time, and we found two rupture models, A and B, having different strength excesses and slip weakening distances, but both models produced waveforms that were essentially indistinguishable.

However, our work shows that fracture energy might be much more stably estimated from waveform inversions. Our models A and B had very similar fracture energies. While we did not invert real data, our models A and B show that an event of the size of the Imperial Valley earthquake has a fracture energy of about $2\text{-}6 \times 10^6 \text{ J/m}^2$, which agrees well with the $2 \times 10^6 \text{ J/m}^2$ obtained by Beroza and Spudich (1988) for the Morgan Hill earthquake. However, during the Imperial Valley event the rupture velocity was inferred to be supershear over a portion of the fault plane (Archuleta, 1984; Spudich and Cranswick, 1984), while in the models presented in this study the rupture propagate at a subshear velocity. Due to this discrepancy our estimate of apparent fracture energy probably overestimates that for the 1979 Imperial Valley earthquake. Previous theoretical studies explain why fracture energy might be a stable inversion parameter. These studies show that rupture velocity is controlled by fracture energy if stress drop is fixed. For a slip-weakening model, Ida (1972) and Andrews (1976a; 1976b) give analytical expressions that relate the apparent fracture energy to rupture velocity in the case of uniform stress drop. In these relations the rupture velocity is determined by the ratio of the apparent fracture energy G_c with a parameter that depends on the square of the stress drop. Thus, if we know an earthquake's stress drop distribution from its slip distribution obtained by a ground motion inversion, the earthquake's rupture velocity will constrain the apparent fracture energy for the event. As a given kinematic model is consistent with a broad range of values of strength excess and slip-weakening distance, so also is a given distribution of fracture energy nonuniquely related to these two parameters. Nevertheless, the fracture energy is a fundamental parameter for describing earthquakes in terms of the physics, and provides important insights into the rupture process

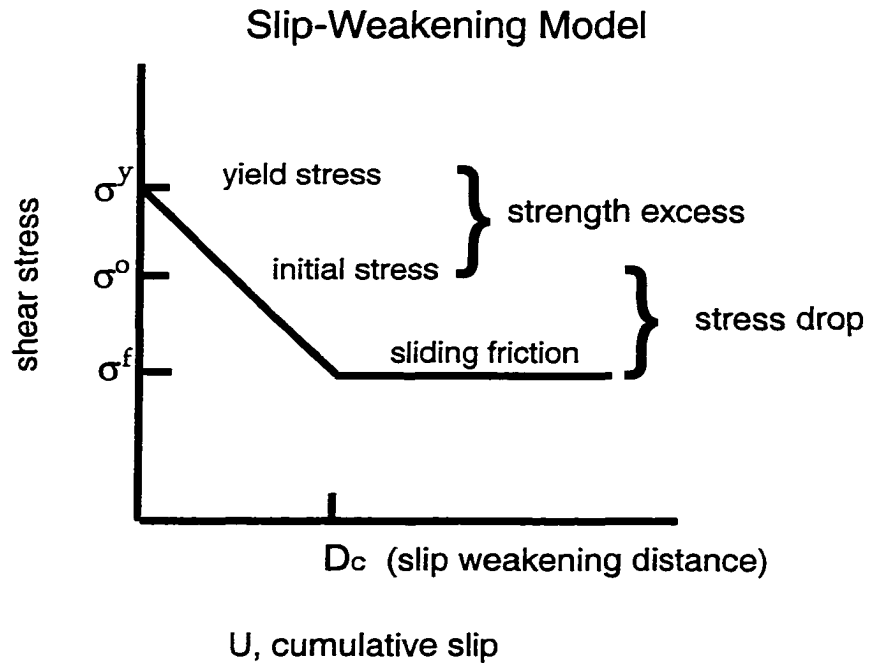


Figure 3.1. Slip-weakening friction law (Ida, 1972; Day, 1982; Andrews, 1985). The curve represents the total shear stress as a function of cumulative slip.

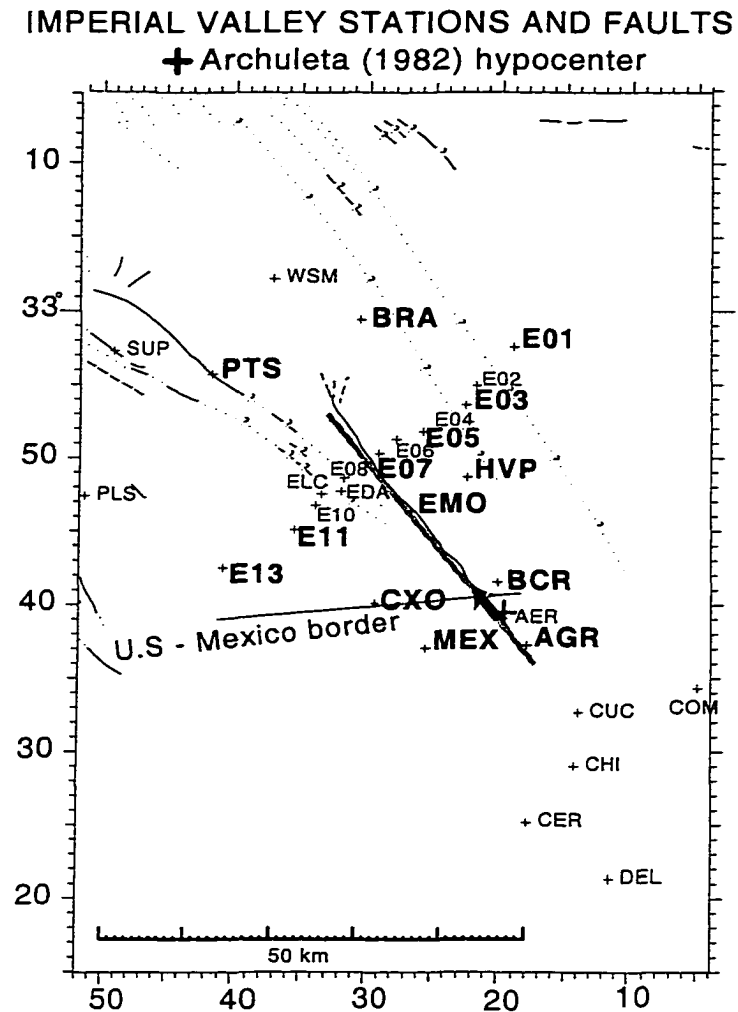


Figure 3.2. Map showing surface trace of the Imperial Fault and the stations that recorded the 1979 earthquake. In this study we have calculated synthetic seismograms at the stations shown in bold characters. The thick line corresponds to the fault plane used in our modeling, and the arrow shows the direction of rupture propagation. Cross is the hypocenter.

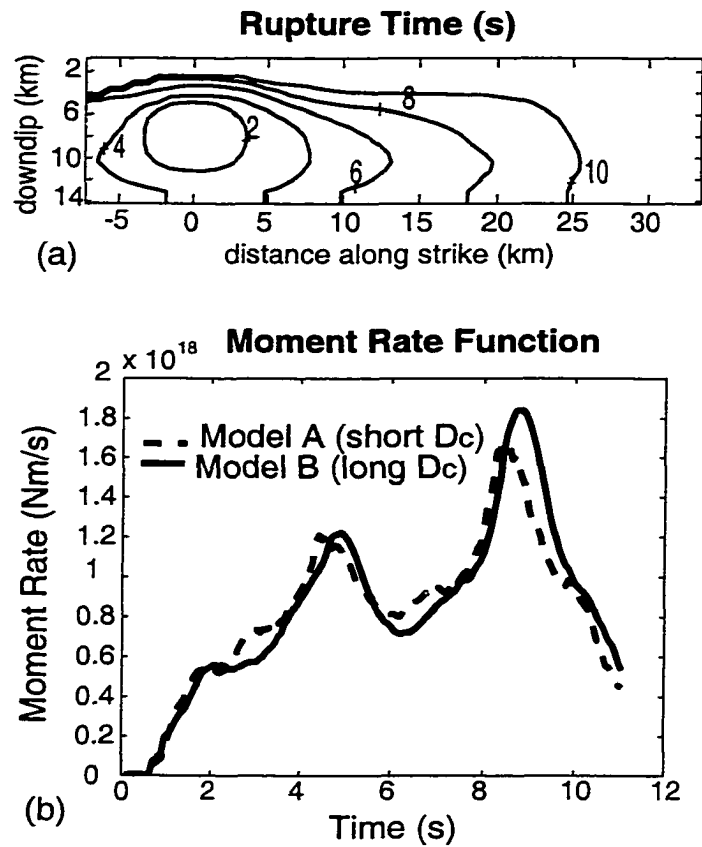


Figure 3.3. (a) Rupture time distribution for both Model A and Model B. We impose the reference model's rupture time distribution on both models (constraint K2 in Chapter 2). (b) Moment rate function for Model A (dashed line) and Model B (continuous line). We force both models to be consistent with the moment rate function of the reference model (constraint K1 in Chapter 2).

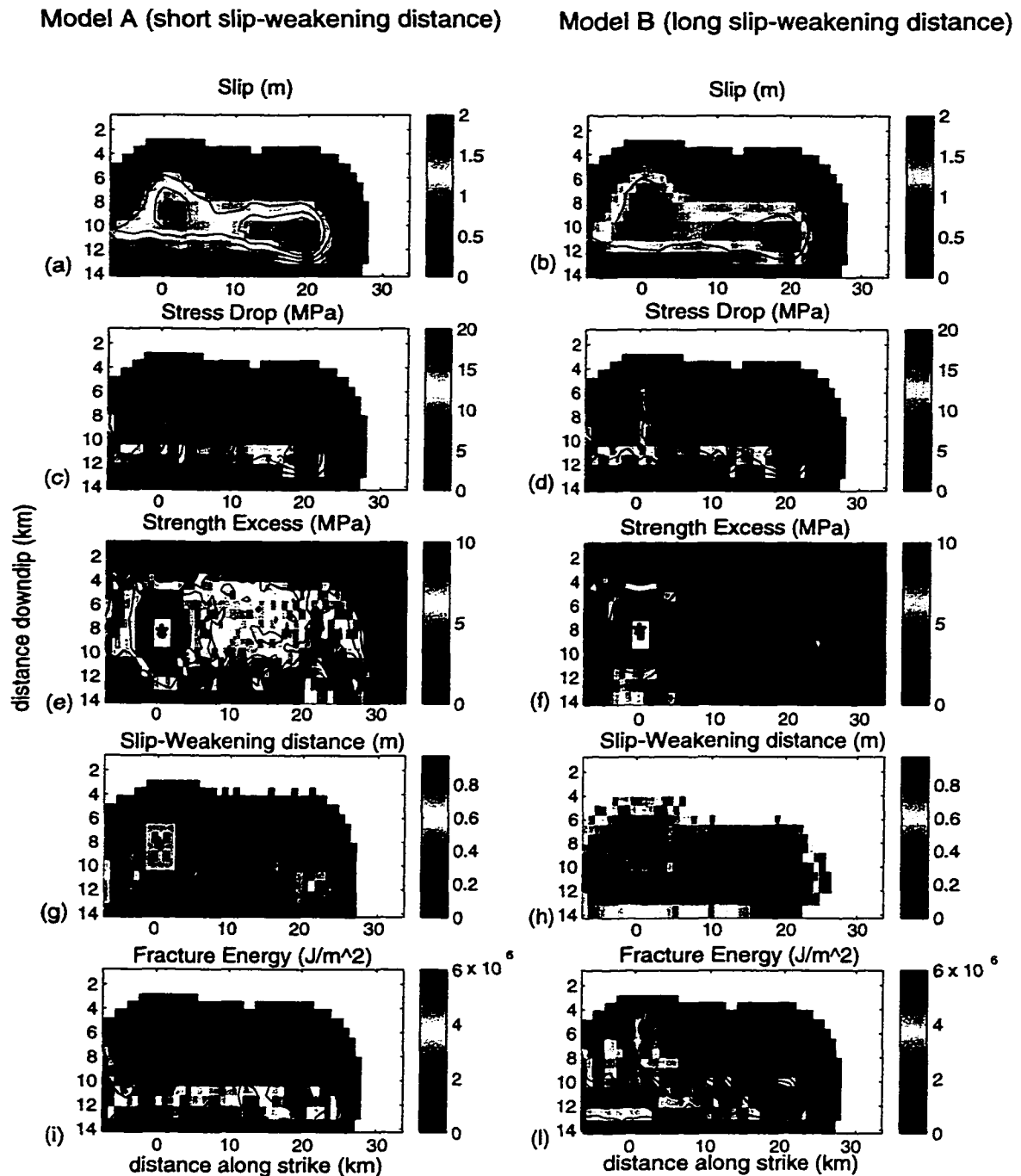


Figure 3.4: Distribution of kinematic and dynamic parameters on the fault plane (the asterisk indicates the hypocenter location) for Model A (left) and Model B (right). Slip distribution (a) and (b); stress drop distribution (c) and (d); strength excess distribution (e) and (f); slip-weakening distance distribution (g) and (h); apparent fracture energy distribution (I) and (I). Note that the two models have very similar slip and stress drop distributions, as required by the constraints imposed, while they have very different strength excess and slip-weakening distance distributions, due to the existing trade-off between these two parameters in controlling the rupture velocity. The similarity between the apparent fracture energy distribution for the two models suggests that this parameter might be relatively stably estimated from waveform inversions.

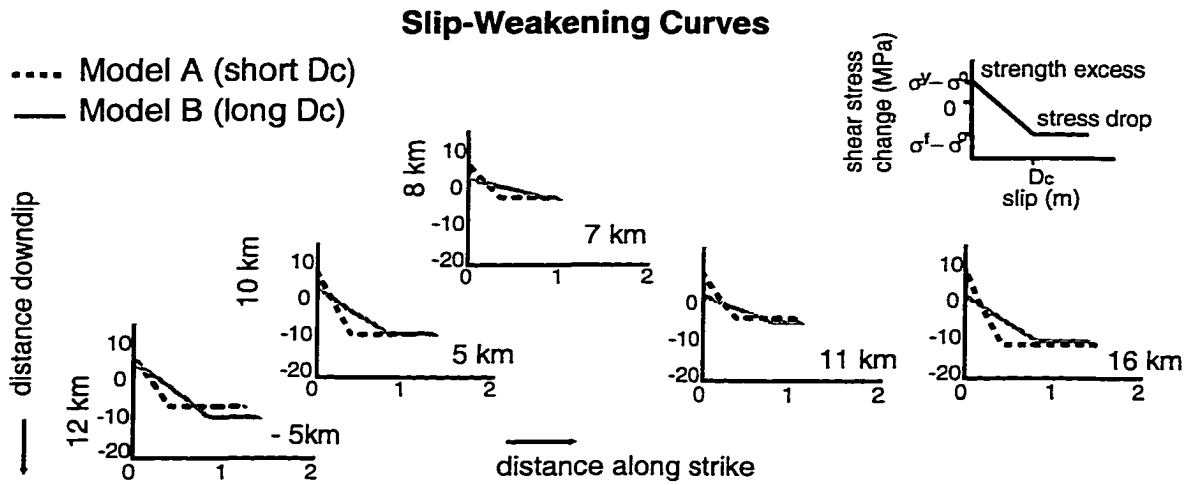


Figure 3.5. Slip-weakening curves at selected subfaults for Model A (dashed line) and Model B (continuous line) at different position along strike and different depths. We impose a fast weakening to Model A (resulting in a slip-weakening distance of about 0.3m) and a slow weakening to Model B (resulting in a slip-weakening distance of about 1m). Note that for Model A the strength excess is systematically larger than that for Model B.

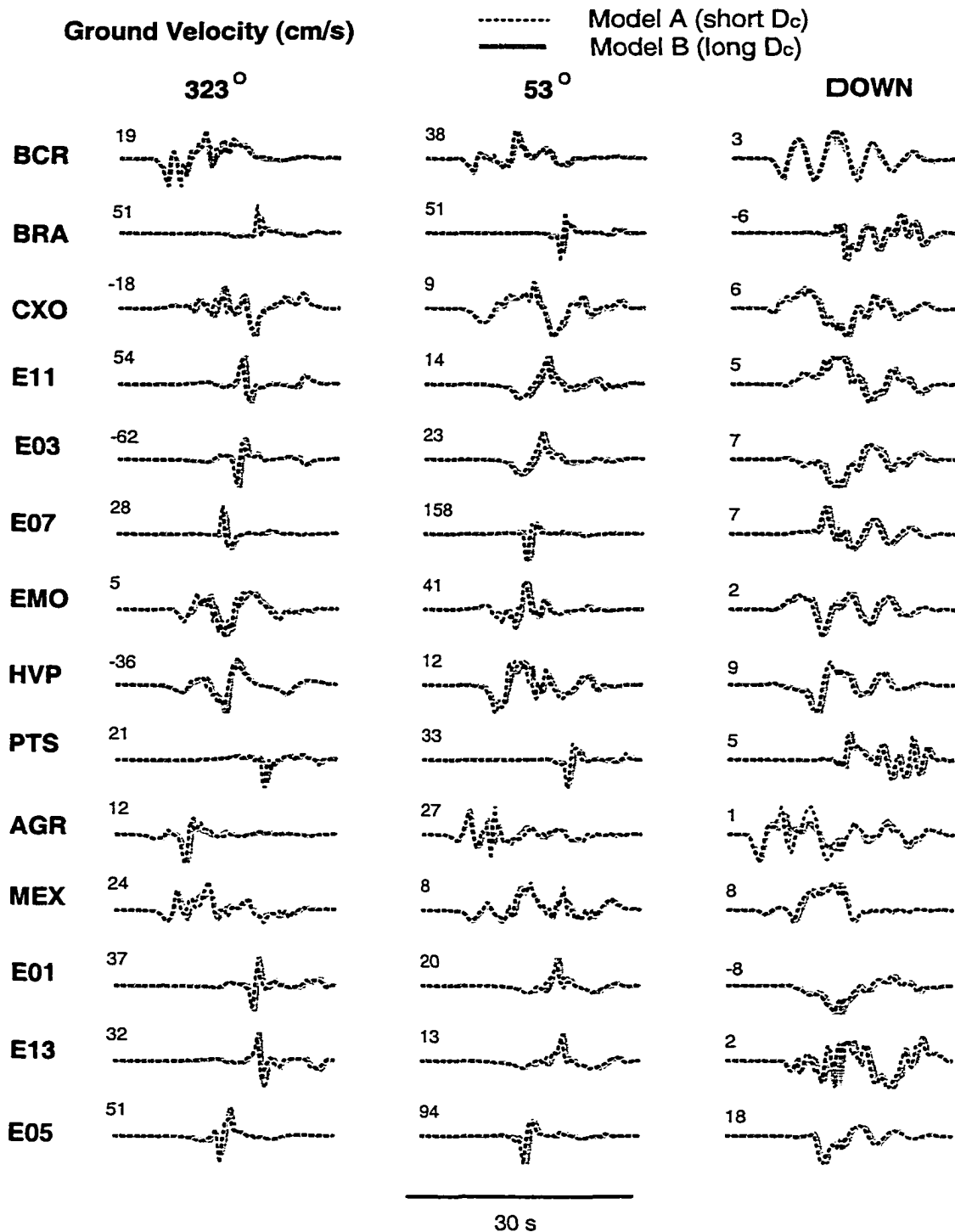


Figure 3.6. Synthetic seismograms resulting from Model A (dashed line) and Model B: (continuous line). We show the three components of ground velocity (cm/s) calculated at the stations shown in Figure 2; the number on the upper left corner of each trace indicates the respective maximum amplitude. The synthetics are calculated up to 1.8 Hz and then lowpassed with a cosine taper between 1 and 1.8 Hz. The similarity between the Model A and B waveforms shows that it would be very difficult to distinguish between these models by waveform inversion.

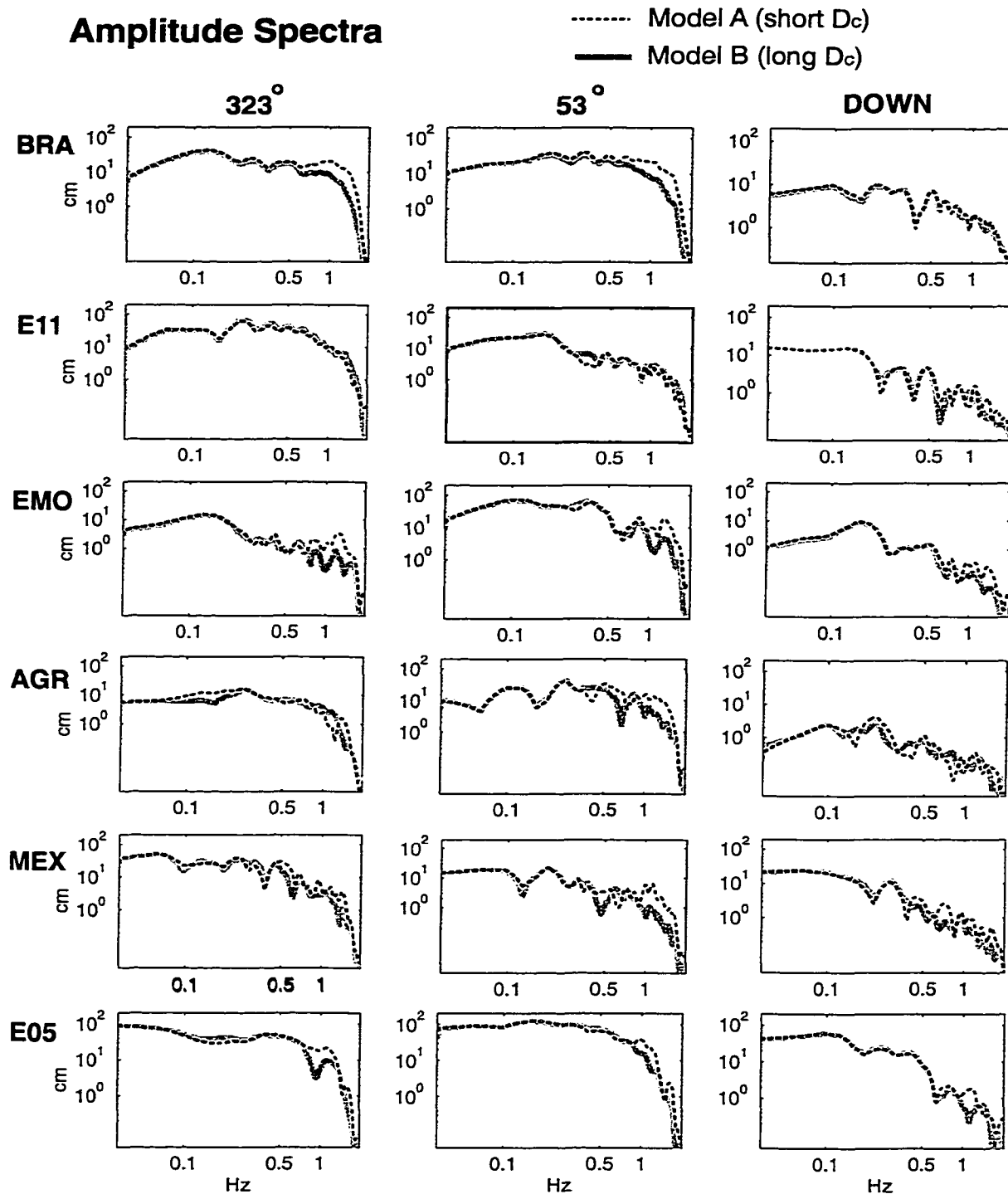


Figure 3.7: Amplitude spectra resulting from Model A (dashed line) and Model B (continuous line) for selected stations. In general, Model A radiates more energy at frequencies above about 1 Hz than Model B. This is particularly evident at stations in the forward directivity region (BRA), close to the fault (EMO) and in the backward directivity region (AGR and MEX), while the differences between the two models are almost negligible at stations more distant from the fault (E11). These amplitude spectra are derived from synthetics calculated up to 1.8 Hz and then lowpassed with a cosine taper between 1. and 1.8 Hz.

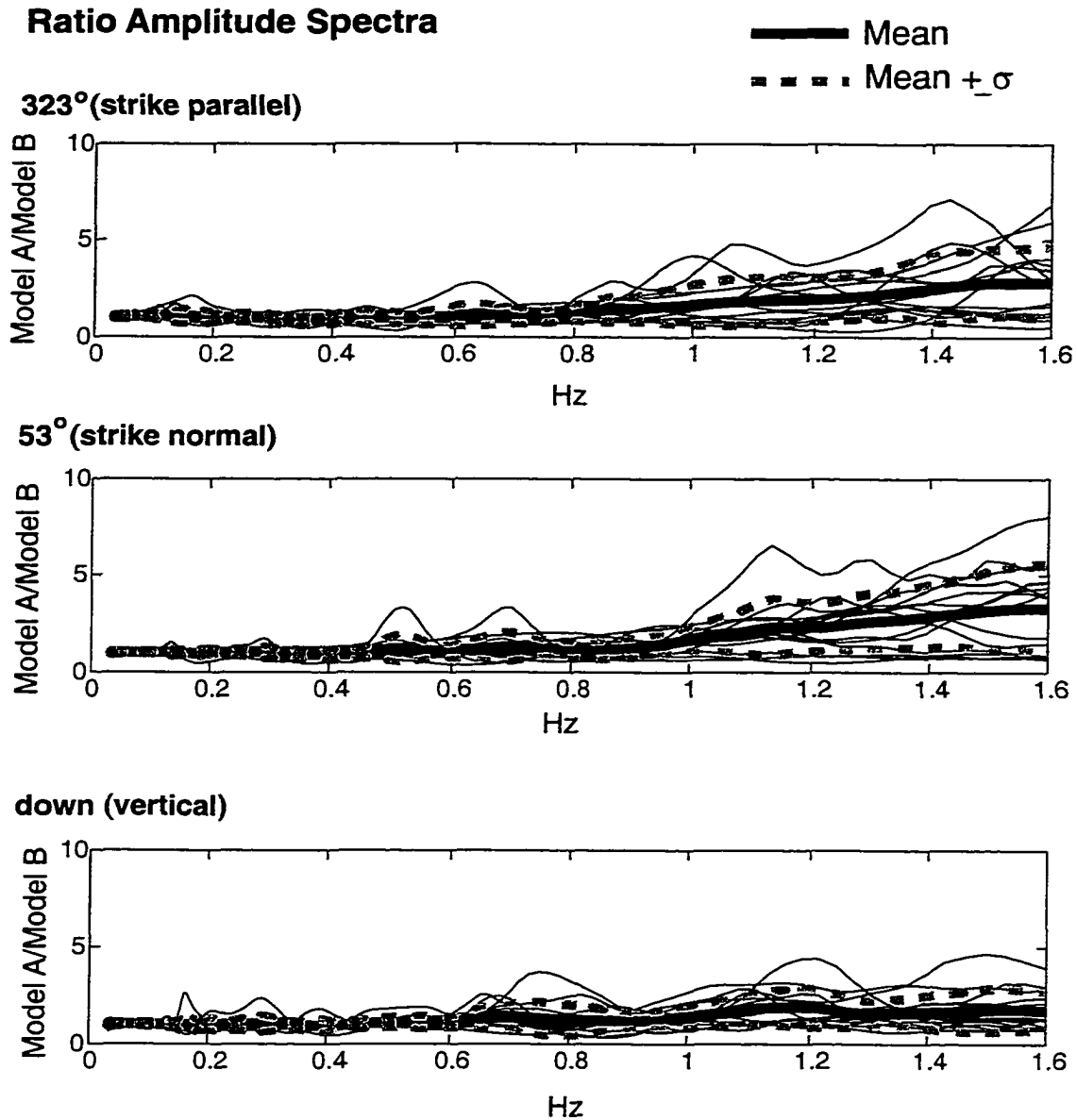


Figure 3.8: Ratio between the smoothed amplitude spectra of Model A and those of Model B. For each component of motion we show the amplitude spectra ratio calculated at each station (thin lines) and the mean calculated among all the observations (thick line). The thick dashed lines are the mean \pm the standard deviation. For the two horizontal components the mean of the amplitude spectra ratio is above 1 for frequencies larger than about 1 Hz, reaching a value of about 2.5 at 1.6 Hz. This means that Model A radiates more energy above about 1 Hz than Model B, and that the two models are equivalent at low frequencies, while the differences in the details of the rupture models are evident only at high frequency.

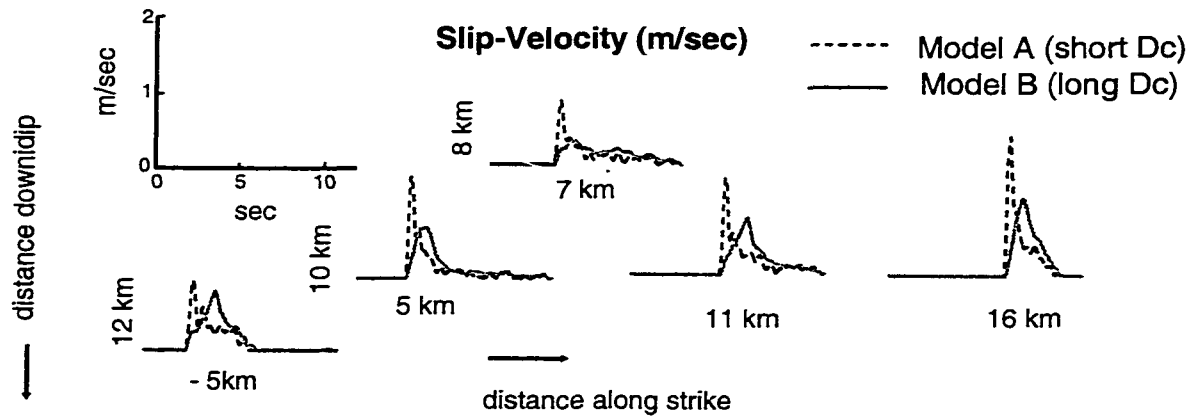


Figure 3.9. Slip-velocity histories (or source time functions) for Model A (dashed line) and Model B (continuous line) at different positions along strike and at different depths as in Figure 5. The source time functions for Model A have larger peak slip-velocity, faster decay, and the same total slip as those of Model B, for which the slip-velocity follows a typical triangular shape (or an overlapping of different triangular functions).

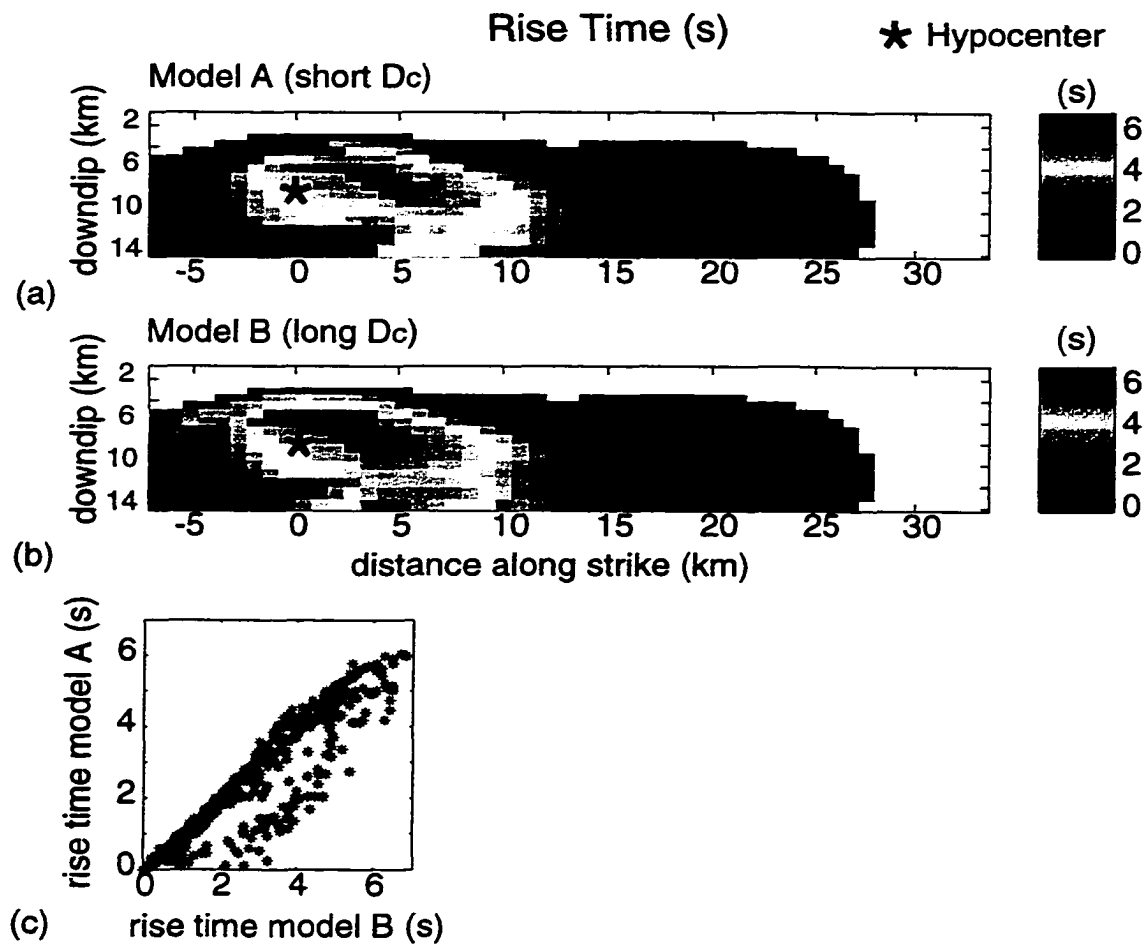


Figure 3.10. Comparison of rise time distribution (calculated as the time required to cumulate 10% to 90% of the final slip) between Model A (a) and Model B (b). The similarities between the two distributions imply that the analysis of this parameter would not help distinguish the two models. (c) Rise time of Model A plotted as a function of rise time of Model B.

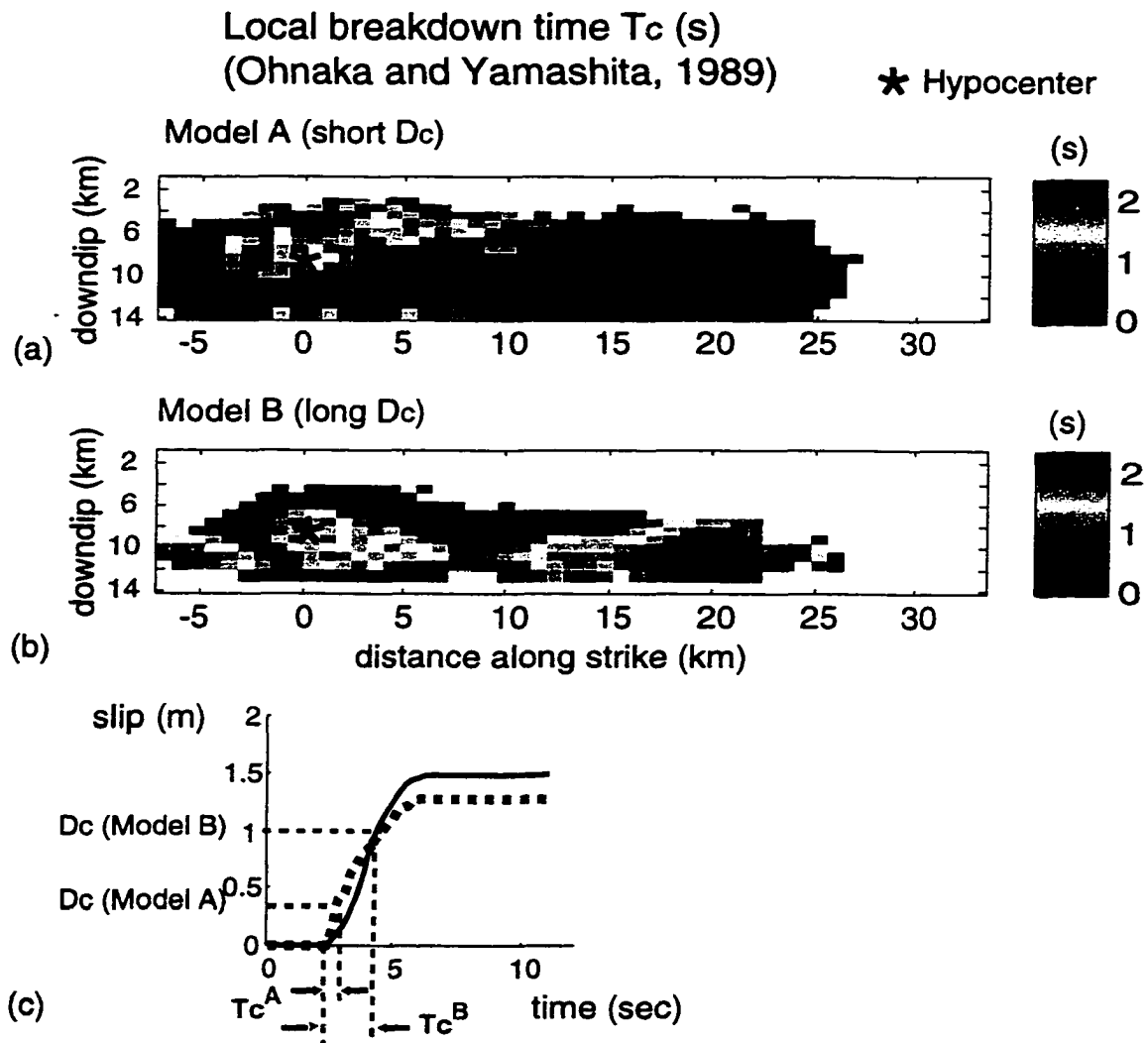


Figure 3.11. Comparison of local breakdown time distribution (defined as the time over which the weakening occurs) between Model A (a) and Model B (b). The local breakdown time for Model A is systematically shorter than that in Model B, as we should expect from the difference in the rate of weakening characteristic of the two models. (c) Local breakdown time for the two models relative to the respective slip histories.

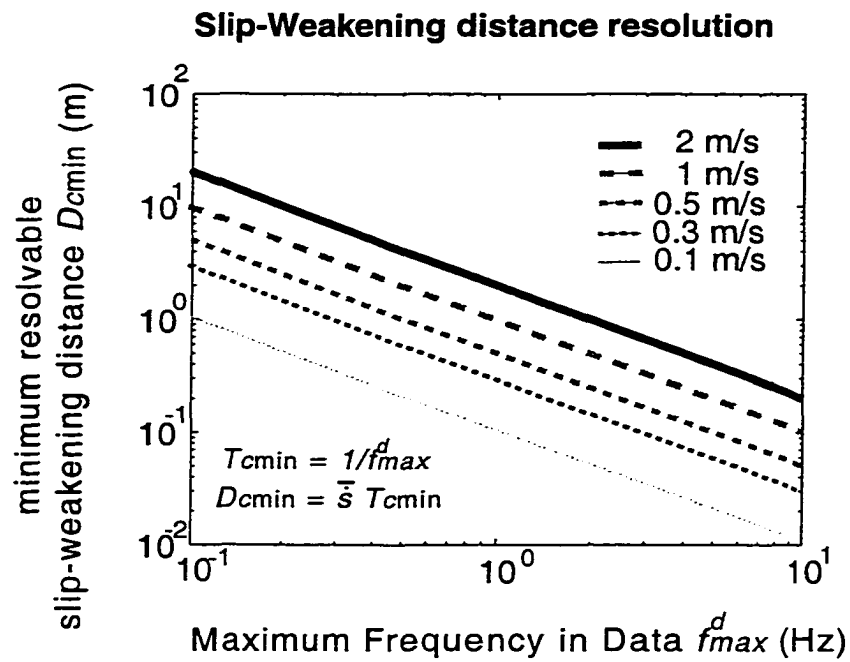


Figure 12: Slip-weakening distance resolution as a function of the maximum frequency contained in the data used for inferring a source model. The different lines correspond to different values of average slip-velocity in the early part of slip as representative of average slip-velocity during weakening.

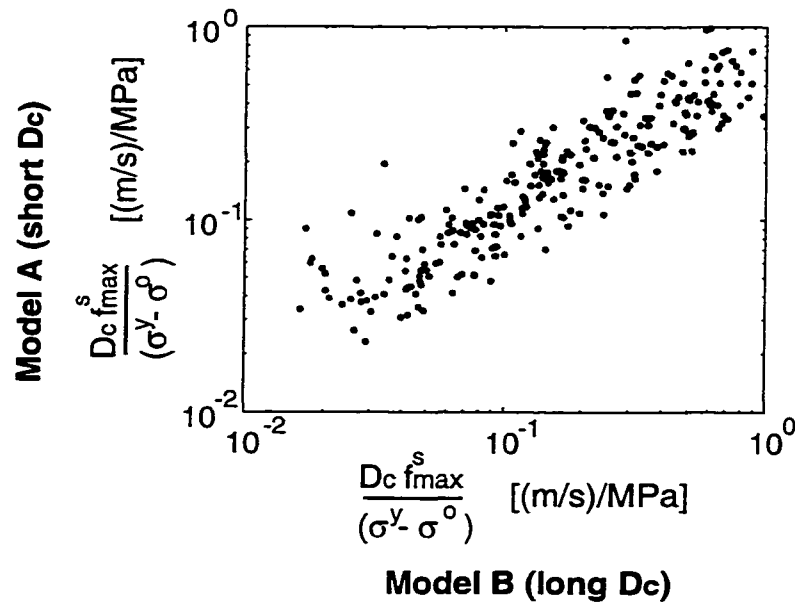


Figure 3.13. $\frac{d_c f_{\max}^s}{(\sigma^y - \sigma^o)}$ for Model A as a function of $\frac{d_c f_{\max}^s}{(\sigma^y - \sigma^o)}$ for Model B, where $f_{\max}^s = 1/T_c$

(Ohnaka and Yamashita, 1989). This figure shows that this ratio is roughly the same for both models. In fact, following Ohnaka and Yamashita (1989), this ratio is a function of the rupture velocity and shear modulus, and therefore is expected to be the same for both models. This constrain might be used to apply spectral analysis to broadband data to reduce the dynamic nonuniqueness discussed in the paper.

Chapter 4 - Inferring Rate and State Friction Parameters from a Rupture Model of the 1995 Hyogo-ken Nanbu (Kobe) Japan Earthquake

- 4.1 Introduction
- 4.2 Rate- and State-Variable Friction
- 4.3 Frictional Parameters from Strong Ground Motion Data
- 4.4 Results
- 4.5 Conclusions

Abstract

I consider the applicability of laboratory-derived rate- and state- variable friction laws to the dynamic rupture of the 1995 Kobe earthquake. I analyze the shear stress and slip evolution of Ide and Takeo's (1997) dislocation model, fitting the inferred stress change time histories by calculating the dynamic load and the instantaneous friction at a series of points within the rupture area. For points exhibiting a fast-weakening behavior, the Dieterich-Ruina friction law, with values of $d_c = 0.01-0.05$ m for critical slip, fits the stress change time series well. This range of d_c is 10-20 times smaller than the slip distance over which the stress is released, D_c , which previous studies have equated with the slip-weakening distance. The limited resolution and low-pass character of the strong motion inversion degrades the resolution of the frictional parameters and suggests that the actual d_c is less than this value. Stress time series at points characterized by a slow-weakening behavior are well fitted by the Dieterich-Ruina friction law with values of $d_c \geq 0.01-0.05$ m. The apparent fracture energy, G_c , can be estimated from waveform inversions more stably than the other friction parameters. I obtain a $G_c \approx 1.5 \times 10^6$ Jm⁻² for the 1995 Kobe earthquake, in agreement with estimates for previous earthquakes. From this estimate and a plausible upper bound for the local rock strength we infer a lower bound for D_c of about 0.008 m.

4.1 Introduction

The diversity and complexity of rupture models for past earthquakes suggests that properties that control rupture evolution are spatially heterogeneous and may vary strongly for different earthquakes. Understanding the prevailing constitutive relation and the relevant parameters could provide a unifying physical basis for understanding this variability and heterogeneity in the faulting process.

Laboratory measurements of rock friction (e.g. Dieterich, 1978; Weeks and Tullis, 1985) at low sliding velocities can be interpreted by rate- and state-variable (RSV) friction laws (Dieterich, 1979; 1981; Ruina, 1983) that describe the evolution of frictional stress as function of slip-rate, and state. Rate- and state-variable friction laws are capable of explaining such diverse aspects of quasi-static earthquake occurrence as Omori's law of aftershock decay (Dieterich, 1994), earthquake nucleation (Dieterich, 1994; Dieterich and Kilgore, 1996a), the lack of tidal triggering of earthquakes (Heaton, 1982; Dieterich, 1987; 1994), and the time behavior of creep on faults (Tse and Rice, 1986; Marone *et al.*, 1991). In this study we focus on the application of RSV friction laws to frictional behavior during the dynamic rupture of a real earthquake. It is not certain that RSV friction laws govern friction on natural faults during earthquakes. Other phenomena, such as melting or fluid pressurization (Tsutsumi and Shimamoto, 1997), extreme velocity weakening (Heaton, 1990), and wrinkle-like slip pulses (Andrews and Ben-Zion, 1997), have been proposed to act during earthquakes. However, no one has yet disproved that RSV friction governs dynamic earthquake slip, and the success of RSV friction in explaining low-slip-speed phenomena encourages us to examine its applicability to high speed dynamic slip.

Many previous dynamic rupture models have assumed a simple slip-weakening model as the governing equation of crack propagation (Andrews, 1976; Day, 1982; Andrews, 1985). Figure 4.1 presents a simple realization of a slip-weakening model, which is characterized by a linear decrease in fault strength from a peak stress τ^p to a residual stress τ^f over a slip increment D_c . This constitutive model was introduced by Ida (1972) and Palmer and Rice (1973) for shear cracks using the notion of crack-tip cohesive zone introduced by Barenblatt (1959) for tensile cracks. The introduction of the cohesive zone removes the physically unrealistic singularity that characterizes the purely elastic-brittle crack tip stress field

Recently, Ide and Takeo (1997) and Olsen *et al.* (1997) considered fault constitutive parameters during dynamic rupture of real earthquakes, focussing on the estimate of the slip-weakening distance in the framework of a simple slip-weakening model (Fig. 4.1). They propose values for D_c of the order of 0.2 to 1 m, several orders

of magnitude larger than the values observed in laboratory experiments. This slip-weakening law might be appropriate for modeling a single earthquake (Okubo, 1989), but is inadequate to explain other aspects of earthquake behavior, such as the restrengthening of faults between earthquakes. Furthermore, the experiments performed by Okubo and Dieterich (1984, 1986) show that the defining parameters of the slip-weakening model, the peak stress τ^p and the residual stress τ^f , are not material properties because they vary from place to place on an homogeneous rock sample.

Experimental results and observational evidence supported by numerical modeling of the earthquake cycle (Tse and Rice, 1986; Ben-Zion and Rice, 1997; Lapusta *et al.*, 1999) suggest that rate- and state- variable friction might be a simple unifying law for the entire cycle of the faulting process. However, open questions concerning the scaling of constitutive parameters from laboratory to the field greatly limit the application of such laboratory-derived constitutive laws to the rupture process of real faults.

Okubo and Dieterich (1984; 1986) designed experiments to observe dynamically propagating stick-slip events in the laboratory, and found that the rate- and state-dependent friction model could explain both quasi-static and dynamic fault slip behaviors. Their data also suggest that friction becomes velocity-independent at high speed so that the process resembles slip-weakening. Ohnaka, Kuwahara and Yamamoto (1987), and Ohnaka and Kuwahara (1990) also observed a predominant slip-weakening friction behavior during stick-slip laboratory experiments.

In this study we address the applicability of laboratory-derived rate- and state-variable friction laws to the dynamic rupture of the 1995 Kobe earthquake as represented by the kinematic rupture model obtained by Ide and Takeo (1997) from inversion of strong motion data. We focus on the estimate of the critical slip, d_c , and, although estimates of rate- and state-friction parameters are not well constrained by our methodology, we compare them with those obtained from stress triggering studies. We also provide an estimate of fracture energy for this earthquake, from which we derive a lower bound on the slip-weakening distance, D_c .

4.2 Rate- and State-Variable Friction

Rate- and state-variable friction constitutive relations were developed to explain laboratory observations of a variety of sliding phenomena under quasi-static conditions along simulated fault surfaces (Dieterich, 1978; 1979), and a simple explanation of them can be found in Scholz (1990, pp.79-83).

Several similar formulations of rate- and state-variable friction have been employed. A first-order simplification of Dieterich's original friction law is the following (Okubo and Dieterich, 1986):

$$\mu = \mu_0 + B \ln(b_1 \vartheta + 1) - A \ln\left(\frac{a_1}{v} + 1\right), \quad (4.1)$$

where, v is slip-velocity, μ is coefficient of friction, μ_0 is a reference value of friction, ϑ is the state variable, that, in the interpretation of Dieterich (1981), is the effective lifetime of population contacts. A , B , a_1 and b_1 are empirically determined coefficients. A controls the direct effect, B controls the evolution effect, and a_1 and b_1 are cutoff parameters to the rate and state dependence, respectively.

Ruina (1983) proposed a simpler form for the variation of the coefficient of friction, and suggested that the state variable can be identified with different physical properties, depending on the specific problem formulation and experimental conditions. His formulation is the following:

$$\mu = \mu_0 + B \ln(\vartheta/\vartheta^*) + A \ln(v/v^*), \quad (4.2)$$

where v^* and ϑ^* are normalizing constants.

A simple form for the evolution of the state variable with fault offset is given by:

$$\frac{d\vartheta}{dt} = 1 - \frac{\vartheta v}{d_c}, \quad (4.3)$$

where d_c is the critical slip distance. Our choice of equation (3) to describe the evolution of the state variable was motivated by its extensive use in the literature (e.g. Dieterich, 1981, 1986; Okubo, 1989).

For sliding at constant slip-rate v , the state evolution can be expressed as

$$\vartheta(t) = \frac{d_c}{v} + \left(\vartheta_0 - \frac{d_c}{v} \right) \exp\left(\frac{u_0 - u(t)}{d_c} \right), \quad (4.4)$$

where ϑ_0 and u_0 are the values of ϑ and fault displacement u at which constant velocity sliding at v is initiated. d_c controls the length scale of the exponential decay.

In this study we will refer to equation 4.1 as the Dieterich equation or full model, and to equation 4.2 as the Dieterich-Ruina equation or simplified model. For the characteristic low slip-rates of quasi-static sliding experiments, it is straightforward to see that the Dieterich equation 4.1 is equivalent to the Ruina formulation (equation 4.2), and the mathematically simpler constitutive law, equation 4.2, is often used.

4.2.1 Laboratory Observations of Friction During Dynamic Slip

Okubo and Dieterich (1984; 1986) suggested that a rate- and state-variable friction constitutive formulation is also appropriate to model laboratory observations of generation and propagation of stick-slip frictional instabilities along simulated faults at high slip speeds. Their observations on 2m-square granite blocks include slip-velocities as high as 0.19 m/s, roughly three or four orders of magnitude larger than speeds used in quasi-static tests, and for jumps in velocity as much as six orders of magnitude larger than those that characterize quasi-static experiments. Under these conditions, equation 4.1 and equation 4.2 are not equivalent, and the cutoffs to both the rate and state dependencies (a_l and b_l in equation 4.1) become important. Thus, stick-slip data suggest that friction becomes velocity-independent at high speed so that the process resembles slip-weakening.

More recent laboratory observations of stick-slip by Tsutsumi and Shimamoto (1997) suggest that at high slip-speed and large displacement sliding frictional heating can occur resulting in an enhanced velocity-weakening behavior, and causing frictional properties to change with displacement.

Okubo (1989) points out that a simple slip-weakening model (Fig.4.1) and the frictional response observed after a positive velocity step describe a similar frictional behavior. Furthermore, the effect of high-speed cutoffs in equation 4.1 enhances this

similarity. He points out, however, that both the peak frictional resistance and the residual frictional strength can depend on fault slip-rate in the state variable formulation, and that the state variable friction formulation includes no explicitly displacement-dependent effects. This difference reveals the similarities between the two friction models to be mainly phenomenological, and separates the physical interpretation of their respective defining constitutive parameters.

4.2.1.1 Critical Slip and Slip-Weakening Distance

In this study we will use d_c to refer to the critical slip in the rate- and state-variable friction formulation, while D_c will be used to indicate the slip-weakening distance in the slip-weakening model (Fig.4.1). As we will point out later, these two slip parameters should not be confused.

The critical displacement d_c in the rate and state-variable friction formulation represents the amount of slip required to renew a contact population consistent with the new sliding velocity. This critical slip parameter is one of the key factors controlling fault instability and the size of the earthquake nucleation zone (Rice and Ruina, 1983; Dieterich, 1986). In laboratory friction experiments d_c has been found to increase with surface roughness (Okubo and Dieterich, 1984), and to be controlled by the thickness of the zone of localized shear strain for experiments in which simulated gouge is present (Marone and Kilgore, 1993). Typical d_c values derived from lab measurements of friction are in the range of μm - mm .

Dieterich and Kilgore (1994; 1996b) have investigated the contact processes between roughened surfaces and have imaged the actual areas of contact for a wide variety of materials. Based on their observations, they interpret d_c as the average size of contact population, and they found it to be directly related to the composite fracture surface topography, which is an observable property of the surface.

Scholz (1988) has addressed the problem of how d_c scales from lab measurements to geological scales. He proposed to relate the critical slip displacement to the maximum contact spacing between two fractal surfaces under a normal load. Using some fault topographic data he roughly estimated d_c to be in the range of 10^{-2} - 10^{-3} m at seismogenic depths. This estimate is consistent with the value of d_c of about 1 cm that

Tse and Rice (1986) used to simulate natural faulting phenomena using a rate- and state-dependent formulation.

In contrast, estimates of the slip-weakening distance D_c for real earthquakes suggested that this slip parameter can take values of the order of several cm to about 1 m on natural faults (Papageorgiou and Akı̄, 1983; Ide and Takeo, 1997; Olsen *et al.*, 1997; Shibazaki and Matsu'ura, 1998). Ide and Takeo (1997) and Olsen *et al.* (1997) have proposed values of D_c ranging between 0.2 to 1 m for the 1995 Kobe earthquake and the 1992 Landers earthquake, respectively. Their inferences are based on the assumption that a simple slip-weakening characterization describes the frictional behavior during dynamic rupture. As discussed in the introduction, however, simple slip-weakening might be an inadequate description of fault constitutive properties because is not able to represent the full range of phenomena represented by rate- and state-variable models and observed in laboratory experiments. Furthermore, these estimates of D_c should not be confused with the constitutive parameter d_c , in the rate- and state- variable friction formulation.

4.3 Frictional Parameters from Strong Ground Motion Data

4.3.1 Overview of Ide and Takeo (1997) Results

In this study we apply our procedure to determine rate- and state-variable friction parameters during the dynamic rupture of the 1995 Kobe, Japan earthquake consistent with the dislocation model of Ide and Takeo (1997). These authors inverted strong motion data in a frequency range of 0.025 - 0.5Hz using an inversion method that used the ABIC criterion to determine the optimal smoothing. The rupture process is described through slip-rate functions given at grid points at 1 km spacing over a single planar fault. . Figure 4.2 shows their inferred slip distribution over the fault plane, and the grids with thick borders indicate the location of the grid points used in their analysis.

Ide and Takeo (1997) estimated D_c for the 1995 Kobe earthquake. They first calculated the spatio-temporal evolution of shear stress change from their dislocation model using a finite difference method with the slip distribution as a boundary condition. Then, by visually analyzing the stress-slip curves at 10 selected subfaults

they determined that the rates of weakening in the shallow parts of the fault are significantly smaller than those in the deeper parts.

Figure 4.3 shows a few examples of stress-slip curves representative of different rate of weakening for various depths. In this study we will refer to “fast-weakening” and “slow-weakening” subfaults to characterize such curves. The “slow-weakening” subfaults are those in which the stress drops over a large fraction of the total slip.

To investigate the limits of their analysis, Ide and Takeo (1997) performed a resolution test and concluded that their estimated values of D_c of about 0.5 m for deeper regions should be considered only an upper limit of D_c . On the other hand, they state that “ [...] it is plausible that the (constitutive) relations on the shallower part is well determined by our method. The slip-weakening rate may be small or the critical displacement D_c is large in the shallow crust”. They suggest that D_c might be 1 m or more in the shallow region.

4.3.2 Our Method

Our method is similar to the Ide and Takeo (1997) procedure and follows the approach of Okubo and Dieterich (1986) to model laboratory records of fault displacement and shear stress during stick-slip failures on a simulated fault within a rate- and state-variable friction formulation.

We first apply the method of Spudich *et al.* (1998) to duplicate the spatio-temporal evolution of shear stress change calculated by Ide and Takeo (1997). The time histories of slip-velocity and shear stress change provide the observational parameters to which we fit a rate- and state-variable friction law rewritten in terms of shear stress change for equation 4.1:

$$\tau - \tau^0 = (\sigma\mu_0 - \tau^0) - A\sigma \ln\left(\frac{a_1}{v} + 1\right) + B\sigma \ln(b_1\vartheta + 1), \quad (4.5)$$

or equation 4.2:

$$\tau - \tau^0 = (\sigma\mu_0 - \tau^0) + A\sigma \ln\left(\frac{v}{v^*}\right) + B\sigma \ln\left(\frac{\vartheta}{\vartheta^*}\right), \quad (4.6)$$

where, σ is normal stress and τ^0 is initial shear stress. The parameters that we attempt to determine are: $(\sigma\mu^0 - \tau^0)$, d_c , $A\sigma$, $B\sigma$, a_l and b_l .

We select grid points mostly along the Nojima fault that correspond to the patches of largest slip, that we presume are better resolved from the strong ground motion modeling. The subfault locations selected for this study are highlighted in Figure 4.2.

4.3.3 Fitting Procedure

We first fit the full model to the stress change time series from a subset (14 subfaults) of our selected observations (the 71 subfaults highlighted in Figure 4.2) to test whether the cutoff parameters a_l and b_l are resolvable and statistically significant. The fitting procedure described in this section is valid for both the full and the simplified models.

In equations 4.5 and 4.6 the slip-velocity, v , and the state, ϑ , are the predictors for the shear stress change, τ . The slip-velocity history is provided by the dislocation model, and the shear stress history is calculated as discussed above. For each selected grid point, we then need to determine the state variable history. In the Dieterich interpretation of state parameter, the initial condition for this variable, ϑ_0 , represents the time since the last episode of stick-slip has occurred on the Nojima fault. In this study we assume two extreme values, one of about 1 month, and one of about 1000 years, in order to test the sensitivity of our estimates to the state variable. Given the recurrence time for the Nojima fault, we believe that the second choice is the more appropriate for this analysis, and therefore we will show the results obtained assuming that initial condition. However, because we cannot account for quasi-static rupture nucleation, an initial state of 1000 years might be an overestimate for this parameter around the nucleation region. In general, a larger value of ϑ_0 mainly results in smaller fitted d_c , and larger $B\sigma$, i.e. an enhanced evolution effect is needed in order to fit the stress histories. However, between the two extreme values of ϑ_0 that we tested, the inferred parameters

d_c and $B\sigma$ vary by at most a factor of 1.5. Having fixed the initial state condition, the state varies as a function of slip-velocity and of one of the unknown parameters, d_c (equation 4.4). Instead of formulating an inverse problem in terms of the friction parameters $A\sigma$, $B\sigma$, (a_l and b_l), and d_c , (as proposed by Reinen and Weeks, 1993) we solve for $A\sigma$, $B\sigma$, a_l , and b_l for trial values of d_c . We consider as possible solutions only those resulting in positive friction parameters. Although negative values of $B\sigma$ have been inferred to fit laboratory measurements of rock friction at hydrothermal conditions (Blanpied et al., 1995) the friction model applied to fit such data substantially differs from the one adopted in this study and, as the authors discuss, the fit obtained was poorly constrained by their available measurements.

4.3.3.1 Grid search over d_c

For each selected subfault we loop over trial values of d_c from 0.002 to 0.65 m, each of which result in different state histories. For each trial value of d_c and initial state θ_0 , we use equation 4.5 or equation 4.6 to fit the observed shear stress change histories by solving for the parameters $A\sigma$, $B\sigma$, a_l , and b_l .

We do not solve explicitly for the reference value of friction, μ_0 . The state history is calculated using equation (4.4), where the instantaneous values of slip-velocity are sequentially inserted into the equation and considered constant over each time step. We used a time step of 0.08 s.

The fitting to the full model is obtained through a Gauss-Newton method (non-linear least-squares), while for the simplified model a simple linear least-squares is applied for the estimation of the parameters $A\sigma$ and $B\sigma$. Regardless of the specific regression method applied, we follow the same procedure to select our best estimates of friction parameters.

For both cases, we calculate the sum of square residual (RSS) from each regression analysis corresponding to different trial values of d_c . For each subfault, the preferred estimate of d_c is the trial value that minimizes the residual sum of squares, and the best

estimates of friction parameters are those obtained from the regression analysis carried with this particular value of d_c .

Figure 4.4 shows an example of this procedure for a subfault with a fast-weakening behavior on the Nojima fault at 15 km depth and about 15 km along strike assuming the Dieterich model (5). Panel (a) depicts the RSS for each trial value of d_c , and the large dot corresponds to the minimum of RSS and the preferred value of d_c . The missing values for d_c larger than about 0.015 m correspond to prohibited solutions that require at least one of the frictional parameters to be negative. This feature is common to several subfaults showing a relatively fast-weakening behavior.

The flat part of RSS curve corresponds to d_c values that fit the data equally well, so the width of the flat part provides a range of critical slip distances consistent with Ide and Takeo's stress curves. In this case the range of d_c is 0.005 – 0.015 m. Panels (b) and (c) show plots of $A\sigma$ and $B\sigma$ as functions of d_c and the large dots mark the best estimates of these parameters that correspond to the preferred value of d_c . We do not show the variation of RSS with the cutoff parameters a_l and b_l because of their large associated errors, as discussed later. Note that $B\sigma$ and d_c are positively correlated, as these parameters have competing effects in controlling the evolution effect.

Figure 4.5 shows the fitting results for this subfault. Panel (a) depicts the slip-velocity given by the Ide and Takeo (1997) model. The dots correspond to the instantaneous slip-velocity at each time step and are the values of velocity used to calculate the state evolution (equation 4.4) depicted in panel (b) using the minimum-RSS estimate of d_c . Panel (c) and (d) show the shear stress change as a function of time and slip, respectively. The continuous lines are the stress functions calculated from the Ide and Takeo (1997) model and the dots correspond to the fitted values obtained using equation 4.5 and the best estimate of frictional parameters. Note that we only fit the values of stress change that correspond to non-zero slip-velocity.

Figure 4.6 shows an example of fitting procedure for a slow-weakening subfault assuming the Dieterich- Ruina model (equation 4.6). Notice essentially the same features discussed for the fast-weakening example, but in this case d_c values from about 0.03 m up to 0.65 m are consistent with the inferred stress history.

4.3.4 Caveats and Reliability of Stress Curves

The simple formulations of rate- and state-dependent friction as given in equation 4.1 and 4.2 are themselves an idealized description of fault friction behavior, and are not able to describe and explain more complicated mechanisms that might be important or even dominant during dynamic slip on natural faults.

In this study we ignore phenomena such as variations of normal stress and/or fluid pressure variations coupled to slip, and chemical effects in faults, such as hydrothermal deposition. Moreover, the constitutive parameters themselves might be slip dependent and therefore could evolve together along with structural and physical changes of fault surfaces undergoing slip (Beeler *et al.*, 1996; Tsutsumi and Shimamoto; 1997; Blanpied *et al.*, 1998).

Given these limitations, in this study we merely aim to address the applicability of simple RSV friction laws to the dynamic rupture of a real earthquake, while keeping in mind that more appropriate constitutive relations might be required in the future.

The reliability of our calculated stress curves is negatively affected by:

1) The nonuniqueness of the slip model and its associated stress change model derived from ground motion data. Because stress change is related to the spatial derivative of slip (Andrews, 1980), the inability of ground motion inversions to resolve the short-wavelength variations of slip on faults means that the short-wavelength variations of stress are unresolvable. This is particularly true at the crack tip, where spatial and temporal variations of stress and slip-velocity are expected to be greatest.

2) The further loss of spatial and temporal resolution caused by the necessary discretization of continuous functions, slip and stress, onto a space-time grid.

3) The lack of data that can be used to infer the characteristics of quasistatic sliding before the onset of dynamic rupture.

The first type of nonuniqueness is probably the most serious because it affects the reliability of both the slip-velocity and the derived stress. For example, Guatteri and Spudich (2000) found two rupture models characterized by different yield stresses and rates of slip-weakening that produced essentially indistinguishable seismograms in the frequency band (0 - 1.6 Hz) typically modeled in strong ground motion inversions. Furthermore, using band-limited waveform data to infer a slip model typically involves

a regularization in the form of a smoothing constraint. Thus, using such a constraint to derive the dynamic source description would bias both the slip-velocity and stress histories to be smooth, meaning that the peak values of both would likely be underestimated. However, it is important to mention here that the two models found by Guatteri and Spudich (2000) have very similar apparent fracture energy distributions over the fault plane. Factor 2) is also likely to yield an underestimated peak stress.

The lack of resolution of both quasistatic (pre-earthquake) and peak values of slip-velocity and shear stress limits our ability to infer the parameter controlling the direct velocity effect, $A\sigma$. If rate- and state-variable friction actually governs the Nojima fault, then when any point on the fault (outside the nucleation zone) makes the transition from quasi-static to dynamic slip, the slip-rate goes from about 10^{-12} m/s to 1 m/s in 0.1 s, and the stress might jump from 10 MPa to as much as 200 MPa in that same time interval. If we could resolve these values from inversion of ground motion data, then we could obtain an accurate value of $A\sigma$ (and a_f). However, at best Ide and Takeo's inversion can only resolve a jump in slip-rate from about 0.1 to 1.0 m/s, and their jump in stress almost certainly underestimates the true jump, so $A\sigma$ is essentially unresolvable. The stress behavior after the weakening process has occurred, i.e. when the state variable has reached a small steady state value, would provide useful information to constrain the direct effect; however, these small stress fluctuations are not well resolved with the 1995 Kobe earthquake strong motion data.

The evolution effect is controlled by both $B\sigma$ and ϑ (through d_c and slip-velocity, v), and in effect, yields a trade-off between $B\sigma$ and d_c . Moreover, we consider only slip-velocity values in the range 0.1-1 m/s which is a much smaller range than the 10^{-8} to 10^{-2} m/s observed by Okubo and Dieterich (1986). This limits our ability to resolve the cutoff parameter a_f .

4.4 Results

4.4.1 Full Model versus Simplified Model

The results of Okubo and Dieterich (1986) suggest that equation 4.5 with cutoff parameters to rate and state dependence is appropriate for modeling both quasi-static and dynamic sliding observations. However, even though their laboratory observations of sliding velocity span a wide range of values, the cutoff parameters a_i and b_i are still poorly constrained (see Table 1 in their paper).

In this study we consider only variations of slip-velocity resolvable using ground motion inversion (0.1-1.0 m/s), and therefore we cannot account for stress changes accompanying the large velocity jumps typical of the transition from quasi-static to dynamic slip. Our limited range of slip-rate observations greatly limits the resolution of the cutoff parameters. Furthermore, as equation 4.5 is nonlinear in a_i and b_i , the estimate of these parameters and of their standard errors can be quite unstable.

We found that the full model and the simplified model yield very similar parameter estimates and fitting results. Moreover, we found that very large statistical errors are associated with the cutoff parameters a_i and b_i so that these parameters are essentially unconstrained by our analysis. Following equation (4.5), we quantified the importance of these cutoff parameters by calculating two quantities, the ratio of a_i to the largest value of slip velocity and the product of b_i with the smallest value of ϑ . Because these quantities for most subfaults were much larger than 1, we concluded that our fits are not sensitive to the cutoffs of the rate and state dependencies.

Moreover, we determined that asymptotic parametric 95% confidence intervals for these quantities were nearly symmetric around the best estimate, spanning over five orders of magnitude. For a few cases we checked the reliability of the parametric-asymptotic error estimates through a bootstrap procedure which confirmed the large uncertainties associated with the cutoff parameters a_i and b_i . Given the linearity and simplicity of the Dieterich-Ruina equation (4.6) we therefore adopt this as the model for the observed stress histories.

4.4.2 Critical Slip

Figure 4.7 summarizes our estimates of d_c for the selected subfaults plotted as a function of depth. The errorbar associated with each estimate of d_c reflects the range of variation of d_c over which the respective RSS function is nearly flat at its minimum. The minimum RSS values are systematically below 0.06 m, with a few larger values that we will discuss later.

The trend in Figure 4.7 suggests that shallow fault regions down to about 5-8 km are characterized by larger d_c values than the deeper regions. However, this depth variation does not appear to be very significant and, as we will discuss later, because our estimates should be interpreted as upper bounds to the true d_c , we cannot assume that the same trend would characterize the true d_c variation.

We assign distinct symbols to differentiate the fast- versus the slow-weakening subfaults, and the tones of gray indicate the respective coefficient of determination, R^2 . R^2 quantifies the proportion of variability of stress change, τ , explained by regression on v and ϑ (Weisberg, 1985, p.19).

From the example shown in Figures 4.4 and 4.5 we notice that d_c values between 0.005 to 0.015 m can model the observed stress history. However, if we estimated the slip-weakening distance by visually analyzing the stress versus slip curve (Fig. 4.5), we would infer a d_c of about 0.15-0.25 m. This difference shows that these two critical displacements should not be interpreted as being the same constitutive parameter.

In the state-variable friction formulation d_c is the decay constant in the state evolution equation 4.4. Following an increase in slip-rate, according to equation 4.4 the state evolves toward a new value characteristic of the new sliding velocity, resulting in a weakening process over d_c . However, during dynamic rupture the variation of slip-velocity during the time in which the stress drops to its residual value is much more complex than in velocity stepping experiments. This slip-velocity variation extends the weakening process beyond the d_c that governs the decay over each single velocity change. This process of continuing evolution in adjusting to varying slip velocity results in the long apparent slip-weakening distance D_c as inferred from the stress as a function of slip.

Our inferred values of rate and state d_c for fast-weakening subfaults are about 10-20 times smaller than the D_c derived by Ide and Takeo from the stress versus slip curves. Our estimates are still several orders of magnitude larger than the laboratory-derived values, yet they narrow the large gap between experimental values and previously inferred values for rupture dynamics.

Sleep (1997) remarks on a similar difference between the two critical displacements in theoretical simulations of fault friction behavior assuming a unified rate- and state-dependent friction law. In his simulations he finds that the slip-weakening critical displacement D_c reaches values up to 50 times larger than the rate- and state critical slip.

4.4.1.1 Interpretation

How should we interpret our inferred values of d_c ? In order to answer this question we should consider the following factors:

1) The limited frequency band in the waveform data, and the smoothing constraints applied to the inversion procedure might bias the stress curves to be smooth (Gattereri and Spudich, 2000), causing the inferred rate of weakening to be slower than the true one. Hence, due to such bias, our estimates of d_c are probably upper bounds on the true d_c .

2) The numerical discretization imposes a limit in the maximum rate of weakening that we can resolve. For a more detailed explanation see the discussion in Andrews (1985).

3) The lack of a strong minimum in the RSS function for most subfaults suggests that larger values of d_c than the minimum-RSS estimates are consistent with the observations. For the “fast-weakening” subfaults (Fig. 4.4 and 4.5) the range of consistent d_c values is quite narrow, while for the “slow-weakening” subfaults (Figure 4.6) this range might span an order of magnitude. The few large values in the d_c estimates as shown in Figure 4.7 come from slow-weakening cases with a nearly flat RSS over a wide range of d_c values. Inspection of these cases reveals that causes of this unconstrained slope are either stress variations after most of the weakening has occurred or stress fluctuations during weakening.

In many cases, however, as can be seen in Figure 4.7 from the height of the errorbars, the width of the flat part of the RSS function is quite narrow. The difference between d_c and D_c underscores the fact that most slow-weakening subfaults having long D_c are equally consistent with a very small rate and state d_c as well as with large d_c .

Given the above resolution considerations, we believe that our fitted values of d_c provide a rough upper bound for this parameter. However, point 3) does not rule out the possibility that larger values of d_c might be acceptable for the slow-weakening subfaults. For the purpose of interpreting these results in terms of fault physical properties, we believe that it might be useful to consider the rate of weakening (slow- vs fast-weakening behavior in Figure 4.7) rather than the estimated d_c value. As already pointed out by Ide and Takeo (1997), a slow-weakening behavior might indicate local fault material properties that promote stability. With this in mind, Figure 4.7 suggests that material properties vary on the fault both with depth and along the strike direction, reflecting the important role of both lateral and vertical heterogeneities in the frictional properties of the fault in controlling earthquake rupture (Boatwright and Cocco, 1996). However, our results support the conclusion of Ide and Takeo (1997) that slow-weakening behavior characterizes shallow parts of the fault more consistently than deep regions.

4.4.3 $A\sigma$ and $B\sigma$

It is critical to recall that the nonuniqueness and poor resolving power of the ground motion inversion imply that we have no actual resolution of the values of $A\sigma$ and $B\sigma$. Our estimates of $A\sigma$ and $B\sigma$ would be correct only if Ide and Takeo's stress time series were perfectly resolved, which they are not. Nonetheless, we derive the minimum-RSS estimates of the friction parameters $A\sigma$ and $B\sigma$ and compare them with other estimates inferred from independent stress triggering studies. The $A\sigma$ consistent with Ide and Takeo's solution range between 0.01 to 0.75 MPa, while the $B\sigma$ consistent with Ide and Takeo's solution take values between 0.01 to 0.3 MPa with a few estimates between 1 and 3 MPa. The $A\sigma$ values consistent with Ide and Takeo's model are compatible with

the values proposed by Toda et al. (1998), Harris and Simpson (1998) and Belardinelli *et al.* (1999).

Toda et al. (1998) have proposed a value for $A\sigma = 0.035$ MPa based on changes in seismicity rate following the 1995 Kobe earthquake. Harris and Simpson (1998) have selected a range of values for $A\sigma$ of 0.0012 – 0.6 MPa based on changes in the seismicity rate in the San Francisco Bay Area after the 1906 earthquake. Belardinelli *et al.* (1999) obtained values of $A\sigma$ of 0.08 to 0.09 MPa from a study on fault interaction and earthquake triggering during the 1980 Irpinia earthquake. The distribution of these friction parameters with fault depth (not shown here) does not reveal any systematic and significant trend.

The trade-off between d_c and $B\sigma$ discussed above should also be considered here for a more complete interpretation of our results. This trade-off, together with the reliability issues discussed above, underscores the need for a parameter related to fault constitutive properties that does not suffer from such ambiguity.

4.4.4 Apparent Fracture Energy.

The state evolution causes a finite fracture energy, G_c , to be absorbed near the crack tip. The apparent fracture energy G_c is an important parameter in dynamic models and represents the energy per area required to initiate fully dynamic fault sliding and, in analogy with slip-weakening models (Ida, 1972; Palmer and Rice, 1973) can be estimated from the stress-slip curve as the area beneath the weakening part.

When the stress drop is fixed, the fracture energy controls the propagation of rupture along the fault, i.e. determines the rupture velocity (Andrews, 1976; Guatteri and Spudich, 2000). It follows that this parameter can be more stably estimated from ground motion data than the single friction parameters $A\sigma$, $B\sigma$, and d_c . Estimates of shear-fracture energy have been calculated for previous earthquakes (e.g. Ida, 1973; Husseini et al., 1975; Aki, 1979; Beroza and Spudich, 1988), yielding a range from $10^2 - 10^8$ Jm⁻².

Figure 4.8a shows our estimated values of G_c for both the original stress curves from Ide and Takeo (1997) model, and for the fitted values of stress assuming the Dieterich-

Ruina model. We emphasize that at each subfault, G_c is calculated using the respective value of D_c , not the rate and state slip -weakening distance d_c . The two calculations give very similar results, with a median value of $G_c \approx 1.5 \times 10^6 \text{ Jm}^{-2}$. This value is consistent with previous estimates for other earthquakes. Beroza and Spudich [1988] estimated G_c for the 1984 Morgan Hill earthquake to be about $2 \times 10^6 \text{ Jm}^{-2}$, and Rice compiled a range of $0.3 - 5 \times 10^6 \text{ Jm}^{-2}$ for average energy per area (personal communication).

Okubo and Dieterich (1984) estimated apparent fracture energy of stick-slip failures generated along simulated faults with different physical properties, such as normal stress and fault roughness. They point out that as the normal stress increases with depth, the apparent fracture energy should increase correspondingly, and that increasing fault roughness also increases G_c . Therefore, these two factors might have competing effects in controlling the variation of G_c .

From Figure 4.8b it appears that fault material and physical properties on the Nojima fault play a dominant role in determining the local apparent fracture energy G_c . For our limited set of subfaults, G_c values below the median are consistently associated with deep fault regions. This characteristic might be due to a combination of factors acting in the deep fault, such as lower stress drop associated with lower slip, shorter D_c possibly associated with lower fault roughness, and weaker fault rock. The previous observation is consistent with the idea that it is the combination of the friction parameters, rather than their individual values, that controls earthquake instability and the dynamics of rupture propagation.

4.1.1.1 Lower Bound for D_c

From our proposed values of G_c we can determine a rough estimate of the lower bound for D_c on the Nojima fault. We can assume that the upper bound for the peak stress is given by the local rock strength, and that the stress drops to zero. All these assumptions will result in the lowest possible D_c consistent with our estimated G_c .

Assuming a simple slip-weakening model, D_c can be determined using the following equation: $D_c = 2G_c/\tau^p$. To evaluate this expression, we use our estimated median value of G_c and an estimated upper bound for the value of rock strength τ^p at 10 km depth on

the Nojima fault, calculated assuming a static coefficient of friction $\mu_s = 0.7$ applicable to the intact host rock (granodiorite) [Lockner et al., 2000]. The estimated lower bound for D_c , D_c^{lower} , is then $D_c^{lower} \approx 0.016m$.

Moreover, for the sake of estimating the lowest possible lower bound of D_c , we assume that the stress does not drop until the fault slip has reached the slip-weakening distance D_c . Although this assumption is not consistent with any physical model of fault frictional behavior, it yields the lowest possible $D_c^{lower} \approx 0.008m$.

4.5 Conclusions

Previous estimates of the slip-weakening distance D_c , the slip distance over which the stress drops, suggested that this critical displacement can take values of the order of several cm to about 1 m on natural faults. These values are very large compared to laboratory estimates and have been interpreted to reflect topography and roughness typical of natural faults. However, D_c should not be confused with the critical slip, d_c , in the rate and state-variable friction formulation. For the fast-weakening parts of the fault we estimate a critical slip distance d_c of 0.01-0.05 m for the 1995 Kobe earthquake, 10-20 times smaller than D_c . Our estimates of d_c are subject to several resolution problems, and might be considered as upper bounds to this constitutive parameter.

Our data set is not sufficient to discriminate between the Dieterich-Ruina model and the original Dieterich formulation with cutoff parameters to the rate and state dependencies (Okubo and Dieterich, 1986). We found that the value of $A\sigma = 0.035$ MPa is consistent with both Ide and Takeo's model of the Kobe dynamic rupture and independent quasi-static studies of seismicity. However, owing to resolution problems and nonuniqueness of the ground motion inversion, we have essentially no resolution of $A\sigma$ and $B\sigma$.

The state evolution effect determines a finite fracture energy absorbed at the rupture front. This energy is an important parameter in rupture dynamics and can be more stably estimated from waveform data than the individual friction parameters. For the 1995 Kobe earthquake we found a median value of $G_c \approx 1.5 \times 10^6$ Jm⁻², consistent

with estimates for past earthquakes. A slight decrease of G_c below 8-10 km depth suggests that constitutive properties on the Nojima fault might favor seismic instability and rupture propagation below this depth. The estimated G_c for the Nojima fault and a plausible upper bound for the local rock strength provide us with a means to infer the lower bound for D_c of about 0.008 m .

The energy depth dependence contrasts with the lack of systematic depth variation of our estimated friction parameters. This suggests that lateral and vertical heterogeneities in the friction parameters may have competing effects in controlling rupture propagation, and that the single parameter G_c is more appropriate and reliable for describing the seismic source in terms of fault physical properties.

In the future the algorithm presented in this study (and that presented by Guatteri and Spudich, 2000) might be useful as part of an iterative sequence of forward simulations and waveform inversions, similar to that of Fukuyama and Mikumo (1993) or Ide and Takeo (1996), aimed at determination of constitutive parameters consistent with observed ground motions.

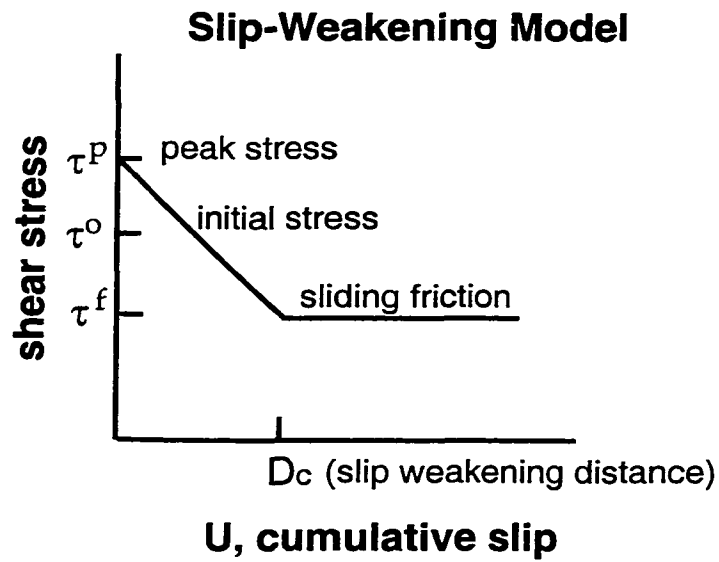


Figure 4.1. Idealized slip-weakening friction model (Ida, 1972; Palmer and Rice; 1973). The curve represents the total shear stress as a function of cumulative slip.

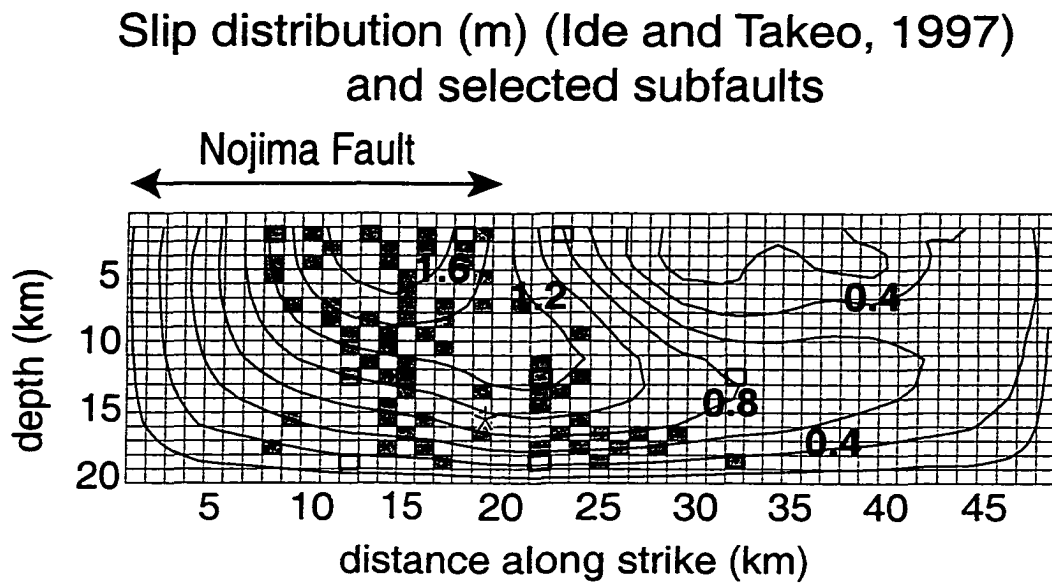


Figure 4.2. Total slip distribution from Ide and Takeo (1997) model. Each subfault is 1km wide. The subfaults with thick borders are those selected by Ide and Takeo (1997) for their analysis, while in this study we have used the subfaults filled in gray.

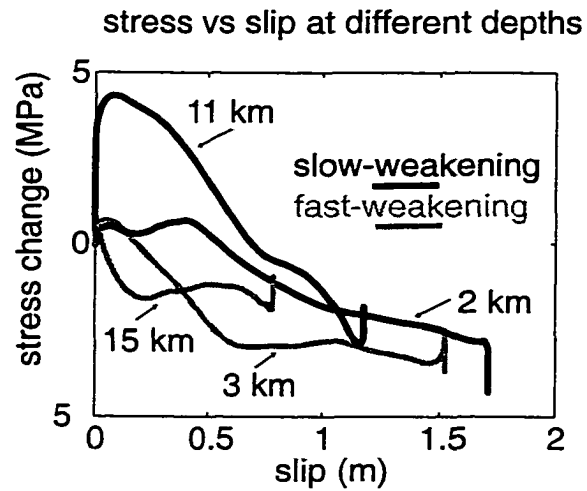


Figure 4.3. Examples of stress-slip curves representative of slow-weakening (black lines) and fast-weakening (gray lines) behavior. Next to each curve we report the depth of the respective subfault location.

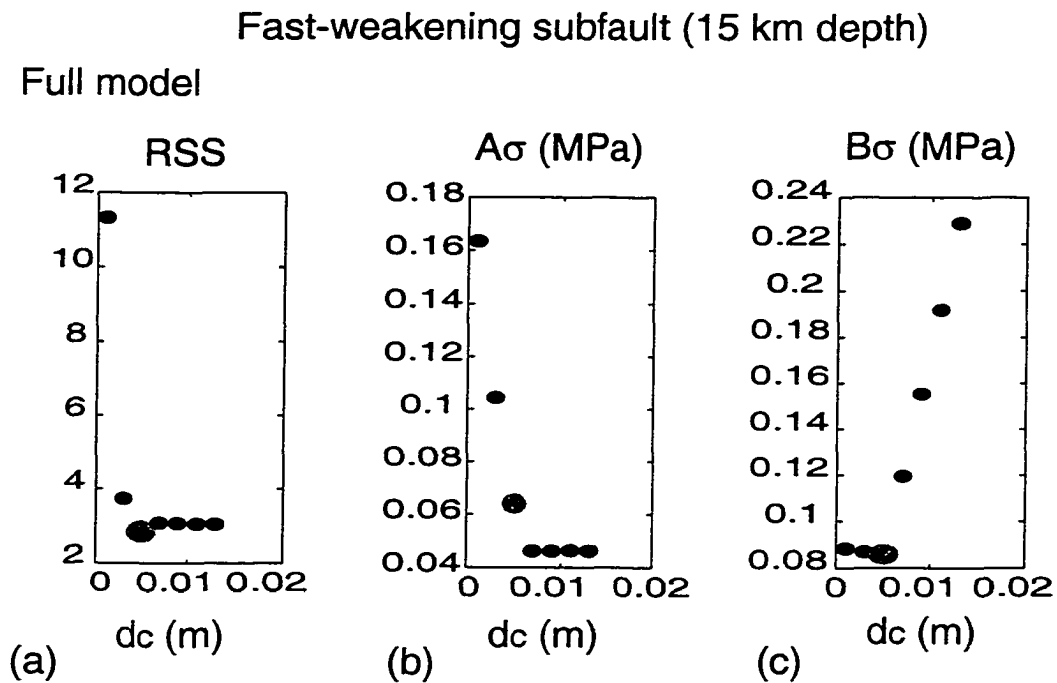


Figure 4.4. Procedure to select the best estimates of d_c and of friction parameters $A\sigma$ and $B\sigma$ (a) Residual Sum of Squares (RSS) obtained for each trial value of d_c . The gray large dot corresponds to the minimum of RSS and selects the preferred value of d_c . Friction parameters $A\sigma$ (b) and $B\sigma$ (c) obtained for each trial value of d_c . The large gray dots correspond to the preferred d_c value and the best estimate of friction parameters.

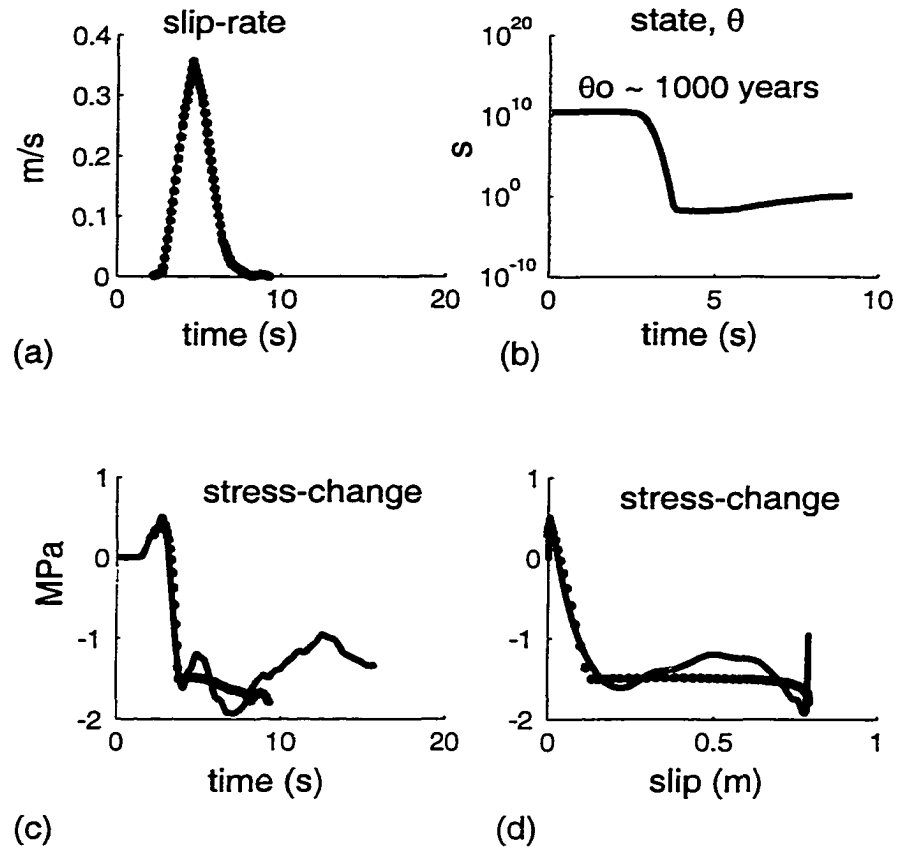


Figure 4.5. Fitting results assuming the Dieterich model (equation 4.5) for the same subfault as in Figure 4.4. (a) Slip-rate function as given by the dislocation model of Ide and Takeo (1997). The gray dots correspond to the slip-rate values for each time step (0.08s). (b) State variable history calculated using equation (4.4), the slip-velocity history and the d_c corresponding to the RSS minimum. Shear stress change as a function of time (c) and slip (d). The continuous line is the "observed" shear stress, and the dots are the fitted values obtained with the best estimates of friction parameters.

Slow-weakening subfault (11 km depth)
Simplified model (Dieterich-Ruina)

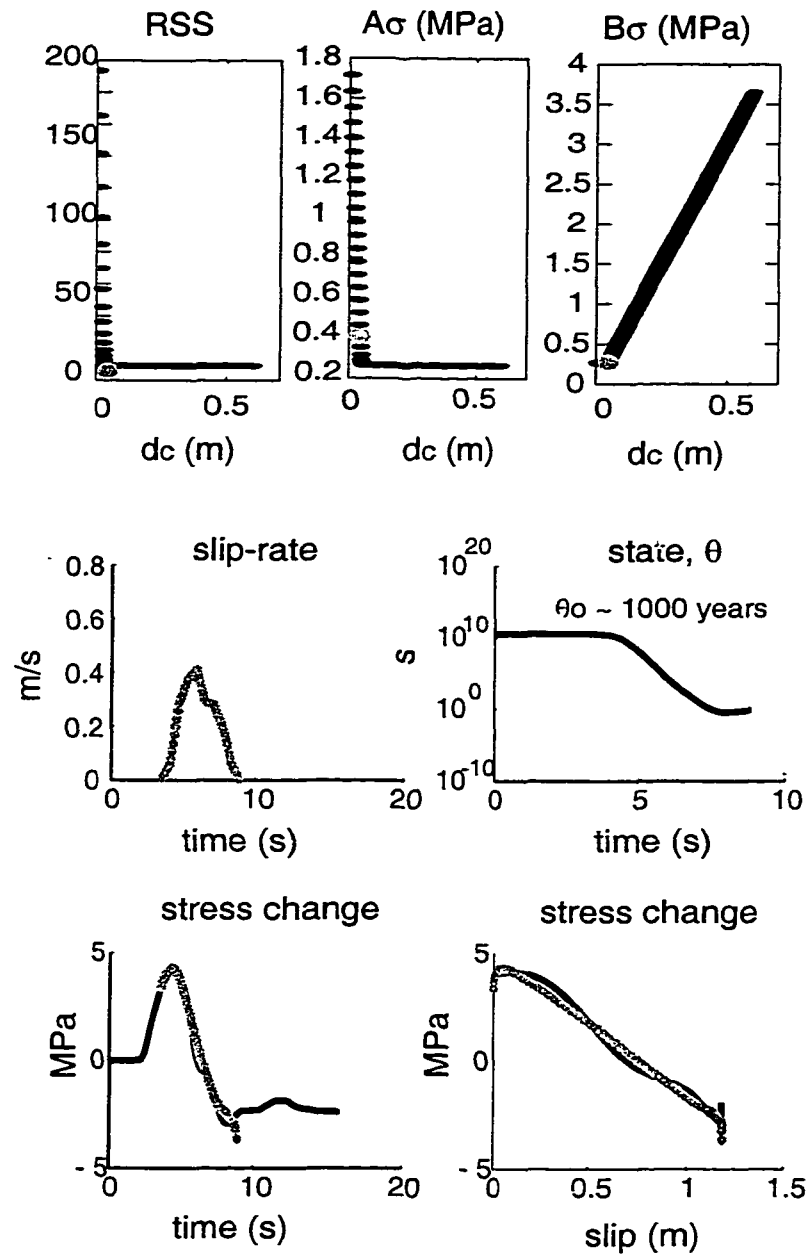


Figure 4.6. Procedure to select the best estimates of d_c and friction parameters $A\sigma$ and $B\sigma$ for a slow-weakening subfault, and the respective fitting results assuming the Dieterich-Ruina equation (6) (see captions of Figures 4.4 and 4.5 for details).

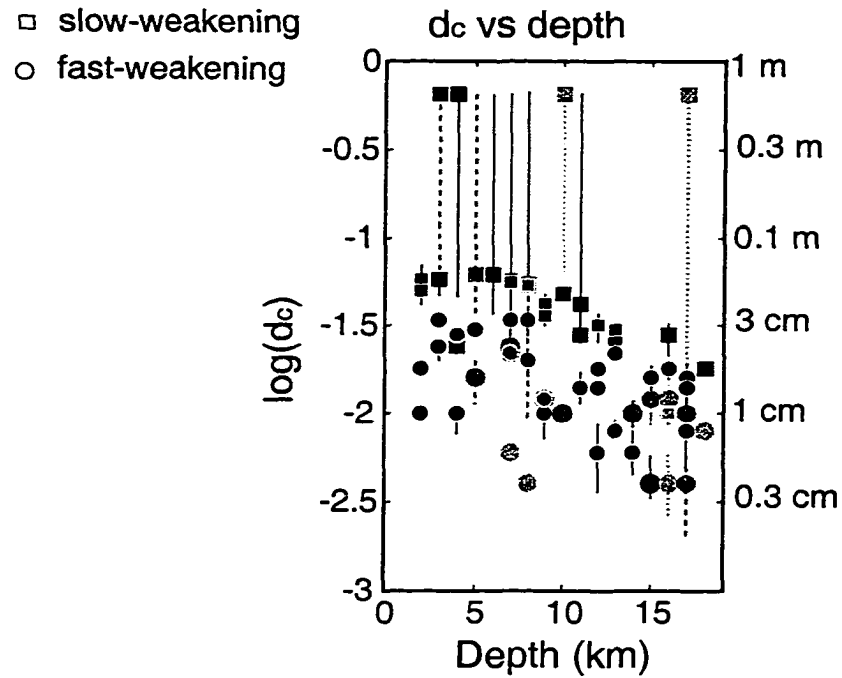


Figure 4.7. Estimates of d_c plotted as functions of depth. The squares show the d_c minimizing RSS for slow-weakening subfaults, while the circles are those for the fast-weakening subfaults. Light gray to black indicate poor to good fit to the observed stress ($R^2 < 70\%$, $70\% < R^2 < 85\%$, $85\% < R^2$, respectively, where R^2 is the coefficient of determination). The errorbars correspond to the range of d_c that span the flat part of RSS (see Figure 4.5).

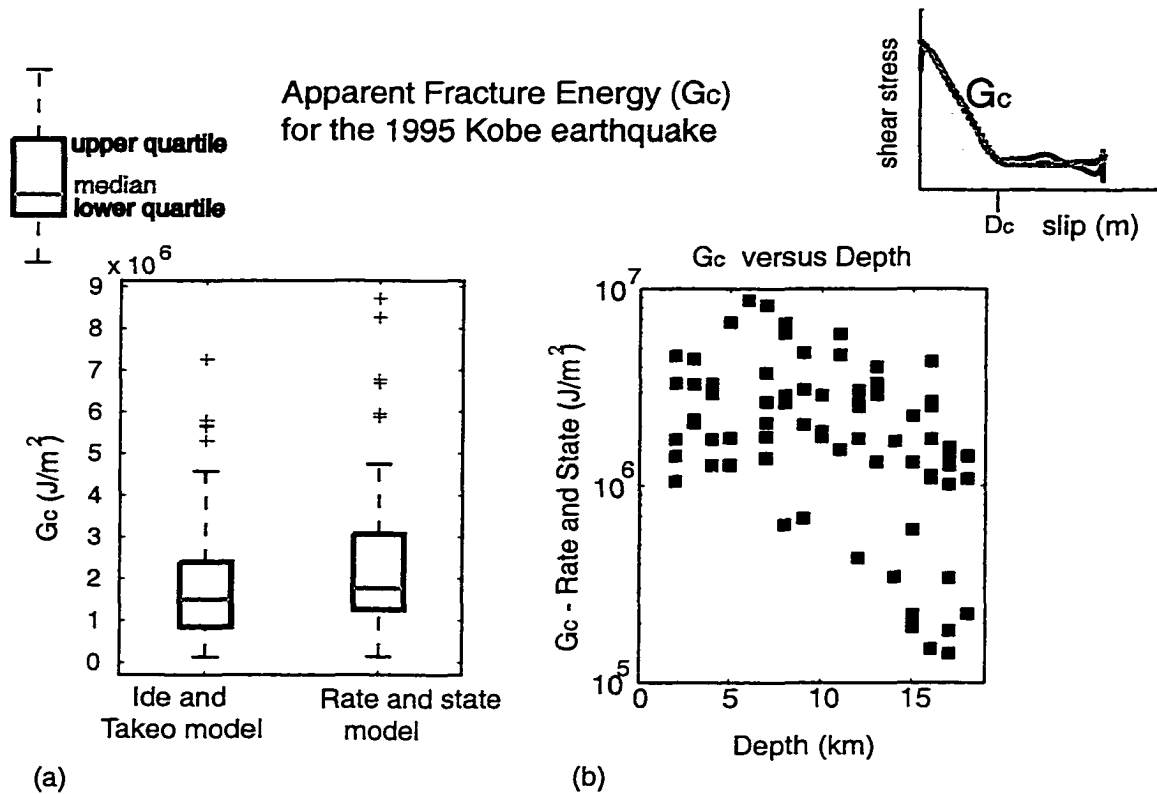


Figure 4.8. (a) Boxplots of G_c calculated from the “observed” stress-slip functions based on Ide and Takeo [1997] model, and from the fitted values assuming the Dieterich-Ruina equation (6). The median values for both cases are about. (b) Depth distribution of G_c calculated assuming the Dieterich-Ruina model.

Chapter 5 - The Effect of Absolute Stress on Rupture Dynamics: Modeling and Inference

Published in *Bull. Seism. Soc. Am.* (1998), **88**, 777-789. © Seismological Society of America

- 5.1 Introduction
- 5.2 Problem Statement
- 5.3 Results
- 5.4 Discussion
- 5.5 Appendix

Abstract

In this chapter I investigate the dynamics of rupture at low-stress level. I show that one main difference between the dynamics of high and low stress events is the amount of coseismic temporal rake rotation occurring at given points on the fault. Curved striations on exposed fault surfaces and earthquake dislocation models derived from ground motion inversion indicate that the slip direction can change with time at a point on the fault during dynamic rupture. I use a 3-D Boundary Integral method to model temporal rake variations during dynamic rupture propagation assuming a slip-weakening friction law and isotropic friction. The points at which the slip rotates most are characterized by an initial shear stress direction substantially deviating from the average stress direction over the fault plane. For a given value of stress drop the level of initial shear stress determines the amount of rotation in slip direction. I infer that seismic events that show evidence of temporal rake rotations are characterized by a low initial shear stress level with spatially variable direction on the fault (possibly due to changes in fault surface geometry) and an almost complete stress drop.

This study motivates a new interpretation of curved and crosscutting striations and puts new constraints on their analysis. The initial rake is in general collinear with the initial stress at the hypocentral zone, supporting the assumptions made in stress tensor inversion from first motion analysis. At other points on the fault, especially away from the hypocenter, the initial slip rake may not be collinear with the initial shear stress, contradicting the usual assumption of structural geology. On the other hand, the later part of slip in our models is systematically more aligned with the average stress direction than the early slip.

This work supports the use of low-stress observable phenomena, such as cross-cutting fault striations and strong spatial variations of slip direction, as a tool to infer the initial stress level (Spudich, 1992) before the earthquake initiated. In the Appendix I include results of such inference obtained from rake rotation data for the 1995 Kobe earthquake that indicate low absolute stress levels (less than 20 MPa) during faulting.

5.1 Introduction

It is widely believed that seismic radiation in earthquakes does not depend on the absolute stress level (Aki and Richards, 1980, p. 56). Recently, however, it has been shown that absolute stress levels influence rupture dynamics (Spudich, 1992; Andrews, 1994; Spudich et al., 1998), which in turn will affect seismic radiation. A common assumption made in dynamic modeling of spontaneous rupture was that earthquakes are high stress events (Das, 1981; Day, 1982). In particular, the initial shear stress, defined as the shear traction before the earthquake initiates, was usually set at a much higher value than the static stress drop. In this case the high initial stress levels are much larger than the time dependent stress perturbations (dynamic stresses) generated by the relatively low stress drop during rupture propagation and the slip direction is essentially parallel to the initial stress direction throughout the rupture. On the other hand, if the initial stress is low, then dynamic stresses are relatively large and may cause the direction of slip to vary with time (Spudich, 1992; Spudich et al., 1998). More recently (Harris et al., 1991; Harris and Day, 1993), 2-D spontaneous rupture propagation has been simulated on "weak" fault models (Brune, 1969) with low initial stress levels; in these 2-D simulations, however, the slip was constrained to one direction.

Temporal rake rotations are, in principle, a powerful tool for estimating the initial stress level. Spudich (1992) showed that if the rake rotates with time at a point on a fault during dynamic rupture, then it is possible to infer the absolute level of shear stress acting on that point before the earthquake initiated.

Geologic observations of fault striations show that temporal changes in slip direction at specific points on the fault at the earth's surface occur during an earthquake, for example, the 1992 Landers earthquake (which we personally observed), the 1957 Gobi-Altai earthquake (Florensov and Solonenko, 1965), the 1974 Izu-Hanto earthquake (Kakimi et al., 1977), and the 1969 Pariahuanca earthquakes (Philip, 1977). Curved and cross-cutting striations were also observed for the 1995 Kobe earthquake on exposures of

the Nojima fault on Awaji Island (Otsuki et al, 1997). The dislocation models derived from ground motion inversion for the 1995 Kobe earthquake are characterized by uniform rupture velocity, spatial slip heterogeneity and spatial and temporal rake rotations (Yoshida et al, 1996; Ide et al, 1996; Wald, 1996).

In this study we investigate the effect of absolute stress on temporal rake rotations in 3-D models of spontaneous rupture propagation. We present five different dynamic rupture simulations loosely guided by the slip distribution of the Kobe earthquake as inferred by Yoshida et al. (1996). We try to determine the factors that could lead to the rake rotations observed in their model. Our objective is not to model the Kobe earthquake specifically, but rather to show the separate influences of high or low initial stress, spatially uniform or nonuniform initial stress direction, and spatially uniform or nonuniform frictional properties, i.e. strength, stress drop, and slip-weakening distance, on the dynamics of rupture.

We find that temporal changes in slip direction are a sensitive indicator of the level of initial stress and that low initial shear stress, i.e. almost complete stress drop, with spatially nonuniform direction of initial stress maximizes the amount of rake rotation. In a more general and simpler interpretation, we could refer to a high fractional stress drop as one of the causes of temporal rake rotations rather than referring to two different parameters (initial stress and stress drop). However, given that high stress events (of the order of 100 MPa) are not likely to release the stress almost completely (the stress drop is usually estimated to be less than 10 MPa), in this study we will emphasize the importance of a low initial stress (of the order of 10 MPa) as one of the necessary (not sufficient) conditions for the occurrence of temporal rake rotations. In this way our results and conclusions are physically more informative and can give some insight in understanding the importance of absolute stress levels on rupture dynamics and seismic radiation.

Our modeling indicates that the interpretation of curved and crosscutting striations requires the consideration of the dynamic stresses caused by rupture. We find that where the dynamic stresses are large, i.e. at points away from the hypocenter, the initial slip direction can be different from the initial shear stress direction. This implies that a common assumption in structural geology, that the direction of initial shear stress is collinear with the slip direction (e.g. Etchecopar et al., 1981; Angelier et al., 1982; Angelier, 1984), could be incorrect. The analysis of curved striations may yield important information on the faulting process. We find that rake rotations are diagnostic of a heterogeneous initial stress direction. We also find that the average direction of initial stress is still consistent with the average rake and that, at a given point on the fault, the slip direction in the later stages of rupture is better aligned with the average initial stress direction over the fault plane.

In simple models with uniform slip weakening distance over the fault plane we also find that the distance over which the initial slip direction is maintained may provide an upper bound of the slip weakening distance. However, exceptions to this correlation exist. In fact, we show that for a model having a non uniform slip weakening distance and an initial stress direction strongly varying on the fault, at some points of the fault the slip direction may start rotating before the slip weakening distance is exceeded. We comment here that this specific analysis leads to conclusions based on qualitative considerations rather than on a quantitative procedure. In fact we only visually estimated the linear part of slip, since we have not yet formulated a suitable mathematical approach to quantify this parameter.

An additional purpose of this Chapter is to show what the observed temporal rake rotations imply about the preseismic state of stress on the Nojima and Rokko fault systems during the 1995 Kobe earthquake. We calculated dynamic stress changes on the rupture fault surface from Yoshida et al. (1996) slip model and applied Spudich's (1992) method to infer that the stress level on the Nojima fault immediately before the

earthquake was low (7 to 17 MPa), with coseismic fractional stress drop being complete near to the surface and being about 32% at depth in the crust. We summarize the methodology and results in the Appendix.

5.2 Problem Statement

We follow the formulation given by Das (1981), Andrews (1985), Das and Kostrov (1987) and Spudich (1992) for discretized models. In a homogeneous, isotropic, linearly elastic, unbounded medium a plane shear crack lies in the plane $x_3 = 0$ in a Cartesian coordinate system (x_1, x_2, x_3) (see Das and Kostrov, 1987, Fig. 1). In the following x_{ij} is the location of grid points on the crack plane, t_k is the time of k -th time step, $u_{\alpha ij}$ is the α -component of displacement of the crack face at location ij and time t_k , $\sigma_{\alpha ij}^o$ is the α -component of initial shear stress across the crack plane, and $\tau_{\alpha ij}$ is the α -component of the stress change (dynamic stress drop) at location ij and time t_k caused by motions on the fault. The motion of the crack face at time t_k is determined from stresses on the fault at previous times by:

$$L_{\alpha ij} := \sum_{\beta=1} \sum_{k=0} \sum_{i',j' \in P_k} \tau_{\beta i' j'} \times F_{\alpha\beta}(i-i', j-j', k-k') \quad (5.1)$$

where $F_{\alpha\beta}$ is the α -component of displacement at ijk caused by the β -component of stress change at $i' j' k'$ (Green's function), P_k is the union of all grids at time k' lying within the cone of causality with vertex at ijk . Andrews (1985) calls the dynamic quantity expressed through equation 5.1 the "load", the contribution to slip caused at time step k by stress changes at *previous* time steps. The load is partitioned into slip and stress change as:

$$u_{\alpha ij} + \Delta t G_o \tau_{\alpha ij} = L_{\alpha ij} \quad (5.2)$$

where Δt is the time step $t_{k+1} - t_k$ and $\Delta t G_o$ is the compliance of the medium (Andrews, 1985). The total traction on the fault is the frictional traction

$$\underline{\phi}_{ijk} = \underline{\sigma}_{ij}^o + \underline{\tau}_{ijk}. \quad (5.3)$$

We define displacement- equivalent tractions

$$\begin{aligned} \underline{\Phi} &:= \Delta t G_o \underline{\phi}, \\ \underline{\Sigma}^o &:= \Delta t G_o \underline{\sigma}^o, \\ \underline{T} &:= \Delta t G_o \underline{\tau}. \end{aligned} \quad (5.4)$$

Then, equations 5. 2 and 5.3 become:

$$\underline{u}_{ijk} + \underline{T}_{ijk} = \underline{L}_{ijk} \quad (5.5)$$

and

$$\underline{\Phi}_{ijk} = \underline{\Sigma}_{ij}^o + \underline{T}_{ijk} \quad (5.6)$$

(Fig5.1a).

We assume isotropic friction; at any instant the slip velocity of a point on a fault is in the direction of the total traction. If the load is collinear with $\underline{\Sigma}^o$ for all time steps, then all other vectors are collinear with $\underline{\Sigma}^o$ for all time steps; if the load vector \underline{L} is not collinear with $\underline{\Sigma}^o$, then displacements are rotated away from the initial stress direction $\underline{\Sigma}^o$ (Fig. 5.1a). Equation 5.3 is fundamental for understanding the effect of a low initial stress on the amount of temporal rake rotation during dynamic rupture. At each point on

the fault and at each time step, the stress change vector $\underline{\tau}$ caused by motion on the fault is added to the initial shear stress vector $\underline{\sigma}^o$ to give the frictional traction vector $\underline{\phi}$. The direction of slip velocity is collinear with the direction of the frictional traction (assuming isotropic friction); the dynamic stress change, when it is relatively large compared to the initial stress, can cause a total traction vector deviating from the initial stress direction. Figure 5.1b and Figure 5.1c show the geometric relation of equation 5.3 for a case of high and low initial stress, respectively. At a given point on the fault, a high initial shear stress leads to a total traction direction fairly constant with time (collinear with the initial stress) while, for a low initial stress case, the total traction direction is very sensitive to the dynamic stress change effect, and it can rotate with time.

We simulate dynamic rupture propagation using the 3-D boundary integral spontaneous rupture code (Quin and Das, 1989; Boatwright and Quin, 1986) modified to include a slip-weakening friction law (Fig. 5.2) (Ida, 1972; Day, 1982; Andrews, 1985) in which the independent variable is the cumulative slip U_k integrated along the slip path, in order to allow temporal rake rotation. The input model is specified by assigning at each grid point the initial stress $\underline{\sigma}^o$, the strength parameter $S = \sigma^y - \sigma^o / \sigma^o - \sigma^f$, the stress drop $\sigma^o - \sigma^f$ and the slip-weakening distance D_c . From these we can obtain the fractional stress drop $\frac{\sigma^o - \sigma^f}{\sigma^o}$. We induced the nucleation by forcing the rupture at a minimum rupture velocity equal to 0.75 the shear wave velocity in the focal region, until it goes spontaneously. The size of the focal region is estimated through the approximate derivation for the critical crack radius r_c given by Day (1982, equation 10). The grid size is set to be 1.5 km in both strike (x_1) and dip (x_2) directions and one time step corresponds to 0.125 s. The minimum slip-weakening distance that can be resolved in a given model is determined by stability and uniqueness requirements. In order to check the

validity of our conclusion and their dependence on the resolution, we have redone the calculations using a finer grid interval (0.75 km) and a shorter time step (0.0625 s). The results shown in this study for the coarser grid (1.5 km) are resolution-independent. In the corresponding fine-grid models the number of time steps and subfaults required to simulate the total duration of rupture over the fault plane is quadrupled. We show the coarse-grid models because the simulation of the total duration of rupture on the fault plane using the finer grid interval would include the effect of radiation coming from the edge of the grid. This is due to the limited size of the grid (64x64) in the original Quin and Das (1989) code.

Because rake can rotate with time, we must solve a set of vector equations to determine the slip increment at each time step consistent with our slip weakening law. At a point on the fault the incremental slip $\underline{\Delta u}_{k+1} = \underline{u}_{k+1} - \underline{u}_k$ relative to time step $k+1$ is determined by finding the intersection between the unloading curve

$$|\underline{\Phi}_{k+1}| = |\underline{R} - \underline{\Delta u}_{k+1}|, \quad (5.7)$$

where \underline{R} is defined as $\underline{R} := \underline{\Sigma}^o + \underline{L}_{k+1} - \underline{u}_k$, and a straight segment of the piecewise-linear slip-weakening curve

$$|\underline{\Phi}_{k+1}| = \mathcal{S}^i + (U_k + |\underline{\Delta u}_{k+1}|)\mathcal{S}^i \quad (5.8)$$

where \mathcal{S}^i is the intercept and \mathcal{S}^i is the slope of the i -th segment. Note that the unloading curve $|\underline{\Phi}_{k+1}|$ is a hyperbolic function of $|\underline{\Delta u}_{k+1}|$ when rake rotation is allowed. From equation 5.7 and equation 5.8 we obtain

$$|\underline{R}|^2 - 2\underline{R} \cdot \underline{\Delta u}_{k+1} + |\underline{\Delta u}_{k+1}|^2 = [G_k + |\underline{\Delta u}_{k+1}|S]^2 \quad (5.9)$$

where we define $G_k := S^i + U_k S$. If we define $\underline{Q} := \frac{1}{2}(\underline{\Phi}_k + \underline{R})$, then $\underline{R} \cdot \underline{\Delta u}_{k+1} = \underline{R} \cdot \underline{Q} |\underline{\Delta u}_{k+1}| / (|\underline{R}| |\underline{Q}|)$. These are the vector equations that must be solved to determine the amount of slip when rake can rotate. The amplitude of incremental slip $|\underline{\Delta u}_{k+1}|$ is the smaller real solution of equation 5.9. We force the slip to stop when equation 5.9 does not have a real solution, or when the boundary condition of collinearity between total traction and slip velocity cannot be satisfied. For a similar problem where rake is not constrained a priori, Archuleta and Day (1980) formulated a stopping criterion equivalent to the physical requirement that slip at a given point on the fault stops when the magnitude of the frictional force vector exceeds the magnitude of the sum of the force vectors due to the instantaneous stress and to inertia acting on that point. However, they did not include a slip-weakening friction law, so their formulation is substantially different from ours. Our healing criterion is somewhat ad hoc, but it does not affect the results of this study significantly. We approximated the free-surface reflection effects implementing the image source method of Quin (1990) with improvements. The ideal case for applying the image source method is a vertical strike-slip fault, in which most of the reflection waves are from SH radiation. We tested this approximation comparing our results with those of Archuleta and Frazier (1978, Fig. 6); our method simulates the free surface effects quite accurately in a vertical strike-slip fault setting.

5.3 Results

In this section we present the results obtained for five different dynamic rupture simulations on a fault plane 22.5 km long and 15 km wide; we simulate a free-surface oriented perpendicular to the fault plane at downdip distance of 3 km in Figure 5.3. For simplicity we assume a homogeneous medium. The rupture is stopped artificially by setting a high value of strength outside the fault plane. As we will show later, this

artificial stopping does not affect substantially the rake rotation at points far from the boundary. The geometry and dimensions of the model is based loosely on the Kobe earthquake. Table 5.1 summarizes the input dynamic parameters and rake rotation results for each model.

5.3.1 Model 1

Figure 5.3 shows the dislocation solution for a spontaneous rupture model characterized by a low initial stress with a varying stress direction and spatially uniform frictional properties. The input dynamic parameters for the model in Figure 5.3 are initial shear stress = 7 MPa, stress drop = 5 MPa, strength parameter $S = 0.7$, slip-weakening distance = 0.37 m, fractional stress drop = 0.7 and $r_c = 3$ km. The direction of initial stress, shown by thick gray vectors in Figure 5.3, varies randomly on the fault plane with a correlation distance of about 6 km, similar to the variation of the initial slip direction for the 1995, Kobe earthquake (Yoshida *et al*, 1996; Ide *et al*, 1996; Wald, 1996). Note that spatial variations of rake rotations in our model (Figure 5.3) are less than those in dislocation models of the Kobe earthquake. The initial conditions of spatial heterogeneity of the initial shear stress direction and low initial shear stress amplitude lead to dynamic stresses that cause substantial temporal rake rotations at given points of the fault.

We can examine the physical cause of rake rotation using subfault 100 (at 14.25 km along strike direction and at 12 km depth) as an example. In Figure 5.4 we show: (a) the total traction amplitude versus the cumulative slip, (b) the total traction as a function of time, (c) the slip path and (d) the load path. We indicate the time step when the slip deviates from the initial direction of stress (time step 29); in each panel of Figure 5.4 the star indicates the respective quantity at time step 29. At this time, in this subfault the load vector \underline{L} is no longer collinear with $\underline{\sigma}^o$ (Fig. 5.4d); \underline{L} has a relatively large component perpendicular to the initial direction of stress. This perpendicular component

TABLE 5.1 - Input Dynamic Parameters and Rake Rotation Results

| | <i>Model 1 (Fig. 5.3)</i> | <i>Model 2 (Fig. 5.6)</i> | <i>Model 3 (Fig. 5.7)</i> | <i>Model 4 (Fig. 5.8)</i> | <i>Model 5 (Fig. 5.9)</i> |
|---|--|--|--|--|---|
| σ^o | 7 MPa | 7 MPa | 7 MPa | 7 MPa | 60 MPa |
| <i>Initial stress direction</i> | Spatially variable; correlation distance ~ 6km | Highly spatially variable; correlation distance ~ 3 km | Uniform | Uniform | Spatially variable; correlation distance ~ 6km |
| $\sigma^o - \sigma^f$ | Uniform 5 MPa | Uniform 5 MPa | Uniform 5 MPa | Uniform 5 MPa | Uniform 5 MPa |
| $S = \frac{\sigma^y - \sigma^o}{\sigma^o - \sigma^f}$ | Uniform 0.7 MPa | Uniform 0.7 MPa | Uniform 0.7 MPa | Variable (Fig. 5.8a) | Uniform 0.7 MPa |
| D_c | Uniform 0.37 m | Uniform 0.37 m | Uniform 0.37 m | Uniform 0.37 m | Uniform 0.37 m |
| <i>Rake rotations?</i> | Temporal and spatial rake variations | Substantial temporal and spatial rake variations | Temporal rake rotations at a few subfaults; no spatial rake variations | Temporal rake rotations at a few subfaults; no spatial rake variations | No temporal rake rotations; spatial rake variations |

drives the deviation of slip from the initial stress direction. Waves radiated from other parts of the fault cause the variation in the load direction. From equation 5.2 we can determine what subfaults in the cone of causality with vertex at subfault 100 and time step 29 have radiated the waves that consistently perturb the initial direction of the load vector at subfault 100. In equation 5.2 we choose ijk relative to subfault 100 and time step 29; we have previously calculated the traction changes $\tau_{\beta i' j' k'}$ for each subfault (i', j') and time step k' and we know the Green's functions $F_{\alpha\beta}(i-i', j-j', k-k')$, so we can calculate the contribution of each point (i', j', k') to the component of the load vector perpendicular to the initial direction of stress at (i, j, k) . We determined which subfaults (i', j') contributed most to the change in load between time steps 28 and 29. These subfaults are shown in Figure 5.5 in bold characters. They contributed P and S

waves from the rupture front. Most of these subfaults lay along P and S isochrones (relative to time step 29) formed by summing rupture time and P or S travel time to subfault 100 (Fig. 5.5). The stress perturbations traveling from these points are large since they represent the stress changes associated with the initial stress release. Note that the fault boundaries do not contribute much to rake rotation, as well as stress waves radiated at the stopping of slip at interior points of the fault. The direction of the initial stress at these subfaults affects the polarization of waves that perturb the total stress direction at subfault 100 at time step 29. Because the average initial stress direction of subfaults along these and later isochrones is more strike-slip than the initial stress direction of subfault 100, the rake at subfault 100 rotates toward strike-slip. Spatial variability in the initial stress direction makes the load direction vary in time at interior points of the fault. The dynamic stresses are not parallel to the initial stress, and since their amplitude is comparable with the initial stress level, the total traction can deviate consistently from the initial stress direction (Fig. 5.1c).

It is important to notice that the amount of rotation with time is influenced by directivity; the directivity effect causes evident rake rotations in the part of the fault where the rupture has propagated farthest (on the right side of the hypocenter). In dynamic modeling when there is rupture towards a point, the load jump is abrupt and this constitutes directivity. The rotation direction is strongly influenced by the average initial stress orientation in the ruptured part of the fault, which is right-lateral. At the points that show substantial temporal rake rotations, the slip direction rotates toward this average direction of initial stress. Moreover, since in dynamic rupture propagation the dynamic stress grows with the rupture area, for points that rupture late the load is large when slip initiates and the initial slip can deviate from the initial stress.

5.3.2 Model 2

Since the spatial variation of the initial stress direction plays an important role in causing temporal rake rotations during dynamic rupture, we investigated its effects further by modeling a spontaneous rupture at low stress with an initial shear stress direction varying randomly over a distance of about 3 km (highly varying initial stress direction) and uniform frictional properties. In Figure 5.6 we show the dislocation result and the initial shear stress distribution for this model. The input dynamic parameters are the same before, stress drop = 5 MPa, initial shear stress = 7 MPa, strength parameter = 0.7, slip-weakening distance = 0.37 m, fractional stress drop = 0.7 and $r_c = 3$ km.

The dislocation solution confirms the important role played by heterogeneous stress, in particular the spatial gradient of the initial stress direction, in determining where and when the rake rotations occur. The slip direction rotates with time at more subfaults and this happens earlier compared to the solution of model in Figure 5. 3. The initial motion is not collinear with the initial stress direction at subfaults having an initial stress direction different from that at neighboring subfaults. The deviation between the initial slip direction and the initial stress direction is more evident at points away from the hypocenter, where the dynamic loads are larger.

5.3.3 Model 3

We also modeled a spontaneous rupture at low initial shear stress with uniform stress direction and frictional properties to evaluate the degree of temporal rake rotation that can occur during dynamic rupture in a completely homogeneous model with low stress. Figure 5.7 shows the dislocation and initial shear stress vector at each subfault for this model, which has the following input properties: initial stress = 7 MPa, stress drop = 5 MPa, strength parameter = 0.7, slip-weakening distance = 0.37 m, fractional stress drop = 0.7 and $r_c = 3$ km. We notice that rake rotates with time at a few subfaults, especially close to the fault boundaries, due to the stopping of the rupture. In general, we observe

that the uniformity of slip direction is controlled by the uniform direction of initial stress. Even though the dynamic stress changes are comparable to the initial stress, the homogeneity in the initial stress direction does not introduce strong temporal and/or spatial heterogeneity in the direction of the load vector. Thus, we conclude that a low value of initial stress by itself is not sufficient to cause substantial temporal rake rotations in the slip solution (Fig. 5.7).

5.3.4 Model 4

We also introduced heterogeneity in the distribution of strength (Fig. 5.8a) into a low stress, uniform initial stress direction model. This did not lead to any substantial increase in the amount of temporal rake rotations. Isolated patches of high values of strength cause strong variations in rupture velocity and some additional rotation in the slip direction (Fig. 5.8b), but much less than those caused by spatial nonuniformity in the initial stress direction (Fig. 5.3).

5.3.5 Model 5

The final model (Fig. 5.9) represents a high stress event with non uniform spatial distribution of initial stress direction and uniform frictional properties (initial stress = 60 MPa; stress drop = 5 MPa; strength parameter = 0.7 and slip-weakening distance = 0.37 m). The lack of rake rotation in this model demonstrates that marked temporal rake rotation is a low stress phenomenon. In this example, the heterogeneity in the initial stress direction is not sufficient to cause substantial temporal rotation of slip direction because the dynamic stresses are too small compared to the initial stress level, and the initial direction of stress controls the direction of motion at each point of the fault and at each time step (Fig. 5.1b).

5.4 Discussion

We conclude from our modeling that two factors are necessary and sufficient to cause temporal rake rotations: a low initial stress level that can lead to an almost complete stress drop, and spatial variations in the direction of initial stress. A few previous studies have touched on the influence of the initial stress level on rake rotations. Das (1981) and Day (1982) recognized the relation between absolute stress levels and rotation of rake. Their analysis, though, was for high stress levels (fractional stress drop of 0.1 and 0.2, respectively) which minimize the amount of rotations. Mixed-mode dynamic simulations of Andrews (1994) indicated that the azimuth of the slip velocity vector varies between the onset of slip and the arrival of the Rayleigh front for trans-Rayleigh rupture speeds. He also showed that the amount of rake rotation depends on the value of the initial stress.

The two factors that lead to rake rotation may be linked. That is, heterogeneous initial stress direction on a fault plane might be expected for low stress events. Low initial shear stress could result from nearly fault normal compression. In this case small variations of fault orientation can lead to large variations in the direction of initial stress. This particular initial condition might be the main cause for spatial rake variations observed for example in the 1989 Loma Prieta earthquake (Beroza, 1991; Wald *et al.*, 1991; Árnadóttir and Segall, 1994; Guatteri and Cocco, 1996; Kilb *et al.*, 1997) and the 1995 Kobe earthquake. There is independent evidence for fault normal compression following the Loma Prieta mainshock in the heterogeneity of the aftershock focal mechanisms (Beroza and Zoback, 1993; Zoback and Beroza, 1993). Following the approach of Árnadóttir and Segall (1994, equation 8 through 12), we can quantify the change in the fault dip angle that would result in a change of about 30° in the initial shear stress direction on the fault plane (the maximum variation assumed for the heterogeneous models in Figure 5.3 and Figure 5.6 is 40°). Working with the geometric parameters for

the Kobe earthquake (strike-slip environment and dip angle of 85°) and assuming a uniform stress tensor, we can obtain a change in the rake of initial shear stress from 140° to 170° if the fault dip angle varies about 4° (dip $\approx 89^\circ$).

In our modeling results there is a tendency for the length of the straight part of slip to be equal to or larger than the slip-weakening distance (in the limit of our numerical resolution). Thus, field observations of the length of the initial straight part of striations could help constrain a critical parameter of the friction law, the slip-weakening distance. In fact, after the stress has dropped to the sliding friction (almost complete stress drop in our models), i.e. when the slip-weakening distance is exceeded, the slip direction is controlled completely by the dynamic stress changes and becomes very vulnerable to the driving force perpendicular to the direction of initial stress. To further investigate this result with better resolution, we modeled part of the rupture using a finer grid (0.75 km). Assuming a uniform slip-weakening distance on the fault plane (we modeled the rupture with slip-weakening distance ranging from about 0.25 to 0.8 m), we still obtain a good correlation between upper bound of the slip-weakening distance and initial linear slip length. We introduced a non uniform slip-weakening distance in a model with low initial stress and initial stress direction strongly varying over the fault plane (Fig. 5.10). We do not know if it is reasonable for the slip weakening distance to vary at this scale at the same depth (although Ide and Takeo, 1997 found that the slip weakening distance varies with depth from values of about 1 m in the shallow fault zone to about 0.5 m or less at depth). We present these results in order to investigate the general effects of a non uniform distribution of slip weakening distance on the length of the straight part of slip. In this case the general correlation observed still holds, but there are a few cases where the slip-weakening distance is larger than the initial linear slip length (Fig. 5.10). This happens at subfaults with long slip-weakening distance away from the hypocenter where the initial stress direction is very different from that at neighboring subfaults. In this situation the loads are large, and strong heterogeneity in the initial stress direction

distribution can cause temporal rake rotations at stress levels larger than the sliding friction. Moreover, regions having a long slip-weakening distance tend to rupture late, increasing the likelihood that perturbing waves will arrive before slip-weakening is completed. Qualitatively, this means that the amount of fractional stress drop necessary to observe substantial temporal rake rotations depends on the degree of spatial variability of initial shear stress direction and slip-weakening distance.

As already discussed, other important factors determine the length of the straight slip part. We have seen in the previous section, that the slip direction at a given subfault starts rotating when stress waves arrive from other subfaults that yield a component of load perpendicular to the initial direction of stress. If the direction of initial stress is fairly uniform over a relatively large zone, the perturbing stress waves arrive later compared to a case in which the direction of initial stress is very heterogeneous within a small zone. For the same reason, the rupture velocity (controlled mainly by the strength parameter) can influence the length of the straight slip part; for a given spatial distribution of initial stress, fast rupture shortens the straight slip part. At points having an initial stress direction that deviates significantly from the overall initial stress direction, the initial slip rake differs from both the local and the overall initial stress directions, and the slip rake tends to lie between the two directions. We found that a high rupture velocity can enhance the occurrence of the same phenomenon. Thus, the common assumption adopted in stress tensor inversions from analysis of striations, that the initial direction of slip is collinear with the direction of initial stress, should be carefully applied for cases of low stress events (if evident) and large variations in fault geometry. In estimating the average direction of initial shear stress from the analysis of curved striations, more weight should be given to the late part of slip direction; as discussed for model in Figure 5.3, at points where substantial temporal rake rotations occur, the slip rotates to align with the average direction of the initial stress in the ruptured part of the fault.

A more complete analysis of temporal rake rotations at shallow depths (as for curved striations observed at the earth's surface) should also consider the free surface reflection effects. Since we only used an approximation of these effects in our modeling, we cannot exactly quantify and completely analyze these effects. Nevertheless, we expect that the closer the top of the fault plane is to the free surface, the bigger the rake rotation is in the shallow fault zone.

A more detailed analysis of the effect of fault geometry changes on the dynamics of rupture should include the resulting variations in normal stress and the spatial heterogeneity not only in the initial shear stress direction distribution, but also correlated variations in the initial shear stress amplitude distribution. These additional heterogeneity would lead to spatial variation of stress drop and strength parameter, resulting in complex dynamic rupture (Day, 1982). In general we can conclude that the dynamics of low stress events are more sensitive to fault plane geometry variations than high stress events.

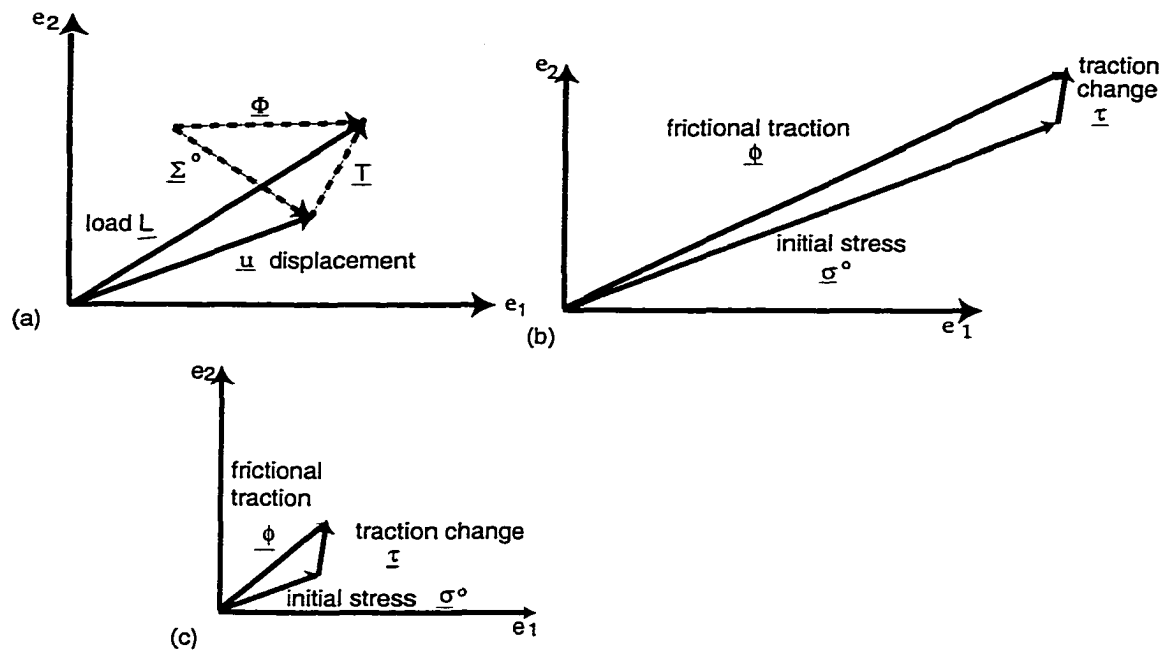


Figure 5.1: (a) Relation between displacement-equivalent friction $\underline{\Phi}$, displacement-equivalent initial stress $\underline{\Sigma}^\circ$, displacement-equivalent dynamic traction change \underline{T} , displacement \underline{u} and load \underline{L} at grid point ij and time t_i . e_1 and e_2 are orthogonal directions in the plane of the fault (strike and dip directions, respectively) (from Spudich, 1992). (b) and (c): Relation between $\underline{\phi}$, $\underline{\sigma}^\circ$ and $\underline{\tau}$ for a high initial stress case (b) and a low initial stress case (c).

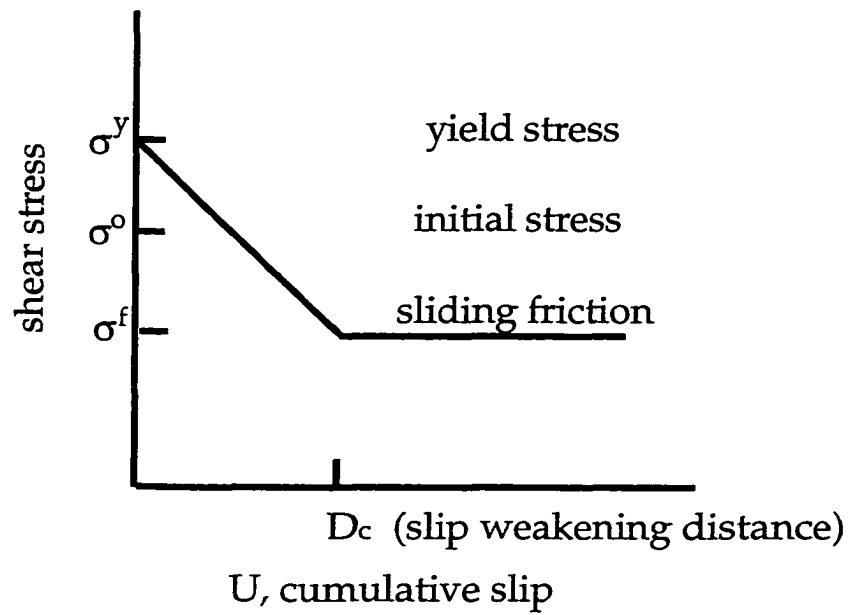


Figure 5.2: Slip-weakening friction law (Ida, 1972; Day, 1982; Andrews, 1985). The curve represents the total shear stress as a function of cumulative slip.

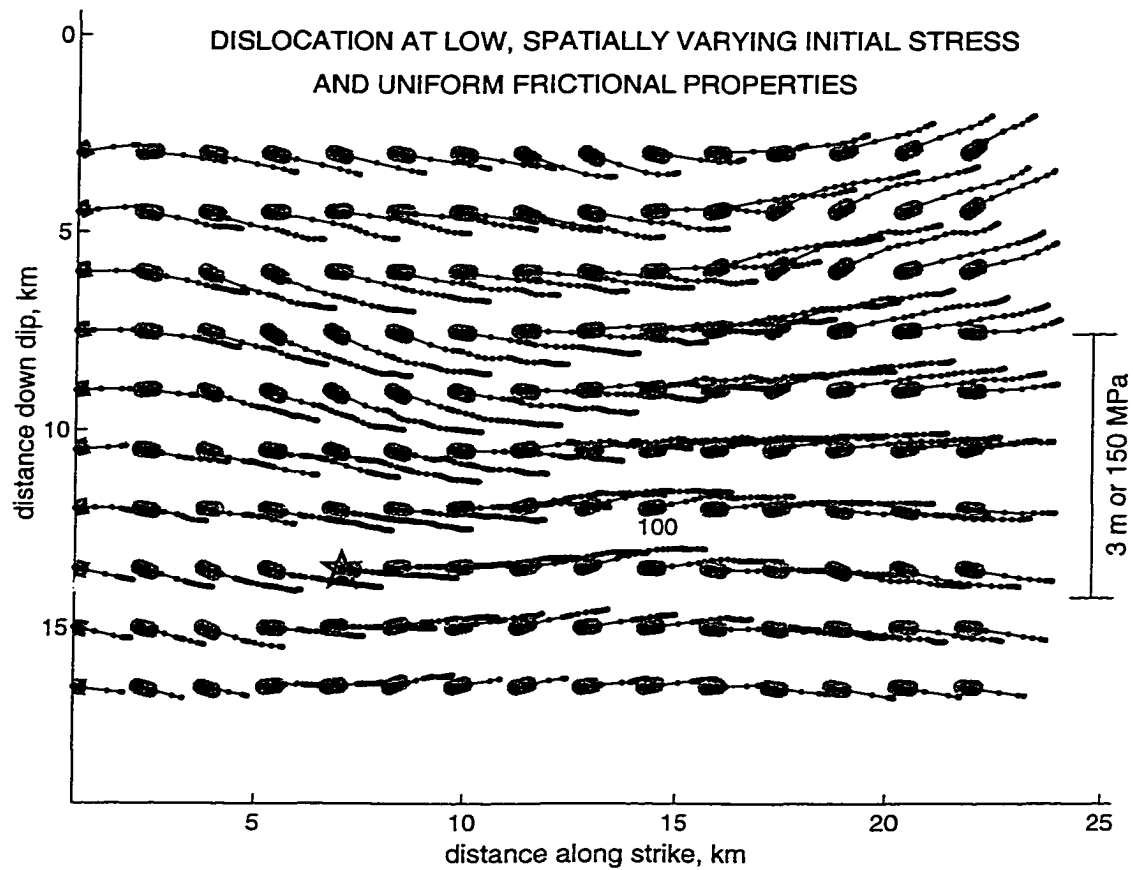


Figure 5.3: Model 1. Dislocation at low initial stress with spatial nonuniform stress direction and spatially uniform frictional properties. At each subfault the thick line represents the initial shear stress vector and the dotted line is the slip path. Incremental slip at each time step (0.125 s) is the segment between two subsequent dots. The hypocenter is at subfault 110 (6.75 km along strike and at 13.5 km depth) indicated by a star. The input parameters are the following: stress drop = 5 MPa, initial stress = 7 MPa, strength parameter = 0.7, slip-weakening distance = 0.37 m. Subfault 100 is indicated because it is analysed in fig.4.

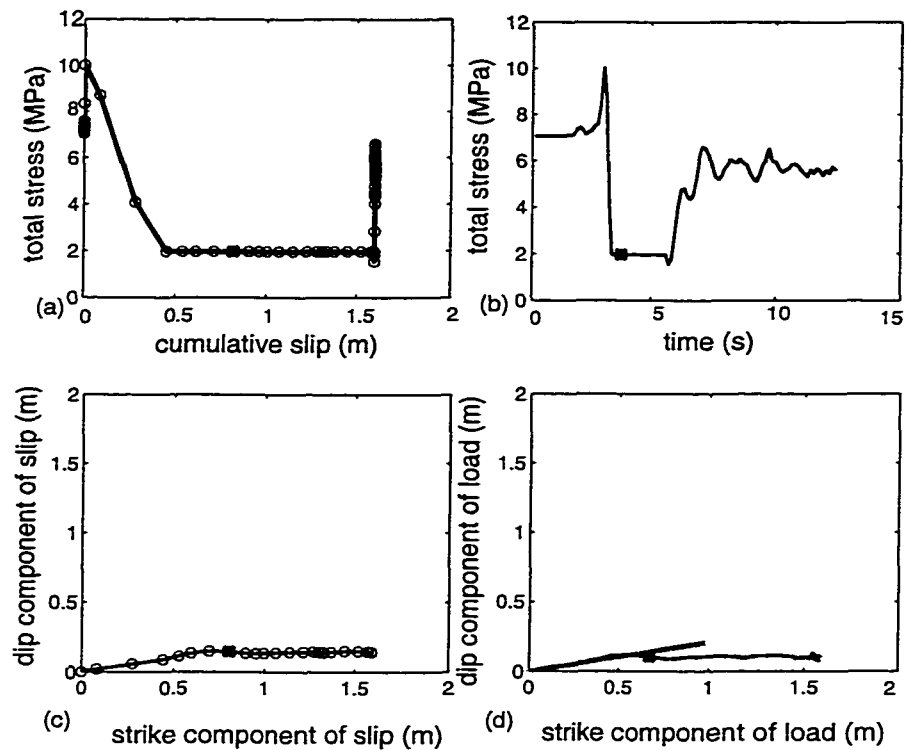


Figure 5.4: Example case: subfault 100 (at 14.25 km along strike direction and at 12 km depth). Asterisk indicates time step 29 (3.625 s), when the slip direction starts deviating from the initial rake. (a) Total shear traction as a function of cumulative slip. Rake rotates after the stress has already dropped to the sliding friction level. (b) Total shear stress as a function of time. Slip stops because of the healing criterion inserted in the dynamic calculation. (c) Slip path. Each dot indicates the incremental slip at each 0.125 s time step. (d) Load path. At time step 29 the load starts having a component perpendicular to the initial stress direction (thick straight line).

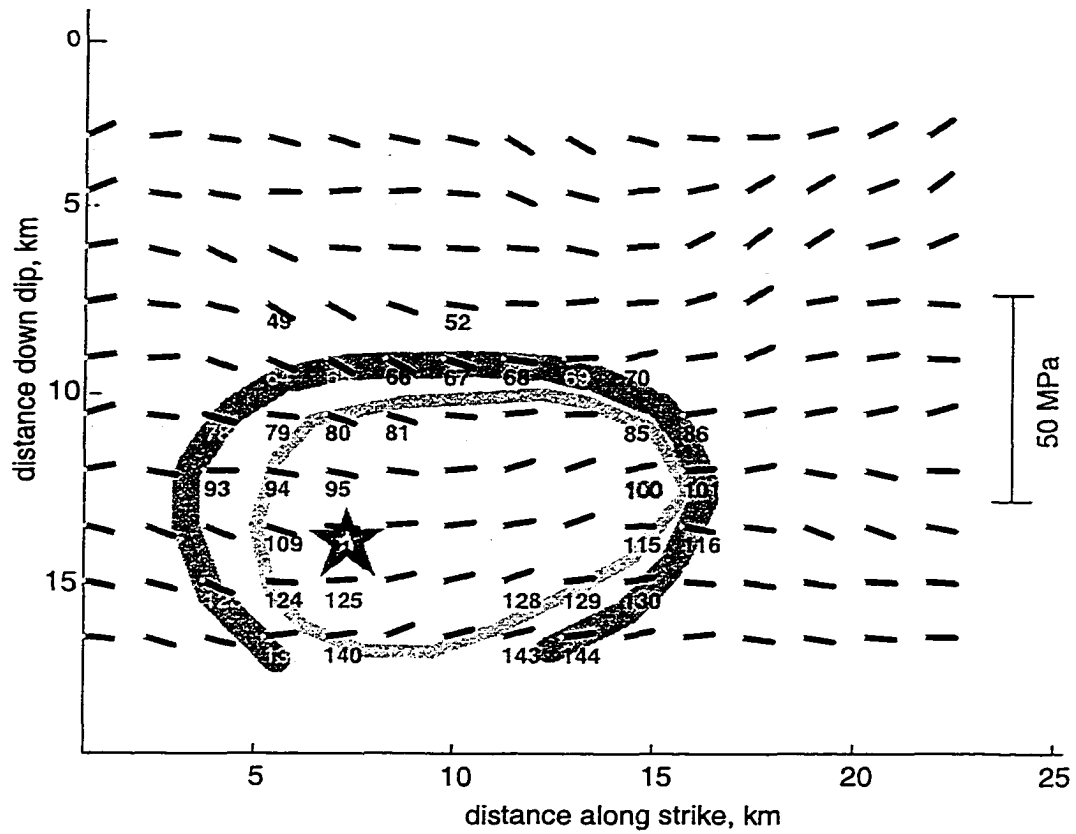


Figure 5.5: The subfaults contributing to the rotation of slip direction at subfault 100 at time step 29 are shown in bold characters. The thick and thin grey elliptical lines represent the P and S wave isochrones, respectively, relative to time step 29 and subfault 100. The subfaults that most contribute to rake rotation at subfault 100 lie on these two isochrones. At each subfault on the fault plane is shown the initial shear stress vector (thick line). The hypocenter is indicated by a star at subfault 110.

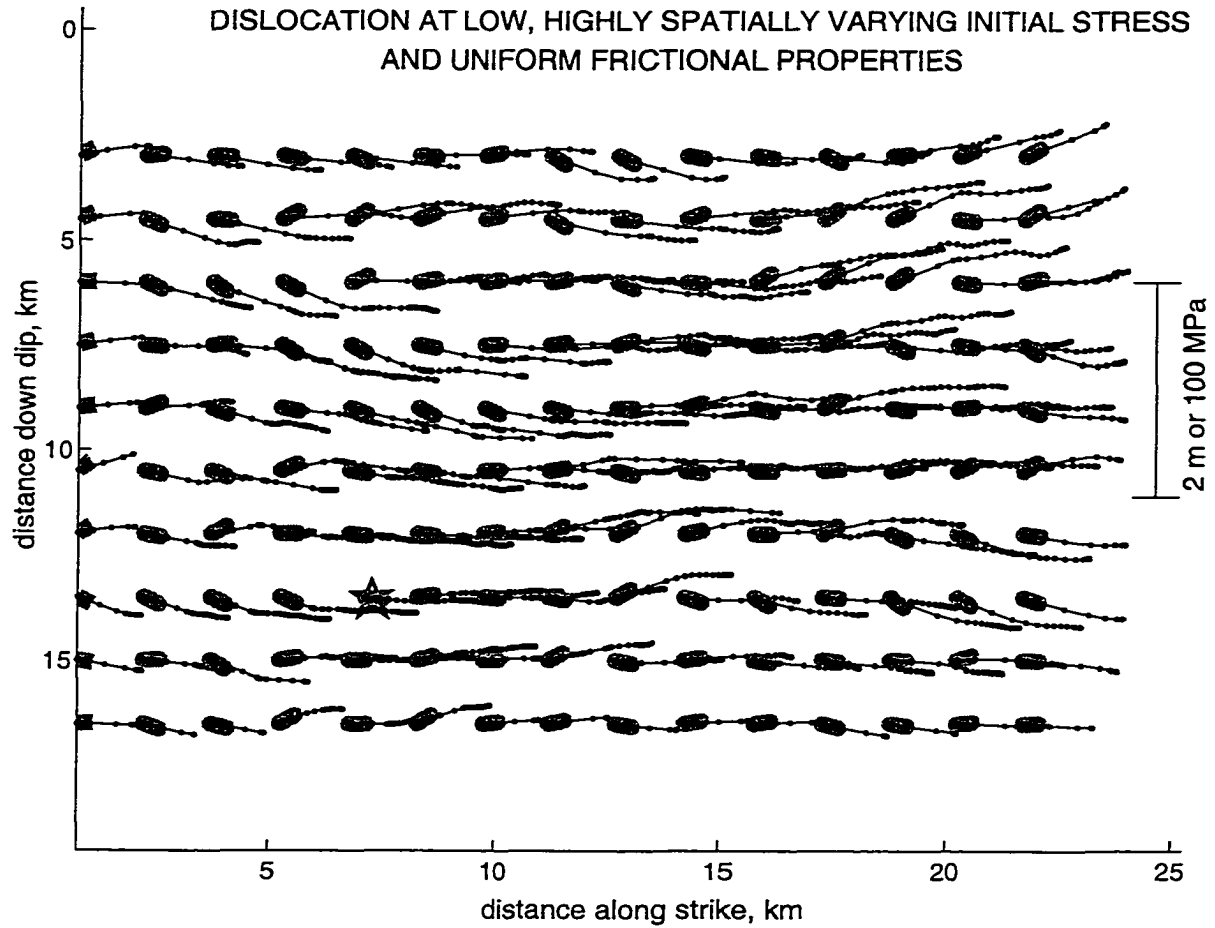


Figure 5.6: Model 2. Dislocation at low initial stress with a highly spatially heterogeneous direction and uniform frictional properties. See fig. 3 for a general explanation. Stress drop = 5 MPa, initial stress = 7 MPa, strength parameter = 0.7, slip-weakening distance = 0.37 m. Note greater rake rotations than fig. 3 and different scale.

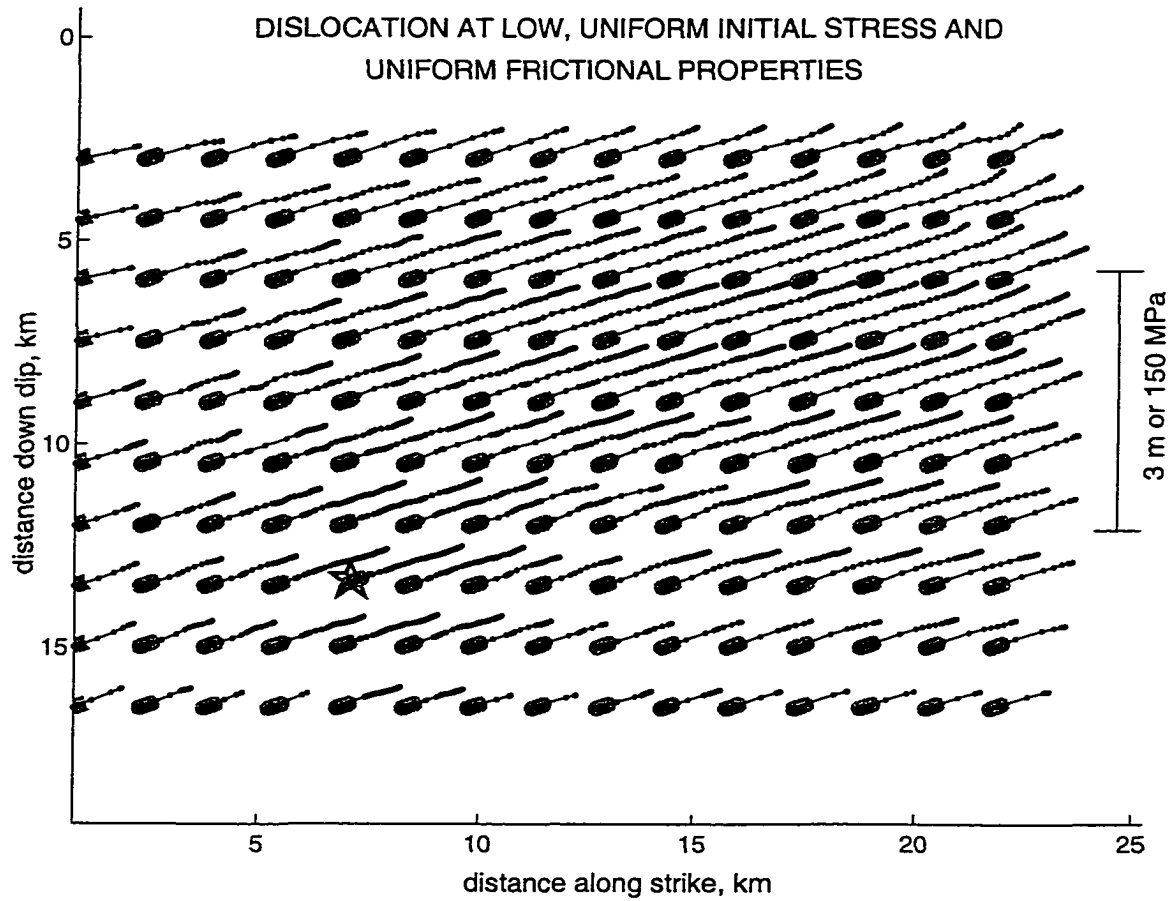


Figure 5.7: Model 3. Dislocation at low, spatially homogeneous initial shear stress and frictional properties. Stress drop = 5 MPa, initial stress = 7 MPa, strength parameter = 0.7, slip-weakening distance = 0.37 m. (See fig. 3 for more explanations). Slight rake rotations are caused by stopping phases from high strength barriers at the model periphery.

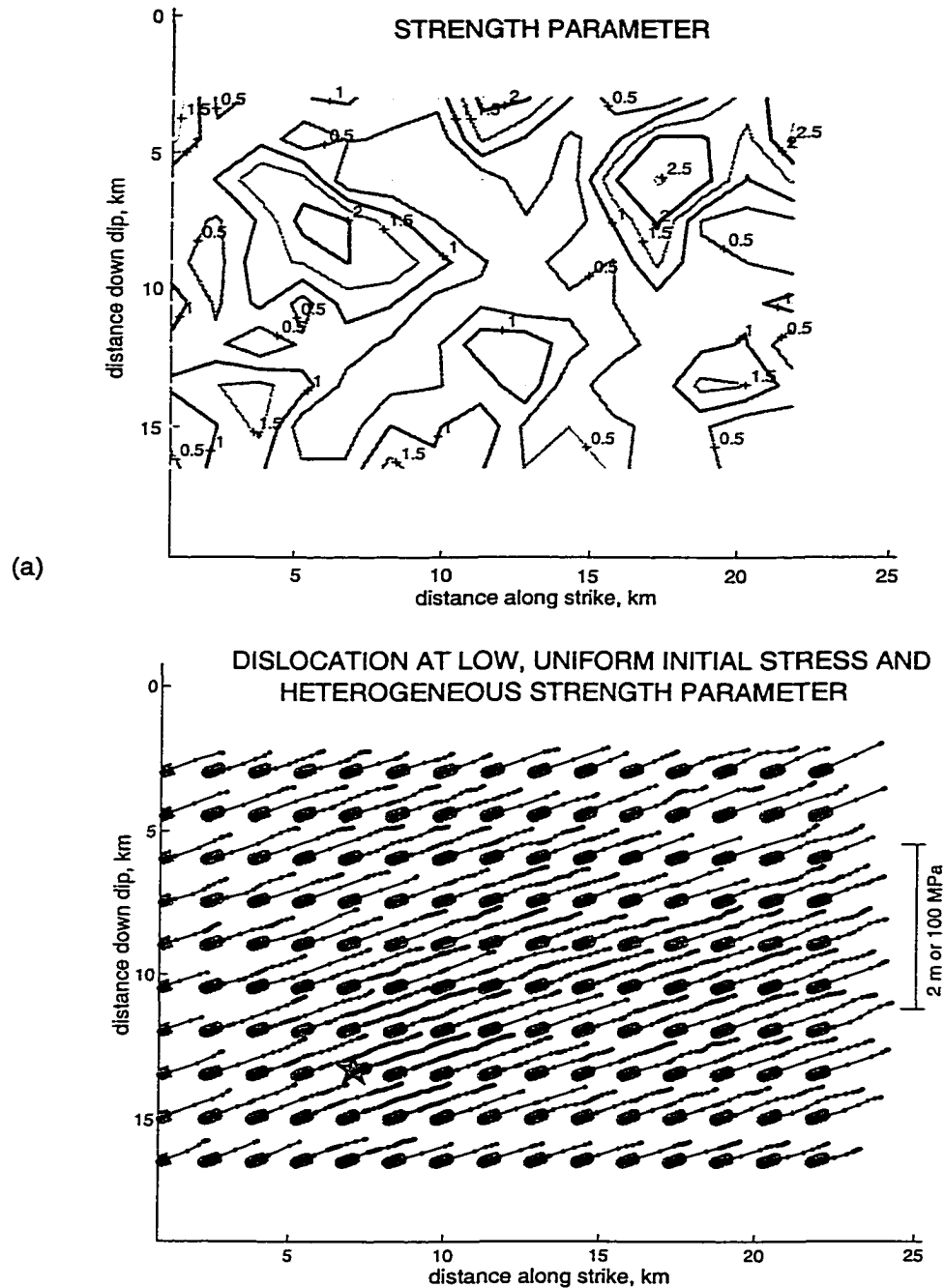


Figure 5.8: Model 4. Model with heterogeneous strength distribution and low, spatially homogeneous initial stress. (a) strength parameter distribution on the fault plane. The other input parameters are: stress drop = 5 MPa, initial stress = 7 MPa, slip-weakening distance = 0.37 m. (b) dislocation results for this model. Notice that some rake rotation occurs at a few subfault where the rupture decelerates because of the high strength value.

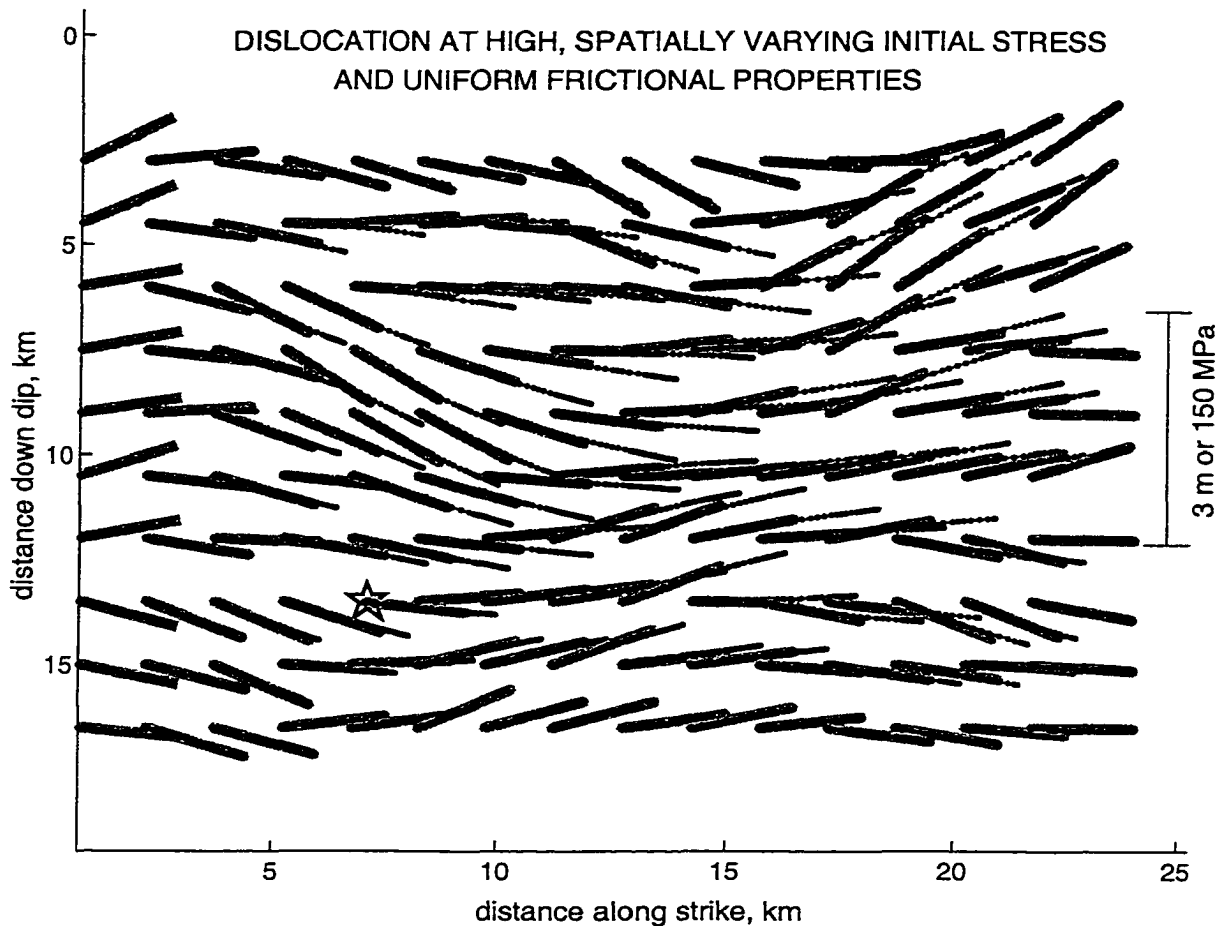


Figure 5.9: Model 5. Dislocation at high initial stress with spatially varying direction and uniform frictional properties. The input parameters are: stress drop = 5 MPa, initial stress = 60 MPa, strength parameter = 0.7, slip-weakening distance = 0.37 m. The initial stress direction distribution is the same as that in model shown in fig. 3. The heterogeneity in the initial stress direction is not sufficient to cause substantial rake rotations if the initial stress level is high.

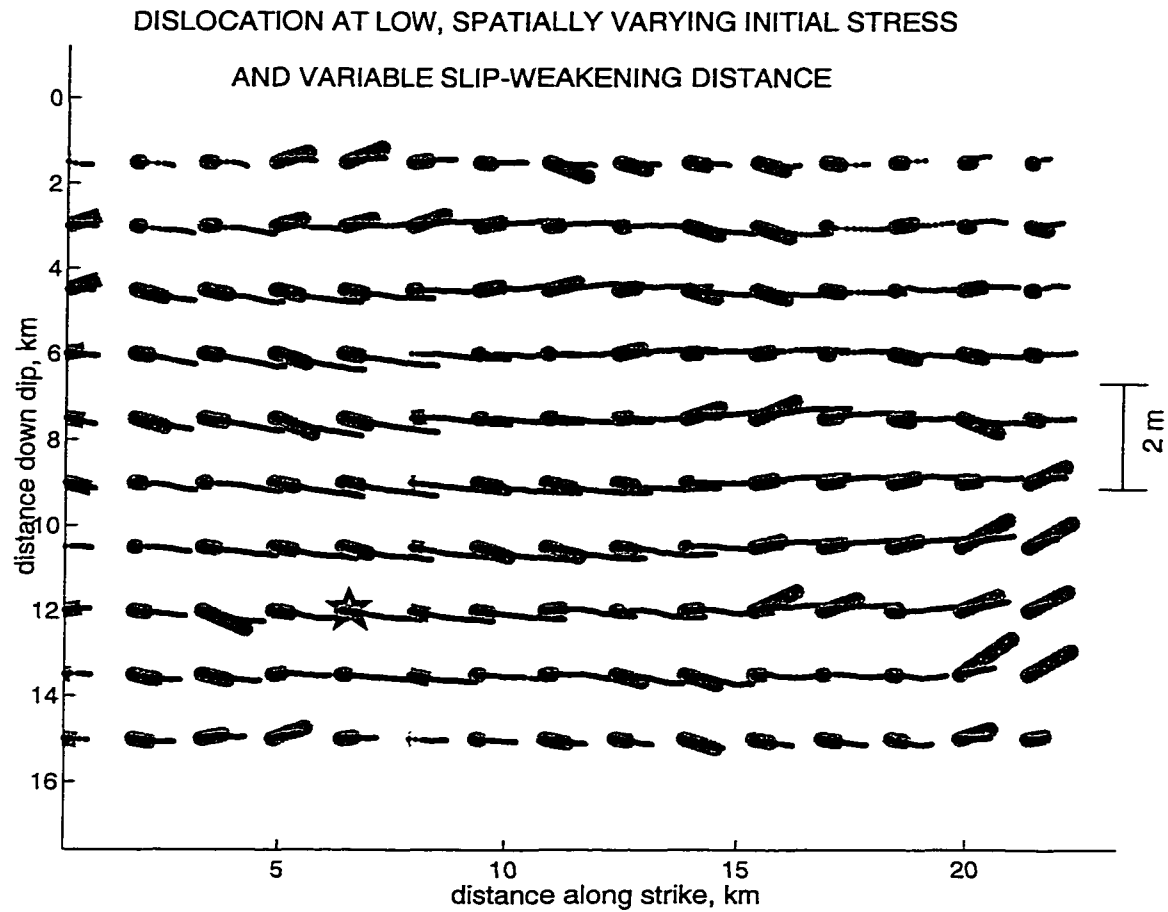


Figure 5.10: Comparison of slip-weakening distance with length of initial linear slip. Dislocation at low initial stress with a highly spatially heterogeneous direction, uniform stress drop and strength parameter, and variable slip-weakening distance. Stress drop = 5 MPa, initial stress = 7 MPa, strength parameter = 0.7. At each subfault the thick gray vector represents the slip-weakening distance in the initial stress direction. The grid interval used for this calculation is 0.75 km (time step = 0.0625 s); the figure shows subfaults spaced by 1.5 km for clarity.

5.5 Appendix

Use of Observed Temporal Rake Rotations to Infer Tectonic Shear Stress During the 1995 Hyogo-ken Nanbu (Kobe) Earthquake

We applied the method introduced by Spudich (1992) to the Hyogo-ken Nanbu rake data and inferred that the stress level on the Nojima fault before the earthquake was low (7 to 17 MPa). The coseismic fractional stress drop was of 32% at depth in the crust and complete near to the surface. These numbers are roughly consistent with the post-earthquake stresses measured by Ikeda *et al.* (1997) in a borehole near the Nojima fault at Hirabayashi and by Tsukahara *et al.* (1997) in a borehole near Ogura (Fig. 3.A1). In this Appendix we summarize the observational data and the results, and we defer the details of the method of analysis and a thorough Discussion section to Spudich *et al.* (1998).

5.3.1 Observational Evidence for Rake Rotations During the Kobe Earthquake

5.5.1.1 Striations

Otsuki *et al.* (1997) observed striations engraved during the earthquake onto the uplifted fault surface of the Nojima fault. Figure 5.A1 shows the 10 locations of the observed striations. At location 2 and 7 he observed sufficient lengths of striations to reconstruct the slip paths that we could use to infer initial stresses (Fig. 5.A2). The striations were inscribed in a film of unconsolidated fault clay several millimeters thick produced by shear during the earthquake. The fragility of the clay in which the striations were inscribed guarantees that the complicated set of striations was formed in the Kobe earthquake. The striations observed at the other locations were inadequate to allow inference of stress level, nevertheless, combined with the final offset data of Awata *et al.* (1996), imply temporal rake rotations.

5.5.1.2 Dislocation Models

Dislocation models derived by Ide et al. (1996) Ide and Takeo (1997), Wald (1996), and Yoshida et al. (1996) from geodetic data and from local and teleseismic ground-motion data show evidence of rake rotations during the earthquake. Figure 5.A3 shows dislocation at successive time steps in an interpolated version of the Yoshida slip model. (We interpolated Yoshida's original model with 4 x 4 km subfaults onto a denser grid with 1.5 x 1.5 subfaults in order to calculate the associated stress changes). Subfault 145 and its neighbors show a substantial temporal rake rotation in Figure 3.A3a, with the NW side of the fault initially moving at high velocity right laterally and downward, and subsequently moving more slowly right laterally and upward. The rotations at these subfaults occur at local maxima of slip on the Nojima fault, and therefore we will concentrate on determining the initial stress for these locations. The Rokko fault system (Fig. 3.A3b) shows substantial rake rotations only at subfault 201, which has relatively little slip and might not be well resolved by the strong-motion data. We note that the 1995 Kobe earthquake shows strong spatial rake rotations, with the final slip direction varying by as much of 80° from the Nojima to the Rokko faults, similar to the 1989 Loma Prieta earthquake (Beroza, 1991; Wald et al., 1991; Guatteri and Cocco, 1996).

Among the three dislocation models, the surface slips in Yoshida slip model are the most consistent with the observed slips and striation curvatures observed on Awaji Island. Moreover, we found that Yoshida's model is the most consistent with certain dynamic relations between slip velocity and stress change. Finally, only Yoshida's model and Ide's model agree on the direction of curvature of slip paths for subfault 145 and 201, for which we derive initial stress. For these reasons in this study we concentrate on the Yoshida slip model.

We are aware that the temporal rake rotations in Yoshida's model might not be well resolved. Because the region on the Nojima fault corresponding to subfault 145 and its neighbors has a lot of slip, the rotations there are more likely to be real than the rotations around subfault 201 on the Rokko fault. On the other hand, there are few strong-motion stations near the Nojima fault to constrain the dislocation solution there. Consequently, we guess that Yoshida's rake rotations on the Nojima fault and Rokko fault are correct with 70% and 50% probability, respectively.

5.5.2 *Method of Analysis*

Spudich (1992) developed a geometric method to infer initial stress from a dislocation model of an earthquake. In order to apply this method it is necessary to know the slip velocity and stress change time histories at the points on the fault. For this study, we reformulated it as a Bayesian calculation of the probability density function (PDF) of initial stress. We defer to Spudich et al. (1998) for a detailed description of this method of analysis.

5.3.1.1 *Calculation of Stress Changes*

Although we infer the initial stress from Yoshida's dislocation model, we also calculated the stress changes for the Kobe dislocation models of Ide and Wald. These calculations allowed us to examine the differences of the slip velocities and stress changes between the three authors' models to estimate these parameters' PDF needed in the Bayesian formulation. We derived stress changes from dislocation models using the inversion method described in Chapter 2 by imposing the slip history (constraint K3) from the dislocation model as constraint.

Each dislocation model was specified on rather large subfaults (2.5 km to 5 km in linear extent, depending on author), so we interpolated each model onto a grid having

subfaults approximately 1.5 km in length and depth (Fig. 3.A3). The slip time function in the interpolated subfaults was kept the same as that in the larger subfault of each author, and the rupture time was lagged between interpolated subfaults in order to simulate rupture propagation within the authors' original subfaults. In addition, we adjusted slip amplitude by bilinear interpolation to reduce slip discontinuities at the edges of the original subfaults. Moment was preserved in this amplitude adjustment. From each interpolated model we calculated dynamic stress changes. Our interpolated model consisted of only a single plane, whereas Yoshida's and Wald's models used two separate planes. Thus, the stresses we calculate in interpolated subfaults at the edges of the original planes are probably not correct, and we refrain from using them in subsequent interpretation. Except for regions at the edges of the original fault planes, our stresses compared well to those calculated for the Wald model by Day et al. (1998) using a finite difference method. Our interpolation method is rather crude because, strictly speaking, an inverse approach should be used to determine a finer grid of slip functions that preserve the moment rate functions of a coarser grid.

5.5.3 Results

5.5.3.1 Stresses from Yoshida's Dislocation Model

The Bayesian calculation provides a posterior density function for the initial stress, σ , however, in the interpretation of the data we are interested in the value of stress that maximizes σ (i.e. the maximum *a posteriori* probability stress, or "MAP" stress). Initial stresses derived from Yoshida's model are shown in Figure 3.A3. To produce this figure, we calculated σ for all subfaults having more than 15° rake rotation (219 out of 340). Of the 219, 187 had unconstrained stresses, leaving the 32 stresses plotted in Figure 3.A3. Of course, some of these stresses are probably not reliable because the rake rotations may not be well constrained by the ground-motion data. We believe the more

reliable stresses are those for subfaults around a local maximum of slip having a large rake rotation, which we have indicated in Figure 3.A3 with diamonds.

5.5.3.2 Stresses from Striations on the Nojima Fault

In the following we assume that the observed surface offsets and the slip paths from striations are more accurate than the slip in the surficial subfaults of Yoshida's model. In order to calculate stresses for subfaults 8 and 11 where we have observed curved striations, we built a hybrid dislocation model in the following manner. We replaced the slip at the surficial subfaults in Yoshida's model with the slip paths from the striations (for subfault 8 and 11) and from the observed offsets (subfaults 7, 9, 10, 12, 13, and 14) at the corresponding locations. We mapped the slip speed time-series from Yoshida's model onto the directions in the slip paths to determine slip-velocity time-series. We then calculated stress changes on all subfaults using this combined geological-seismological slip-velocity model. Calculated surficial stress changes were rather sensitive to our geologic assumptions, but the consequent inferred initial stresses did not depend strongly on the assumptions.

Striations at location 2 (subfault 11) are fairly consistent with an initial stress (right lateral, NW down) of (5,5) MPa. Striations at location 7 (subfault 8) do not satisfy the geometric constraint very well, but they give a MAP stress of (12, 5) MPa. For both locations, the MAP stresses are near the stress-drop vectors for the last time step, meaning that stress drop is complete. For both locations, the conclusion that stress drop is complete is probably more reliable than the specific values derived from the initial stresses.

The direction of curvature of striations at locations 2 and 7 agrees with the results discussed in this chapter. Specifically, the largest temporal rake rotations occurred at places where the initial stress direction deviated most strongly from the average initial stress direction for the whole fault. At these places, the initial slip direction agreed with

the initial stress direction, but later slip was in the direction of overall slip for the fault. Initial slip at locations 2 and 7 was dip slip, with later slip in the strike-slip direction, consistent with the dynamic models presented in this Chapter.

5.5.3.3 Comparison with Borehole Observations

The initial stresses we have inferred from striations and Yoshida's slip model agree well with independent evidence about the state of stress obtained from three boreholes drilled after the Hyogo-ken Nanbu earthquake. These were the Nojima-Hirabayashi NIED (National Institute for Earth Science and Disaster Prevention) borehole of Ikeda et al. (1996, 1997), the Nojima-Ogura borehole of Tsukahara et al. (1997), and the Ikuha borehole of Ito et al. (1997) of the Geological Survey of Japan (Fig. 3.A1). For brevity, we refer to these three holes as the Hirabayashi, Ogura, and Ikuha holes, respectively.

We resolved the borehole maximum (SH) and minimum (Sh) horizontal stresses into shear stress on an assumed vertical Nojima fault. The upper bound on this resolved shear stress is $(SH - Sh)/2$ which is everywhere 12 MPa or less (Fig. 3. A4), and is 4 to 8 MPa below the cataclastic zone in the Hirabayashi borehole. For both the Hirabayashi and Ogura holes, the actual resolved postseismic shear stress on the Nojima fault is essentially zero (Fig. 3.A4) because of the measured fault-normal compression (Ikeda et al., 1997; Tsukahara et al., 1997).

Our analysis of striations implies complete stress drop near the surface, which is consistent with the results from the Hirabayashi and Ogura boreholes. Combination of all stress measurements (Fig. 3.A5) shows some increase of shear stress with depth between 0 and 3 km. Between 3 and 11 km, there is no clear change of initial stress or postseismic stress with depth, although it should be remembered that our sampling is very sparse. Stress drop at the surface (at least for our two striation locations) is complete, but between 3 and 11 km, fractional stress drop is about 32%.

5.5.4 Implications of Low Shear Stress

Our results for the Nojima fault support the hypothesis that major crustal faults are slipping at low shear stress levels. Between 3 and 11 km depth we see no consistent depth dependence of initial stress, and we see a very slight tendency of postseismic stress to decrease with depth (Fig. 3.A5). This lack of a strong depth dependence is in accordance with the hypotheses of Byerlee (1990, 1993) and Rice (1992) that elevated fluid pressures in a highly permeable fault zone sandwiched between impermeable walls would lead to depth-independent fault strength. Zhao et al. (1996) have found evidence for elevated fluid pressure at the hypocenter of the Hyogo-ken Nanbu earthquake. Our observations of low shear stresses agree with those of Tsukahara et al. (1996), who observed very small values of $(S_H - S_h)$ in fracture zones penetrated by a 2 km deep borehole near Ashio, 100 km north of Tokyo. However, contrary to the hypotheses of Byerlee and Rice, they did not find highly elevated water pressure in the fracture zones; rather, they appeal to the effect of clay minerals to decrease frictional strength in fault zones.

This study and that of Bouchon and Streiff (1997) and Guatteri and Spudich (1998) emphasize the important interrelationships between the pre-seismic stress tensor in a region, the shape of the fault surface, and the resulting dynamics of rupture. If faults slip at low shear stress, then one of the principal stresses will be nearly fault normal (in the case of the San Andreas and the Nojima faults, that stress is S_1 , the maximum principle stress). If the fault surface has a heterogeneous orientation in such a stress field, then the direction of the initial stress can vary strongly over the fault surface (Árnadóttir and Segall, 1994), causing the spatial variations of rake, such as those seen in the Hyogoken-Nanbu and Loma Prieta earthquakes (Beroza, 1991; Árnadóttir and Segall,

1994; Guatteri and Cocco, 1996), and consequent temporal rake rotations. The strong spatial variation of rake in the Hyogoken-Nanbu earthquake indicates that the initial stress direction was highly heterogeneous on the fault, possibly caused by variations in the fault geometry. The results of Guatteri and Spudich (1998) imply that the heterogeneous initial stress direction caused the temporal rake rotations we discuss here. This mechanism is completely different from that discussed by Andrews (1994).

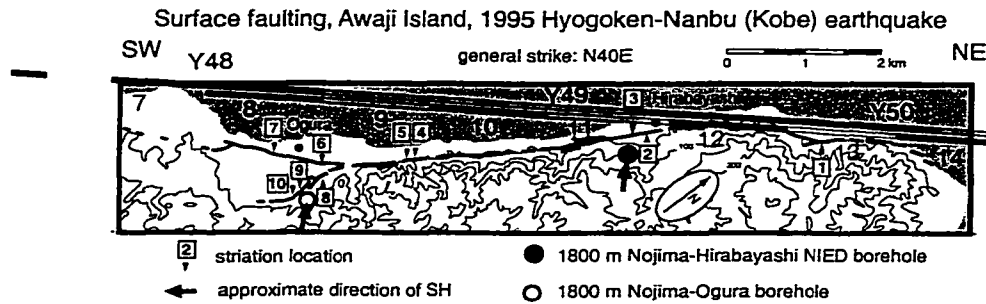


Figure 5.A1. Map of Nojima fault on Awaji Island, showing elevation (m), surface faulting (heavy line), locations of fault striations (numbers in boxes), the Nojima-Hirabayashi NIED and the Nojima-Ogura boreholes, and the subfaults (numbered) in the original (Y48-Y50) and interpolated (7-14) Yoshida slip models. Arrows show approximate direction of SH in boreholes (from Spudich *et al.*, 1998).

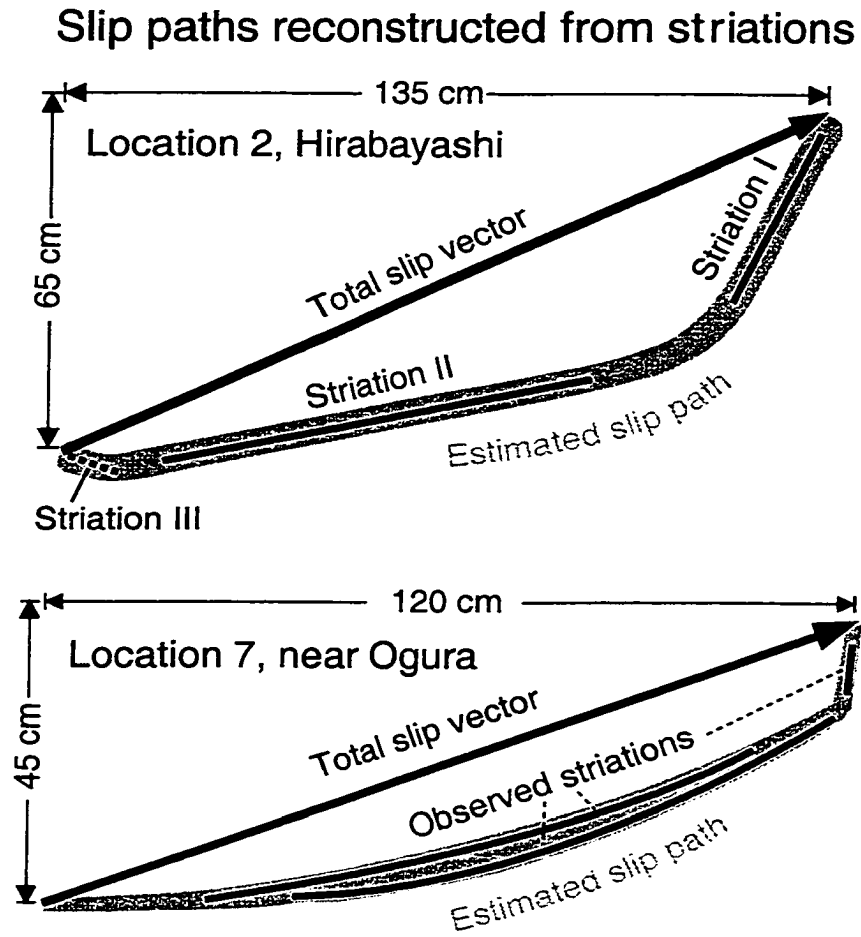


Figure 5.A2. Black lines: striations observed at locations 2 and 7. Gray bands: slip paths inferred from striation locations 2 and 7. From Otsuki et al. (1997).

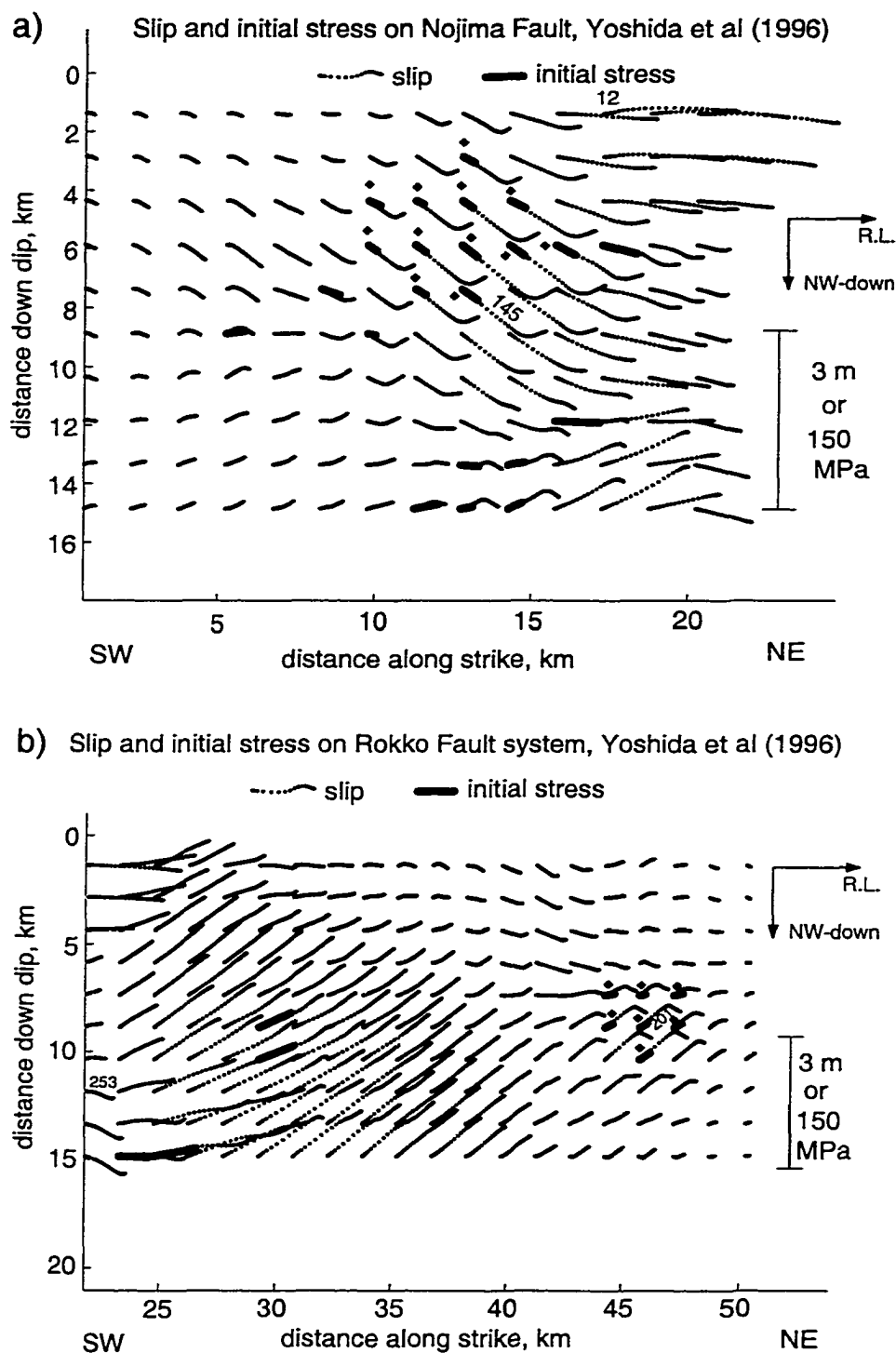


Figure 5.A3. Interpolated slip (dots) and derived initial stress vector (thick lines) for the Hyogo-ken Nanbu earthquake in the Yoshida et al. (1996) slip model. Dots show the dislocation of the NW side of the fault at time increments of 0.125 s for each subfault. At subfaults where no initial stress vector is shown, the motions did not specify a unique initial stress. A few subfaults are numbered. Diamonds indicate more reliable stresses. a) Nojima fault. b) Rokko fault system (from Spudich *et al.*, 1998).

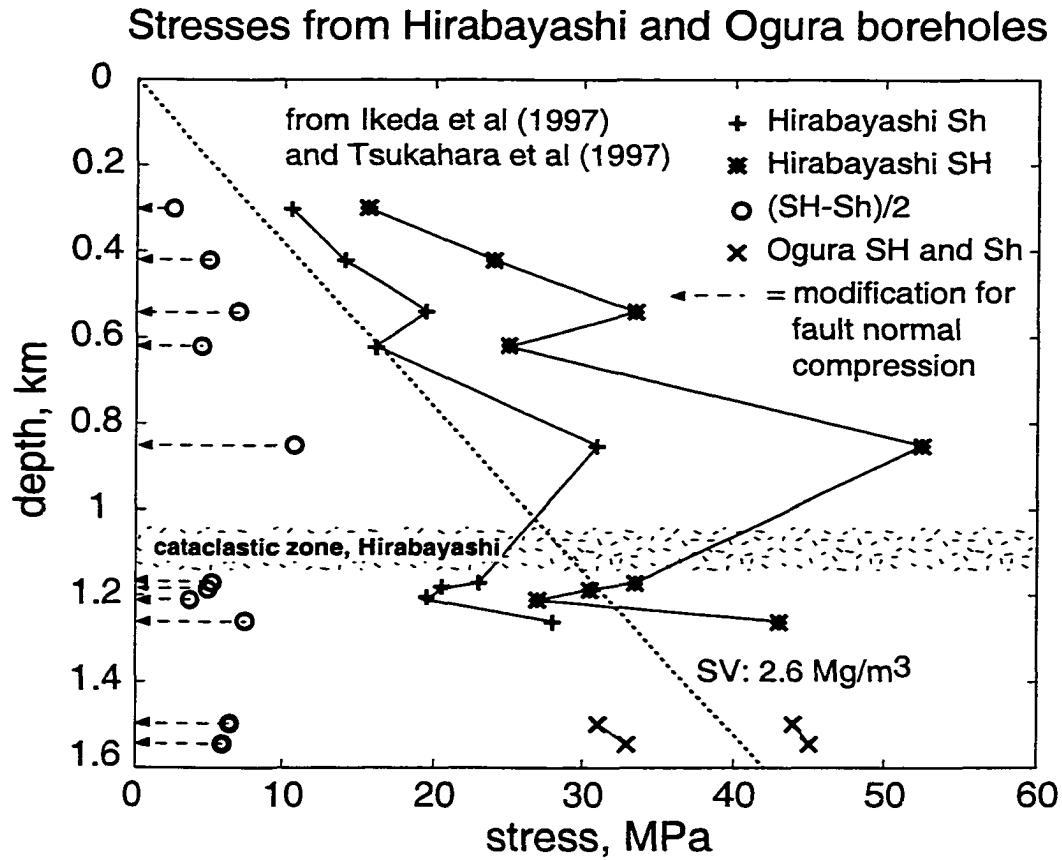


Figure 5.A4. Maximum (SH) and minimum (Sh) horizontal stresses measured by hydrofracturing by Ikeda et al. (1997) and Tsukahara et al. (1997) after the Hyogo-ken Nanbu earthquake in the Hirabayashi and Ogura boreholes, respectively (Figure 5.A1). Circles show the upper bound on the post-earthquake shear stress on a vertical plane. At both boreholes SH was approximately normal to the fault; dashed lines show resulting modified shear stress on the fault. The Hirabayashi borehole passed through a cataclastic zone inferred to be the Nojima fault at depths of 1.1-1.3 km. SV is the assumed vertical stress (from Spudich *et al.*, 1998).

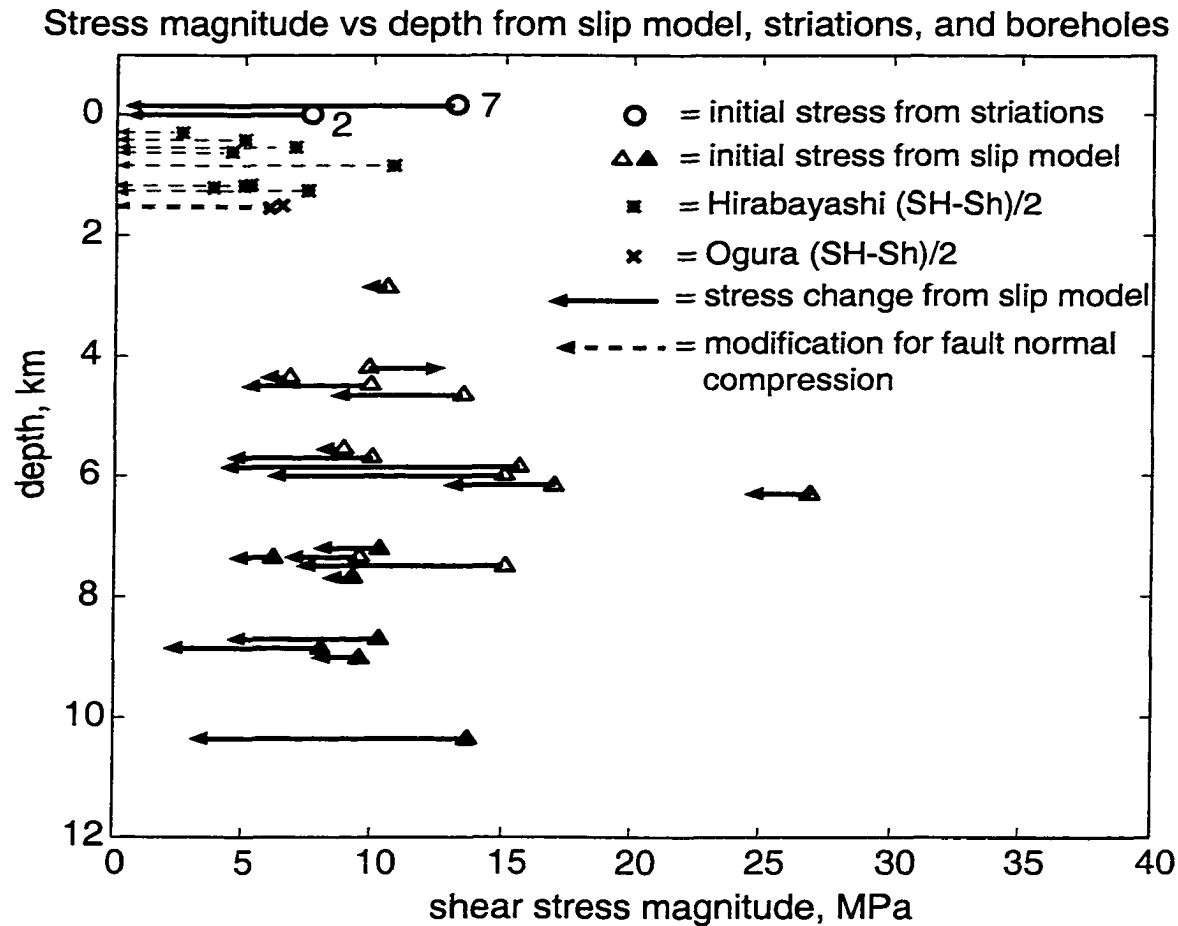


Figure 5.A5. Shear stress on the Nojima fault as a function of depth, from all methods. Circles: pre-earthquake stresses from striations (location number indicated). triangles: pre-earthquake stresses from temporal rake rotations of selected subfaults (diamonds in Figure 5.A3) in Yoshida model. Open triangles are for Nojima subfaults and filled triangles are for more speculative results from the Rokko subfaults. Solid lines: Coseismic stress changes inferred from our hybrid dislocation model. x and *: post-earthquake maximum shear stress from borehole measurements at Ogura and Hirabayashi, respectively. Dashed lines: modification to borehole shear stress to correct for observed fault-normal compression (from Spudich *et al.*, 1998).

Chapter 6 – Strong-Ground Motion Simulation with Stochastic-Dynamic Rupture Models

- 6.1 Introduction
- 6.2 Method
- 6.3 Models
- 6.4 Strong-Ground Motion Simulation
- 6.5 Discussion

Abstract

Finite-fault images of the spatial and temporal evolution of earthquake slip show that fault slip is spatially variable at all resolvable scales. There is also evidence that rupture velocity is spatially heterogeneous, although it is more difficult to resolve variations in the rupture velocity from strong motion data. Complexity of the rupture process exerts a strong influence on the variability and level of damaging strong-ground motion in earthquakes. Adequate predictions of the intensity and variability of ground motions from future earthquakes strongly depends on our ability to realistically model source complexity. A dynamic description of the rupture process provides a self-consistent way of describing the variability of all the relevant source parameters without prescribing their spatial distribution a priori.

Using a Boundary Integral Method we simulate dynamic rupture of hypothetical earthquakes having stress drop distributions consistent with the random-field model of earthquake slip developed by Mai and Beroza (1999). We assume a slip-weakening model and prescribe the distribution of apparent fracture energy that determines a subshear rupture velocity. We obtain physically consistent rupture models that reflect the statistical properties of slip heterogeneity found in finite-source models of past earthquakes. These dynamic models contain the full space-time evolution of the rupture process, and hence the time dependence of slip is a derived, rather than an assumed, parameter. We use these rupture models to compute theoretical strong motion seismograms up to a frequency of 2 Hz for several scenario earthquakes (strike-slip, $M_w = 7.0$) at multiple observer locations. We compare horizontal empirical-response spectra with values obtained from our dynamic models and corresponding kinematic simulations. We find that including spatial and temporal variations in slip, slip rise time, and rupture propagation consistent with dynamic rupture models exerts a strong influence on near-source ground motion and has the potential to improve current strong ground motion prediction procedures. Our results suggest that variability in the rupture time distribution may be included in kinematic models through a generalization of Andrews (1976a) result relating rupture speed to apparent fracture energy, stress drop, and crack length.

6.1 Introduction

The observed strong ground motion for recent earthquakes (1989, Loma Prieta; 1992, Landers; 1994, Northridge; 1995, Hyogo-ken Nanbu (Kobe)) questions our current ability to correctly predict strong ground motion in the near-source region of large earthquakes. Ground motion prediction equations, known as ‘attenuation laws’ (e.g. Boore and Joyner, 1997; Abrahamson and Silva, 1997) are empirical relationships that relate the intensity of observed strong ground motion, such as peak ground acceleration (PGA) or spectral acceleration (S_a), to magnitude, distance, faulting style and other parameters describing the particular event and the particular site conditions. The limitations of the current attenuation laws derive in part from their underlying simplifying assumptions and averaging procedures. Another limitation on the reliability of these predictive equations arises from the sparse data distribution of long period strong motion recordings in the near-field ($R < 10$ km) of large earthquakes. To overcome this deficiency it is common practice to extrapolate ground motion parameters close to the source from larger distances ($R = 20$ -50 km). Still, such unconstrained extrapolation might not yield an adequate characterization of the extreme near-field where ground motion exhibits strong variability. Near-source ground motion is largely dominated by long-period energy (< 1 Hz) that is strongly affected by wave path effects, such as basin-edge geometry, and source directivity (e.g. Wald *et al.*, 1991; Cohee and Beroza, 1994; Olsen and Archuleta, 1996; Kamae and Irikura, 1998). The significant impact on the dynamic response of large structures exerted by long-period energy demands more accurate representations of near-source ground motion characteristics than those provided by extrapolating empirical predictive equations. Deterministic approaches to strong-ground motion simulations from several earthquake source realizations have the potential to correctly reproduce and predict these low-frequency characteristics in the near-field of large earthquakes.

Recent work based on kinematic source modeling has addressed the problem of simulating realistic near-source strong-ground motions for future earthquakes. In particular, large effort has been put into developing hybrid methods for near-fault broadband strong-ground motion simulations that combine both deterministic and stochastic-empirical approaches (e.g. Herrero and Bernard, 1994; Kamae *et al.*, 1998; Hartzell *et al.*, 1999; Pitarka *et al.*, 2000). While the high frequency ground motion is usually treated stochastically, long period ground motions are often treated deterministically and strongly source-controlled, implying that the unknown source characteristics of future earthquakes introduce large uncertainties in the prediction of near-fault ground motion. Somerville *et al.* (1999) and Mai and Beroza (1999) have developed methods to characterize slip models of future earthquakes for use in the prediction of strong ground motions. In particular, Mai and Beroza (1999) have proposed a description of earthquake slip as a spatial random field based on the analysis finite-source rupture models available in the literature.

Source complexity may be manifested not only as local variations in static slip, but also as heterogeneity in rupture velocity, slip-velocity and slip duration. The combination of this heterogeneity contributes to intermediate and high frequency radiation, and may also affect longer period ground motions. While a source characterization including variability in all the relevant parameters would be ideal for ground motion prediction, it is not necessarily clear how to constrain variations in rupture velocity and source time function parameters (slip-velocity and duration) in kinematic rupture models. Kinematic modeling limits the possibility to include variability in the source parameters in a self-consistent manner. While the complexity of the slip distribution can be inferred from available source models, the variability of the other relevant source parameters is either neglected or assumed a priori based on theoretical spectral models (e.g. Bernard *et al.*, 1996; Hisada, 2000).

Dynamic modeling of the rupture process provides a self-consistent way of describing the variability of all the source parameters without prescribing their spatial distribution a priori. Simulating strong-ground motion with dynamic models is much less efficient than using a kinematic approach, especially if many realizations are required to routinely estimate averages of the expected ground motion intensity at several observer

locations. On the other hand, dynamic modeling allows us to identify the relevant source effects that should be included in a realistic source realization, and to determine simple relations between kinematic source parameters that could be included in kinematic source parameterizations. In this chapter we perform dynamic rupture modeling as a means of constraining unmodeled aspects of kinematic rupture models. The resulting model is a realization of the earthquake rupture process that is based on our current knowledge of the physics of the earthquake source.

Andrews and Boatwright (1998) have used this approach previously to calculate far-field ground motion spectra with dynamic-stochastic rupture models using a finite-difference spontaneous rupture code. However, the variability in the slip distribution in their study was not meant to be consistent with the observed complexity of published dislocation models. In our study we simulate seismograms up to 2Hz with dynamic-stochastic rupture models obtained using a Boundary Integral Method and constrained to be consistent with the random-field model of earthquake slip developed by Mai and Beroza (2000). Our main goals are to determine whether and how the inclusion of a more realistic source complexity improves our ability to estimate strong-ground motion in the near source. We compare simulated acceleration response spectra (S_a) from our dynamic models to empirical values predicted by attenuation laws and to those calculated from kinematic models that are heterogeneous in the slip distribution only. We will concentrate on the intermediate and long periods ($> 0.7s$) radiation that is the most sensitive to source effects.

6.2 Method

6.2.1 Stochastic-Dynamic Rupture Modeling

We model spontaneous rupture by means of the boundary integral method (BIM) (Boatwright and Quin, 1986; Das and Kostrov, 1987; Quin and Das, 1989) outlined in Chapter 2. We modified the original code in order to include free-surface effects, vertical heterogeneity in the velocity structure, and a slip-weakening friction law. The ingredients needed for spontaneous rupture modeling are the distributions of stress parameters over the fault plane and the specification of the friction law that governs the failure process.

6.2.1.1 Stress Drop

In all our rupture models we assume a homogeneous distribution of initial stress over the fault plane. In our calculations, the strongest constraint derives from the requirement that our rupture models be consistent with the slip heterogeneity found in finite-source models of past earthquakes. We accomplish this task by imposing the static stress drop distributions derived from a set of slip realizations generated following the random-field model of earthquake slip developed by Mai and Beroza (1999).

6.2.1.2 Friction Law

Our assumed friction law is a simple slip-weakening model (Fig. 3.1) (Ida, 1972; Andrews, 1976a; 1985; Day, 1982) that may be considered a reasonable approximation of more general constitutive behavior of the fault during dynamic motions (e.g. Okubo, 1990; Ide and Takeo, 1997; Guatteri *et al.*, 2001). Given the initial value of shear stress, the slip-weakening friction law is entirely parameterized by the stress drop, $\sigma^o - \sigma^f$, the strength excess, $\sigma^y - \sigma^p$, and the slip-weakening distance, D_c . D_c is the distance over which the stress drops linearly from its peak value to its final or residual level. The slip-weakening relation eliminates the unrealistic singularity in stress and particle velocity at the crack tip implied by an abrupt stress drop. The elimination of this singularity and the introduction of a characteristic length result in a finite amount of energy absorbed at the rupture front. In this study we are not concerned with the investigation of detailed dynamic source properties. Rather, we aim to design possible rupture models that are consistent with observed slip and that can be specified using a small number of dynamic parameters.

6.2.1.3 Apparent Fracture Energy

Guatteri and Spudich (2000; Chapter 3) showed that, in a rupture model with a given stress drop distribution, D_c and strength excess trade-off in controlling the rupture velocity. Even though different values of D_c and strength excess result in different source time functions, only the analysis of high-frequency data (>1Hz) would be able to resolve these differences. To overcome this ambiguity, a single parameter, the apparent fracture

energy G_c can be used to describe the frictional properties of the fault that control rupture propagation. Fracture energy is defined as the amount of energy required to create a unit area of shear fracture. In a simple slip-weakening model is calculated as the area underneath the slip-weakening curve (Fig. 3.1). In general, as pointed out by Andrews (1976a) and Okubo and Dieterich (1994), G_c need not be a material constant. For a given stress drop distribution, the value of fracture energy may be representative of the resistance of the fault to failure. In this study we will therefore describe our dynamic input parameters in terms of stress drop and fracture energy solely.

For each model, we initially prescribe the fracture energy distribution obtained from the respective stress drop distribution and spatially homogeneous values of strength excess and slip-weakening distance. Then, by *trial and error* we perturb the distribution of $\sigma^y - \sigma^p$ and D_c on selected portions of the fault plane, in order to obtain the fracture energy distribution that results in a subshear rupture speed over most part of the fault and as an average value. The values that we obtained are in agreement with fracture energy estimates for past earthquakes (e.g. Rice, *personal communication*; Beroza and Spudich, 1988; Guatteri *et al.*, 2001).

6.3 Models

Our scenario earthquakes are designed to be representative of strike-slip, $M_w = 7.0$ events in California. We assign a fault length $L = 36$ km and a fault width $W = 16$ km determined from recent source-scaling relations for our selected magnitude (Mai and Beroza, 2000). We discretized the fault plane into 960 subfaults with a width of 750 m. Accordingly to Andrews and Boatwright (1998) study, this grid size should result in accurate ground motion spectra up to about 1.5 Hz. We computed ground velocity at the observer locations shown in Figure 6.1 using the method of Olson *et al.* (1984) and Spudich and Archuleta (1987) assuming the generic velocity structure for California (Boore and Joyner, 1997). We calculated seismograms in the frequency band 0-2.3 Hz and lowpass filtered them with a cosine taper between 2 and 2.3 Hz. The ground velocity time-series were sampled at a rate of 0.1 s.

We subdivided our models into two sets. The first one consists of three rupture models (A, B, and C) based on three different slip realizations having the same hypocenter at a depth of 11 km and at 10 km along strike from the left boundary of the fault. This first set of models will allow us to account for the effect of variability in the source parameters on ground motions.

The second set of simulations is meant to include variations in directivity effects. We selected the stress drop derived for Model B and generated three different dynamic rupture models (D1, D2 and D3) having the hypocenter located at 11 km depth and at 15, 20, and 25 km along strike from the left boundary of the fault, respectively.

6.3.1 First Set of Dynamic Models

Figure 6.2 shows side by side the respective distributions of source parameters for the three models. In the first row of panels (Fig. 6.2a-c) we show the three slip distributions obtained as a result of our dynamic simulation ('dynamic slip') of the 'kinematic' slip distribution generated following Mai and Beroza (1999). In general, the dynamic modeling resulted in a slightly smoother slip distribution compared to the original kinematic slip. Figures 6.2d-f show the distributions of static stress drop derived from the kinematic slip distribution using the method of Andrews (1980). Figures 6.2g-i show the distribution of apparent fracture energy on the fault. The spatial variability is strongly related to the respective stress drop distribution. This similarity mainly depends on the fact that in our models the heterogeneity of the stress drop distribution dominates over the relatively smooth strength excess and slip-weakening distance distributions. Figures 6.2l-n depict contours of the rupture times on the fault obtained as a result of the dynamic modeling. In Figure 6.3 we show contours of slip-velocity averaged over depth as a function of distance along strike and time, together with reference lines having slopes of 2 km/s, 3 km/s and 4 km/s. These plots show that the average rupture velocity over the fault plane is subshear, as it is locally for main parts of the fault. The width of the contour is indicative of the local slip duration (rise time), and more detailed representation of the distribution of rise time, here defined as the time required to accumulate from 10% to 90% of the total slip, is given in Figures 6.2o-q. It is important to notice that the variability in the rupture time and rise time distributions is a derived,

rather than an assumed characteristic of the rupture model. However, it depends on the assumptions used to obtain the distribution of fracture energy.

6.3.2 Second Set of Dynamic Models

As for the previous set of models, we summarize the distributions of the relevant source parameters of the three models D1, D2, and D3 in Figure 6.4. The final slip distributions of Model D1, D2, D3 (Figures 6.4a-c), and Model B (Figure 6.2b) are very similar, the respective stress drop distributions are the same (Figures 6.4e-g), while the fracture energy distribution differs among the four models (Figures 6.4g-i and Figures 6.2i). Figures 6.5a-c show the contours of depth-averaged slip-velocity as a function of distance along strike and time for the three new examples. Notice that moving the hypocenter position affects the relative time at which different parts of the fault radiate and how waves radiated during slip will interfere with one another. In the following section we will also discuss how the location of the hypocenter affects the shape of the source time function on different parts of the fault.

6.3.3 Source Parameters

In typical kinematic modeling, the rise time and the slip velocity function (source time function) are usually distributed uniformly over the fault, while the rupture velocity is fixed to some fraction of the local shear wave speed. In contrast, Figures 6.2, 6.3, 6.4 and 6.5 show that the resulting spatial-temporal rupture evolution from our dynamically plausible rupture models is substantially complex.

6.3.3.1 Rupture Velocity

Andrews (1976a) obtained an analytical relation between rupture velocity and fracture energy, stress drop and crack length valid in simple antiplane strain with uniform stress drop and frictional properties. Even though his relation (his equation 23) does not directly apply to 3-D heterogeneous dynamic simulations, Guatteri and Spudich (2000) have generalized his result to more realistic dynamic models through numerical simulations. To help develop realistic source characterizations, it is important to discuss how rupture velocity is expected to vary over the fault plane for a given slip model. In

this study we assume that rupture propagation occurs at sub-shear speed over most parts of the fault, as inferred for the majority of instrumentally recorded earthquakes.

As the crack grows, the rupture tends to accelerate (Andrews, 1976a; 1985; Day, 1982) due to the effect of dynamic loading coming from the ruptured area of the fault. Areas of local high stress drop also promote fast rupture propagation. For example, Model A has two relatively large stress drop patches, one around the hypocenter and the other at about 15 km from the nucleation region, at a distance where the dynamic loading has already a large effect. The high stress drop around the hypocenter determines fast initial rupture propagation, while the second area promotes rupture acceleration and increases the dynamic loading on both the ruptured and not ruptured areas of the fault. Relatively large values of fracture energy, corresponding to high fault resistance, are needed there to slow down the accelerating rupture growth. The variability in the rupture time distribution is a result of heterogenous stress drop and fracture energy distributions.

From a physical point of view it is interesting to ask why the fracture energy should vary on the fault plane such that the rupture velocity remains sub-shear. We should keep in mind that we are modeling specific slip distributions that, together with the constraint on rupture speed and our assumption of fault constitutive behavior, imply specific physical fault properties reflected in the fracture energy distribution. For earthquake scenarios consistent with events having super-shear rupture propagation (e.g. 1979 Imperial Valley and 1999 Izmit earthquakes), the same slip distributions would imply different fracture energy and, therefore, different fault physical properties.

In the second set of models, while the median values of G_c are comparable (Table 6.1), the locations of area with large values of fracture energy differ, depending on the respective hypocenter locations. As discussed above, local large values of G_c are necessary as soon as the crack has extended over large distances. Figure 6.6a shows the depth-averaged fracture energy for Model B (continuous line) and Model D3 (dashed line) that represent the two extremes with regard to the effect of hypocenter position on the local rupture velocity. We rewrite equation 23 in Andrews (1976a) (notice that in Andrews' equation 23 $G = G_c/2$) in terms of the dimensionless parameter $V = \mu G_c / (\Delta\sigma^2 L_h)$:

$$1 - v^2/\beta^2 = C(V/2)^2$$

where v is the rupture speed, β is the shear speed, μ is the shear modulus, $\Delta\sigma$ is the stress drop, and L_h is the crack length (distance from the hypocenter). For a simple antiplane strain, C is about π^2 . Even though Model B and model D3 have different hypocenter positions, their rupture speeds are very similar especially away from the hypocenter ($L_h > 7$ km). In Figure 6.6b the similarity between the parameter V for these two models suggests that Andrews' relation applies to 3-D heterogeneous dynamic models. Let us consider that on average the rupture speed is 85% of the shear velocity. The median value of V for model B is about 0.4, from which we can empirically determine $C \approx 7$ that is comparable to Andrews' result. This relation may be used to generate realistic rupture time distributions to design generalized source models for strong-ground motion predictions.

6.3.3.2 Rise Time and Slip Velocity Function

A complete source description requires the definition of the time dependence of slip after rupture (slip velocity function, SVF). In Figure 6.7 we show SVFs derived from the dynamic models B, D1, D2, and D3 at different locations along strike and at the same depth of 7 km. The purpose of this figure is to show how the SVF varies between different parts of the fault depending on local frictional parameters and dynamic loading. Over the rupture area, the SVF can have various shapes resembling overlapping triangles (e.g. Wald *et al.*, 1991), truncated Kostrov functions (e.g. Beroza and Spudich, 1988), or cosine slip functions (Hartzell *et al.*, 1996; Cotton and Campillo, 1995). While such variability in the slip velocity function is usually not considered in kinematic source characterizations, it is indeed a reasonable and expected property of a complex rupture model.

Large dynamic loading (at points distant from the hypocenter) has the effect of narrowing the SVF resulting in large peak slip-velocities. The effect of a local large stress drop is identifiable in similar effects on the slip velocity function. These examples are intended to be representative of the degree of variability of the SVF over the fault for a relatively complex rupture model. Guatteri and Spudich (2000) showed that, with a slip-weakening model, individual values of strength excess and D_c affect the local shape of

the SVF without affecting the calculated waveforms and spectra over a limited frequency band ($< 1\text{Hz}$).

Because it is difficult to directly measure slip rise time for a given earthquake, this parameter is usually inferred from values used in deterministic modeling of observed ground motions. Heaton (1990) analyzed the rise time values obtained from these modeling studies and concluded that only a narrow band of the fault is rupturing at a given point in time. Recent studies (e.g. Cotton and Campillo, 1995; Hartzell *et al.*, 1996) suggest correlations between slip magnitude and slip rise time, yielding values of rise time consistent with Heaton's observation. Somerville *et al.* (1998), based on the analysis of slip rise times inferred for a number of moderate to large earthquakes, have proposed a relation between earthquake magnitude and slip rise time.

In our dynamic simulations, the pattern of variation in the distribution of rise time over the fault (Figures 6.2o-q) is typical for a crack model governed by a slip-weakening model (e.g. Day, 1982). The rise time is large around the hypocenter and gets shorter close to the edges of the fault, with values depending on the total rupture duration. Heterogeneity in the stress parameters adds additional variability in the typical rise time distribution. The differences in the slip rise time distribution between Model A, that has the roughest slip distribution, and the other models, reveal a weak correlation between slip magnitude and rise time.

Contrary to simple kinematic parameterizations, due to the more complicated shape of the SVF (Figure 6.7), our measured values of rise time might not provide a good quantitative estimate of the time over which the most energetic radiation is released from a given point on the fault. For example, in Figure 6.7 the SVF of model D1 at 10 km on the left away from the hypocenter has a rise time of about 3.5 sec, while the most energetic radiation is released in about 1.2 sec, corresponding to the width of the initial slip-velocity pulse. Shortening D_c and increasing the strength excess would have the effect of concentrating the most energetic radiation in a shorter time (Guatteri and Spudich, 2000). However, in this study we mainly concentrate on the intermediate-low frequency range, where these differences would be less important, and we chose relatively large values of D_c (about 0.5 to 1m) in order to minimize the discretization

noise of the dynamic calculation. Later we will show that using a shorter D_c affects the simulated response spectra a short periods.

TABLE 6.1

| | <i>Model A</i> | <i>Model B</i> | <i>Model C</i> | <i>Model D1</i> | <i>Model D2</i> | <i>Model D3</i> |
|--|----------------|----------------|----------------|-----------------|-----------------|-----------------|
| <i>Mean Slip (m)</i> | 3.6 | 3.75 | 3.6 | 3.9 | 3.9 | 3.8 |
| <i>Median G_c $10^6 (J/m^2)$</i> | 4.1 | 5.1 | 5 | 5.6 | 5.7 | 5.7 |

6.4 Strong-Ground Motion Simulation

The choice of the station distribution (Figure 6-1) was motivated by the need to simulate strong-ground motion in the near-fault region ($R < 10$ km), where the sparsity of recordings affects the reliability of current attenuation laws, and at intermediate to large distances, where the density of available recordings allows model validation.

6.4.1 Comparisons with Empirical Response Spectral Acceleration Models

The main purpose of this study is to determine what degree of complexity we need to include in source characterizations to improve strong-ground motion prediction with respect to traditional kinematic approaches. We demonstrate the advantages of a dynamically consistent source characterization over a simple kinematic approach by comparing the respective horizontal simulated- and empirical-response spectra (5% damped) for rock sites using the Abrahamson and Silva (1997) model for strike-slip earthquakes of M_w 7. Corresponding to each dynamic model, we developed two kinematic source characterizations: the first one based on a *hybrid* kinematic-dynamic parameterization, and the second one based on a simple *kinematic* parameterization. For both parameterizations, we assign the original *kinematic* slip distribution and a box-car SVF with a rise time of 1 sec over the entire fault plane. The *hybrid* parameterization includes the variability in the rupture times derived from the respective dynamic model, while in the *kinematic* model the rupture propagates at a uniform rupture velocity equal to

85% of the local shear speed. Table 6.2 summarizes the types of parameterizations and parameter values of the three modeling approaches.

TABLE 6.2 – Summary of Modeling Approaches

| | <i>Dynamic</i> | <i>Hybrid</i> | <i>Kinematic</i> |
|---|-------------------------------|-------------------------------|-------------------------------|
| <i>Slip</i> | 'dynamic' | 'kinematic' | 'kinematic' |
| <i>Rupture Velocity, v</i> | Variable | Variable (from dynamic model) | Uniform $v = 85\%$ shear wave |
| <i>Rise Time, T</i> | Variable, Mean(T) = 3 sec | Uniform $T = 1$ sec | Uniform $T = 1$ sec |
| <i>SVF</i> | Variable | Box-car | Box-car |

The empirical relation of Abrahamson and Silva for crustal earthquakes was derived using a worldwide data set of shallow events. However, only very few recordings from M_w 7 earthquakes constrain this relation at short distances from the fault ($R < 10$ km) where we observe the greatest variability in strong ground motions.

Figures 6.8 and 6.9 show the comparisons of empirical and simulated spectral acceleration attenuation at several periods for the three different modeling approaches, *dynamic*, *hybrid*, and *kinematic*. In Figure 6.8, for each approach we plot the geometric mean of the two simulated horizontal components of spectral acceleration for all slip models and at all stations without including those aligned along the fault strike (stations 16-30). These locations are along a nodal plane where only the fault-normal component of motion is different from zero (shown in Figure 6.9). In general, the simulations from the *kinematic* approach underperform those obtained from the *dynamic* and *hybrid* modeling. At short periods ($T = 0.7$ s) all the simulated spectral accelerations are depleted in high frequency with respect to the empirical values. This might be due to the relatively coarse model discretization and the limited frequency band of the Green's functions used in our ground motion simulation. In general, the *hybrid* model predicts larger spectral acceleration amplitudes with respect to the other two approaches, especially in the very near-fault region. While these larger amplitudes correspond to a better agreement with the empirical relation at short periods, they overestimate the long-period values. The dynamic simulations overall follow the slope of the empirical relation better than both the kinematic and hybrid approaches, especially at intermediate

distances, where sufficient data exist to provide adequate constraints for the empirical relation. Notice the larger spread of the spectral values at 1 km from the fault in the dynamic simulations compared to the respective hybrid and kinematic results. Although all the along-fault stations 46 to 51 have a closest distance to the fault of 1 km, we should expect strong variability in the ground motions among these locations, where the effects of fault-finiteness and source complexity are the largest. Because the empirical relations are poorly constrained at such distance to large-magnitude earthquakes, it is difficult to determine whether the dynamic simulations are more realistic than the hybrid ones.

6.4.4.1 Directivity Effects

In the near-fault region, the ground motions are strongest on the fault-normal component of motion. This results from rupture directivity effects due to the coherency of SH radiation along the fault rupture generating a large, long-period pulse of motion in the direction perpendicular to the fault (Archuleta and Hartzell, 1981; Somerville *et al.*, 1997). This focusing of energy is maximized at the stations aligned along the strike (16-30), where the SH radiation pattern is at its maximum. Forward directivity effects occur when the rupture front propagates toward the site, and the direction of slip is aligned with the site. Therefore, among our models, we should expect Model D3 to result in the smallest forward directivity effects at the nodal stations.

In Figure 6.9 we show the fault normal horizontal component of spectral accelerations calculated at the nodal stations 16-30 for various periods. The values simulated from the three models D1, D2, and D3 are plotted with different symbols to compare the variations of directivity effects. At all periods, the dynamic simulations capture the variability of directivity effects among the models having different hypocenter positions, showing that Model D3 (diamonds) result in the smallest amplitudes, especially in the very near-source region. Surprisingly, the hybrid simulations show these systematic differences only at larger distances ($R > 10\text{km}$), while the analysis of the kinematic results does not reveal any substantial difference among the different models. The comparison with the empirical relation is not straightforward, because these fault-normal component amplitudes are not averaged values as those shown in Figure 6.8. Nevertheless, we

notice that the fall-off of the empirical relation is matched by both the dynamic and hybrid simulated values at intermediate-large distances.

6.5 Discussion

The comparison between the three modeling approaches allows us to infer how specific source characteristics affect the predicted response at various periods. The systematic large spectral amplitude of kinematic and hybrid simulated responses at long periods reflect the strong coherency of energy release as the rupture propagates along the fault. It has been noticed that kinematic simulations of strong ground motion with very smooth slip distributions tend to overestimate the spectral amplitudes at long periods (> 2 s) in the near-source region (e.g. Olsen *et al.*, 1995). Graves (1998) discusses how uniform or smoothly varying slip distributions greatly increase the coherency of long-period energy release during fault rupture and therefore the calculated ground-motion amplitudes. Nevertheless, kinematic models with heterogeneous slip distributions and homogeneous rupture velocity still overestimate the long period amplitudes (Graves, 1998; Pitarka *et al.*, 2000). Among our three classes of models, the kinematic models have the largest degree of coherency due to homogeneous rupture velocity and uniform SVF, while the variability in both these parameters in the dynamic models greatly diminishes the coherent energy release during rupture. This is particularly evident in the analysis of directivity effects based on Figure 6.9.

The introduction of spatial and temporal heterogeneity tends to increase peak ground motion amplitudes at short periods. This behavior is manifested in the larger spectral amplitudes simulated from the hybrid and dynamic models with respect to those calculated from the kinematic models at short periods (< 2 s) in the near-source region. Although the dynamic models are the most complex, the hybrid approach results in larger high-frequency responses. We interpret this as a consequence of the spectral characteristics of the SVF assumed in the hybrid models (box-car with a rise time of 1 sec). We checked this by calculating ground motions from the hybrid models assuming a rise time = 2 sec, and observe a systematic decrease especially in the high-frequency amplitudes (Figure 6.10). This also suggests that the SVF obtained from our dynamic

modeling might be too smooth to correctly predict the short-period response. Moreover, many near-source stations are concentrated around epicentral regions, where the radiation is largely affected by long rise-time areas. Guatteri and Spudich (2000) showed that a dynamic model having a short slip-weakening distance is characterized by more peaked SVFs compared to a corresponding model with a longer D_c , which, in turn, results in larger high-frequency ground motion amplitudes. To test this idea, we have computed response spectra from a dynamic model having the same slip, static stress drop and fracture energy distributions as in model B, but with a shorter D_c (about a half of the original value). The comparisons of the simulated response spectra from the long- and short- D_c dynamic models are shown in Figure 6.11. Notice that at a period of 0.7 sec the short D_c model results in systematically larger response spectra amplitudes, especially at the medium-large distances. We can argue that even shorter D_c would result in larger high-frequency amplitudes. Even though it is beyond the scope of this study, these results encourage the analysis of high-frequency spectra to help constrain rupture dynamics.

6.5.1 Implications for Strong-Ground Motion Prediction

This study shows that the inclusion of variability in all the relevant source parameters, such as slip, rupture velocity and SVF, may reduce the occurrence of systematic differences between the simulated ground motions and the empirical values at various periods. The improvement provided by the inclusion of heterogeneity in the rupture velocity is evident from the comparison between the hybrid and kinematic simulations. Variability in the rupture time distribution may be included in kinematic models through a generalization of Andrews' result relating rupture speed to apparent fracture energy, stress drop, and crack length. The additional effects of variable SVF in the dynamic models are subtler and probably less evident due to our specific choice of rise time values in the kinematic and hybrid parameterizations. Figure 6.7 suggests that the assumption that a box-car describes the time dependence of slip after rupture is inadequate to realistically characterize the fault behavior. A truncated Kostrov function (e.g. Beroza and Spudich, 1988), overlapping triangles (e.g. Wald *et al.*, 1991), or a cosine slip function (Cotton and Campillo, 1995) better describe the fault particle motion

of a complex source. Furthermore, because both the slip rise time and SVF are not very well constrained in deterministic waveform modeling (e.g. Cotton and Campillo, 1995), non uniform rise time distributions would reduce the bias in the spectral content of simulated ground motions. The empirical relation between slip rise time and magnitude proposed by Somerville *et al.* (1998) determines a median rise time of about 1.5 s for a M_w 7 earthquake. Our results suggest that this value might be appropriate for the median value of a spatially variable width of the slip velocity function pulse (Figure 6.7).

The results of this study can be applied to develop more physically constrained kinematic source models for deterministic near-fault strong ground motion simulations. A more realistic and robust characterization of the rupture process, in combination with stochastic high-frequency simulations, has the potential to improve the modeling of near-fault ground motions. More realistic source characterization of scenario earthquakes should lead to more realistic ground-motion time histories, which in turn should improve our ability to predict the dynamic response of structures to near-fault ground motions.

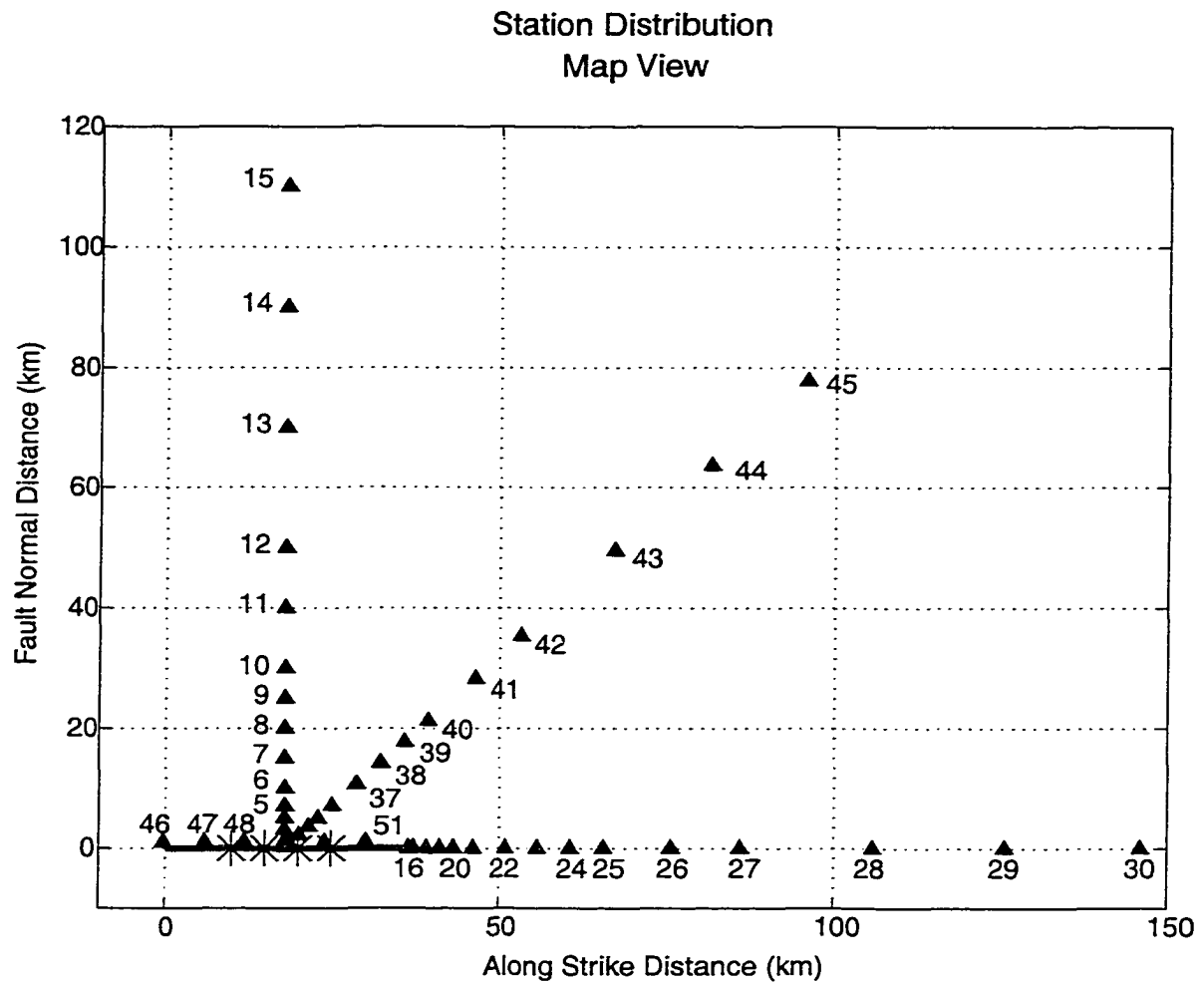


Figure 6.1. Fault and receiver locations. Stars indicate the hypocenters for the six different rupture models. The triangles indicate the locations of receivers.

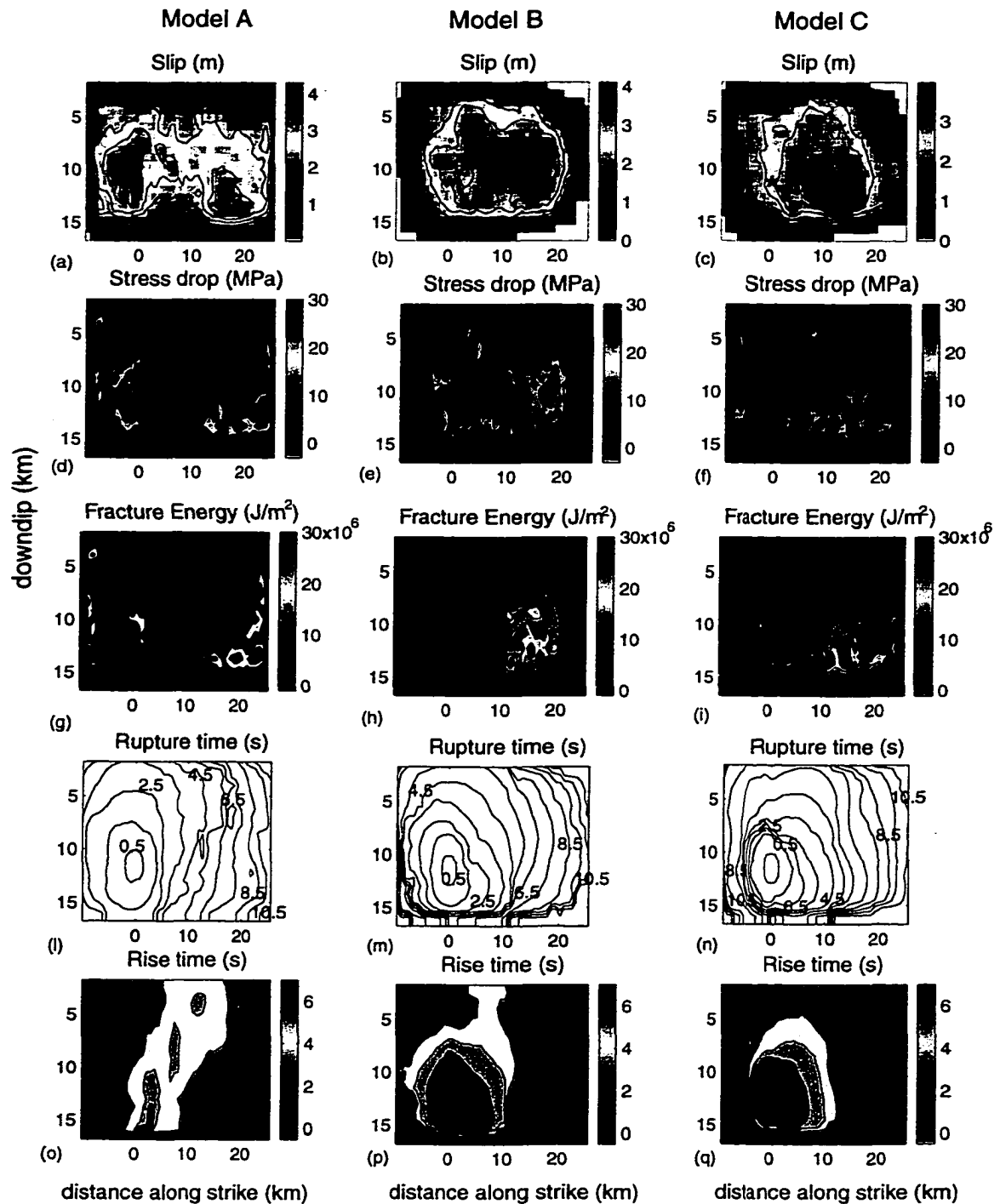


Figure 6.2. Distribution of kinematic and dynamic parameters on the fault plane (the star indicates the hypocenter location) for models A, B and C. Dynamic slip distribution (a), (b), and (c); static stress drop distribution (d), (e), and (f); fracture energy distribution (g), (h), and (i); rupture time distribution (l), (m), and (n); rise time distribution (o), (p), and (q). The static stress drop distributions are derived from slip realizations (kinematic slip) generated following the random-field model from Mai and Beroza (1999). The fracture energy distributions are prescribed by *trial and error* to obtain a subshear rupture speed. The dynamic slip, the rupture time and the rise time distributions are derived from our dynamic simulations.

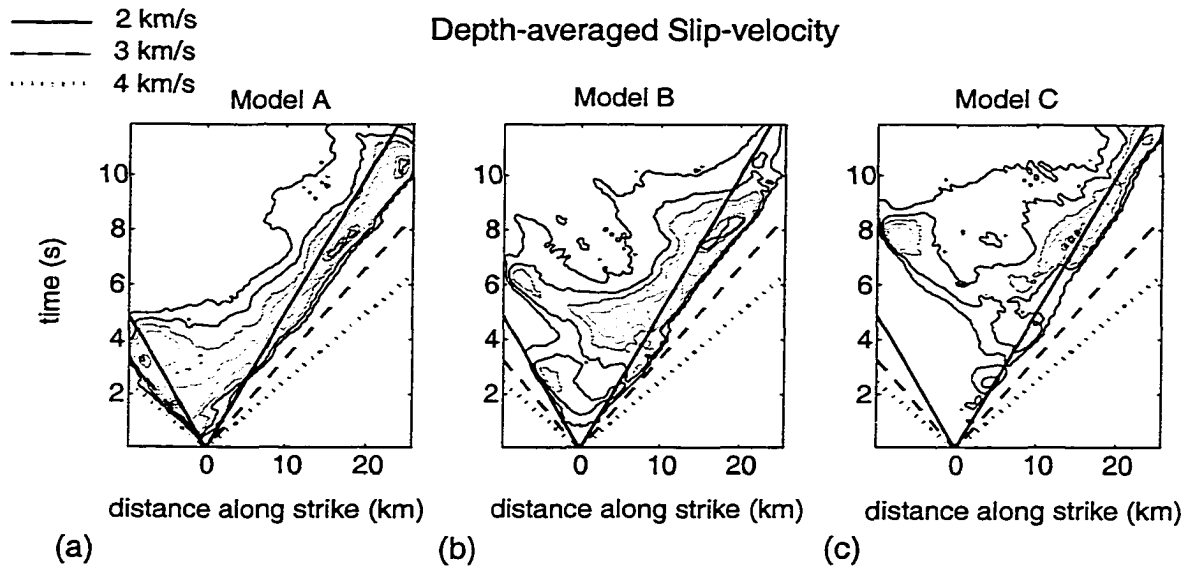


Figure 6.3. Contours of depth-averaged slip velocity as function of distance along strike and time for models A, B and C. The three reference lines have slopes corresponding to rupture speeds of 2 km/s, 3 km/s, and 4 km/s. The average slope of the contours are representative of the average rupture velocity.

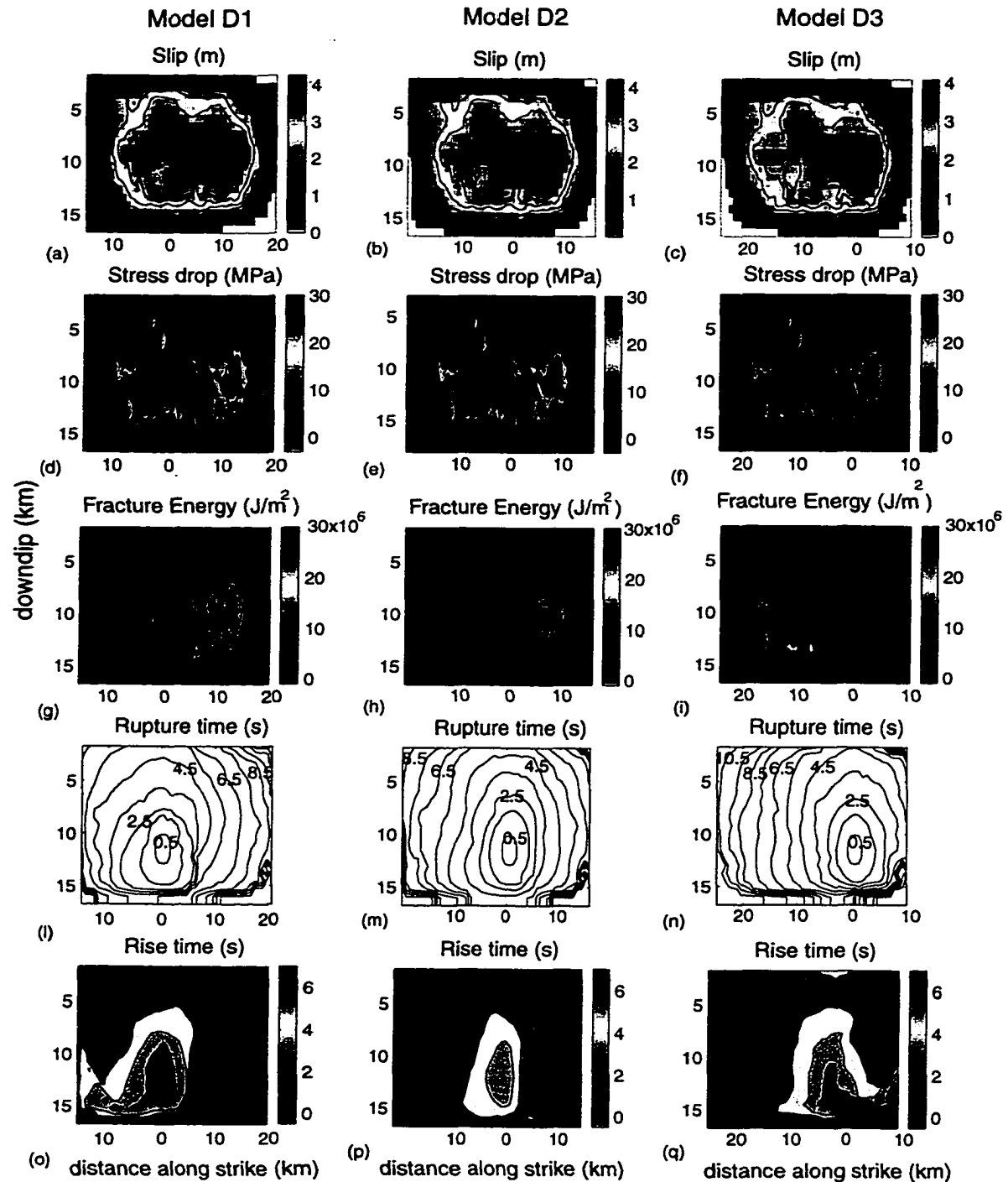


Figure 6.4. Same as Figure 6.2 for models D1, D2 and D3. For these three models, the static stress drop distribution is the same as for model B. The stars indicate the hypocenter locations for the three models: at 15 km, 20 km, 25 km from the left boundary of the fault at 11 km depth, respectively.

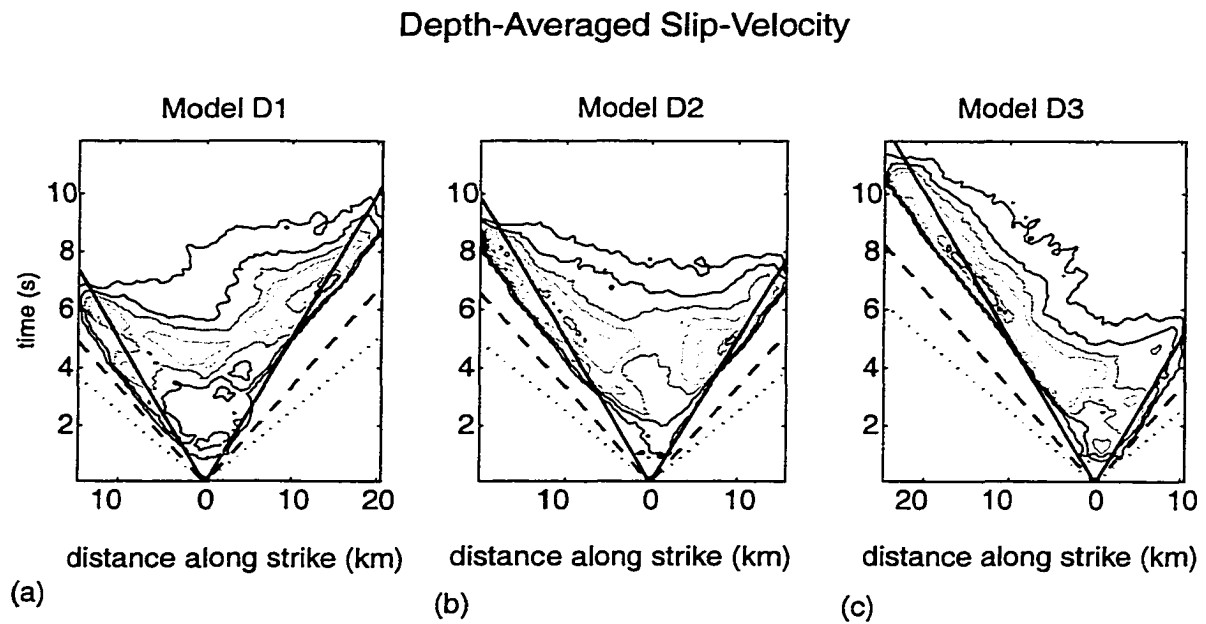


Figure 6.5. Same as Figure 6.3 for models D1, D2 and D3. Note the different hypocenter location along strike.

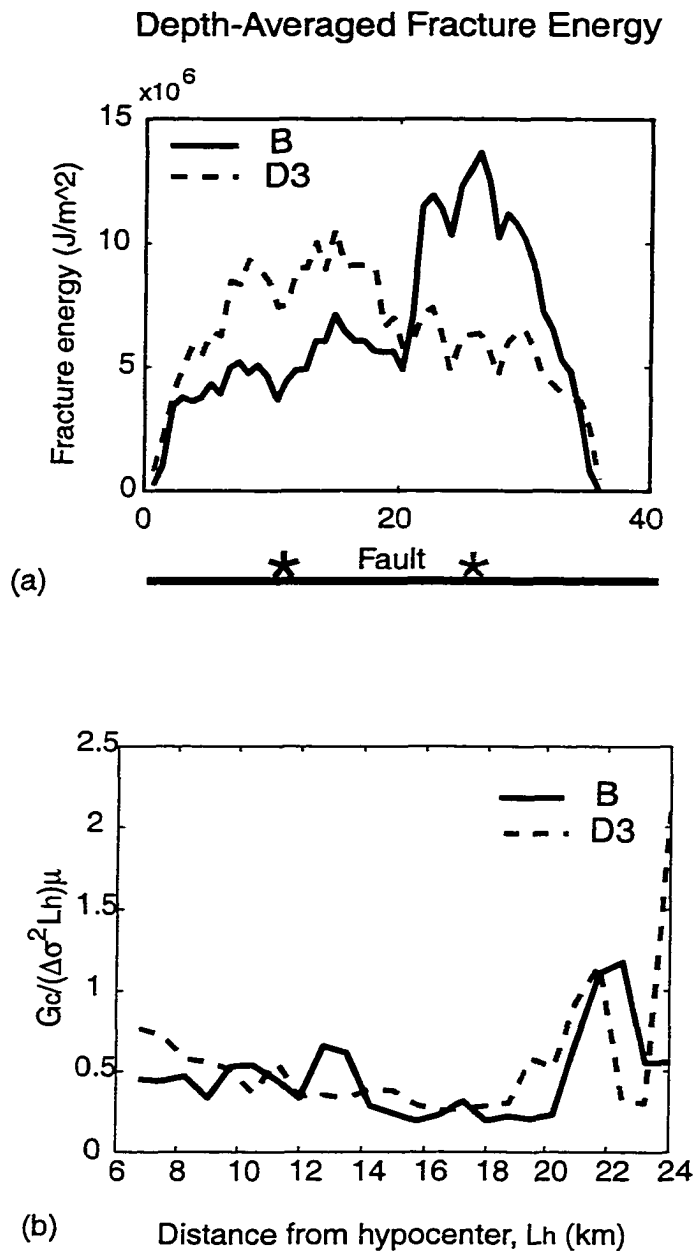


Figure 6.6. (a) Depth-averaged fracture energy for model B (continuous line) and model D3 (dashed line). The models have the same stress drop and slip distributions but different hypocenter locations (indicated by the stars). Relatively large values of fracture energy are present where it is necessary to slow down rupture propagation. (b) Dimensionless parameter dependent on fracture energy, stress drop, and crack length that controls the value of rupture velocity for a simple antiplane strain with uniform stress drop (Andrews, 1976a). The similarity between the values calculated for model B and model D3 suggests that this parameter may still control rupture speed in a 3-D heterogeneous dynamic model.

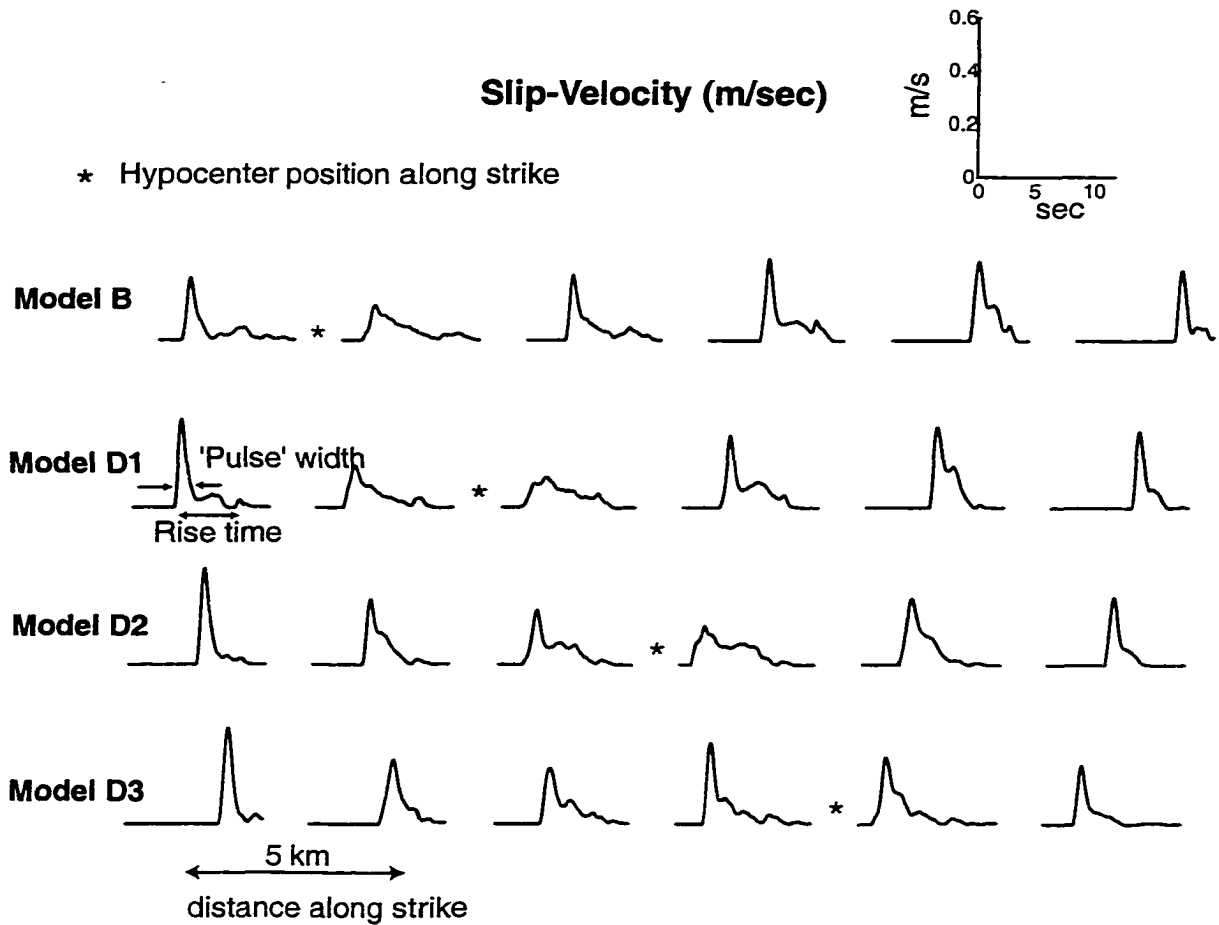


Figure 6.7. Slip-velocity histories (or source-time functions) obtained from the dynamic simulations of models B, D1, D2 and D3 (having the same slip distributions) at different positions along the strike of the fault and at a depth of 7 km. The source-time functions for the four models correspond to the same position on the fault, and the stars indicate the hypocenter location along the strike for the respective model. Notice how, at a given point on the fault, the relative distance from the hypocenter affects the shape of the local slip-velocity.

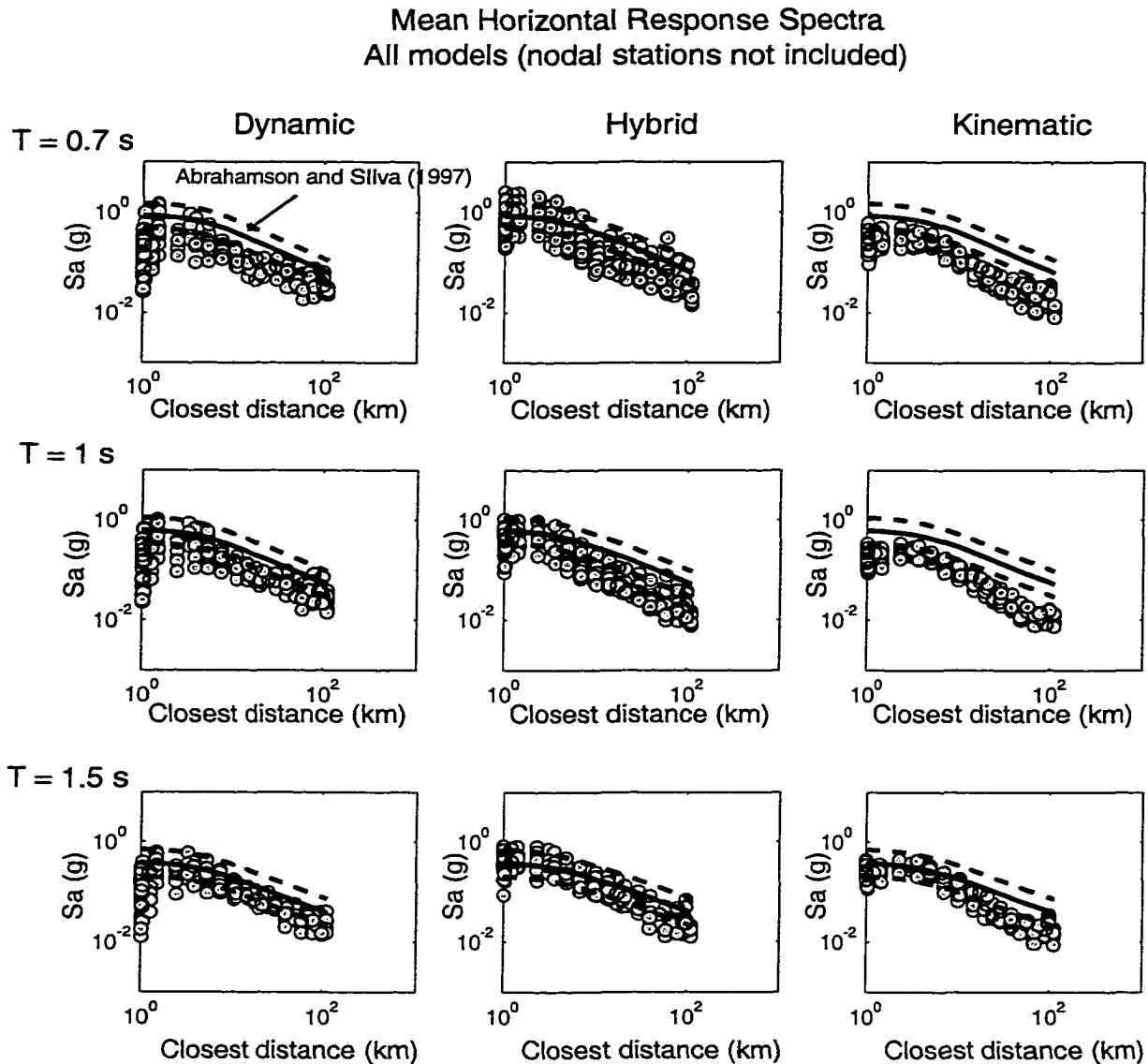


Figure 6.8a. Comparison of simulated (circles) and empirical average horizontal spectral acceleration attenuation (solid line) of Abrahamson and Silva (1997) for a M 7 strike-slip earthquake. Dashed line is the standard deviation of the empirical attenuation. The dynamic simulated values were obtained using the dynamic models A, B and C shown in Figure 6-2, and models D1, D2 and D3 shown in Figure 6.4; the hybrid and kinematic simulations were obtained as explained in Table 6.2. The spectral acceleration for the nodal stations (16-30 in Figure 6.1) is not shown here.

Mean Horizontal Response Spectra
All models (nodal stations not included)

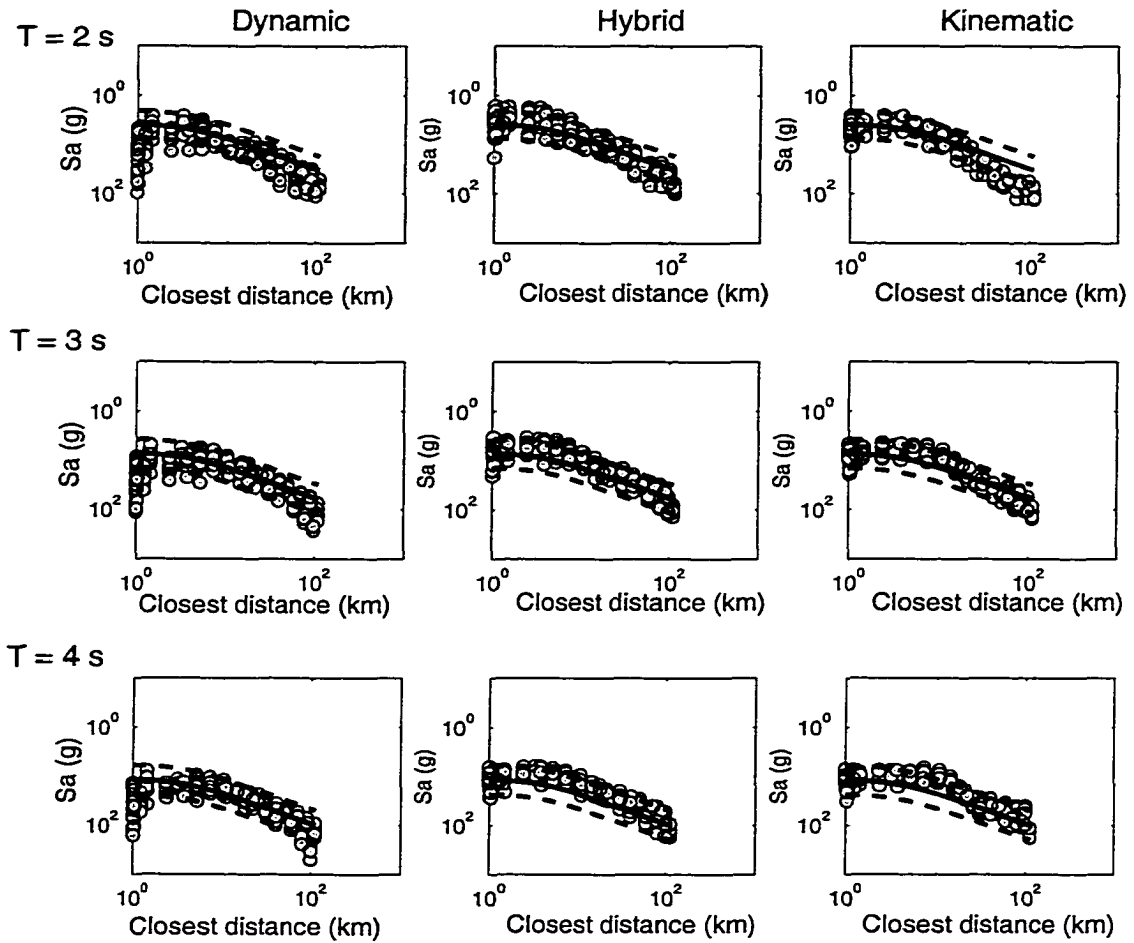


Figure 6-8b. See caption of Figure 6.8a.

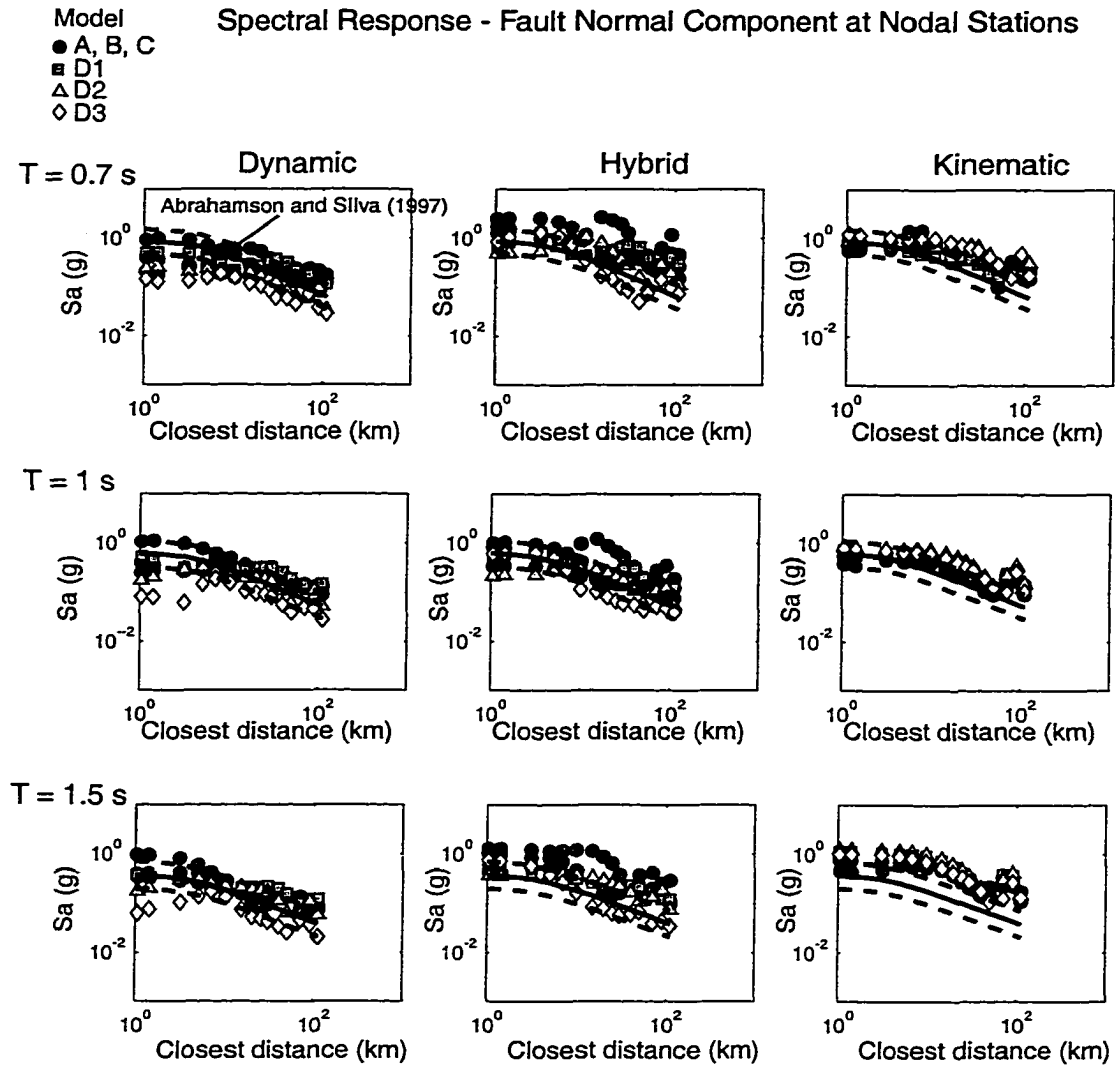


Figure 6.9a. Comparison of simulated fault-normal horizontal component (circles) and empirical attenuation (solid line) of Abrahamson and Silva (1997) for a M 7 strike-slip earthquake. Only the simulated values at the nodal stations 16-30, for which the directivity effects are the largest, are shown.

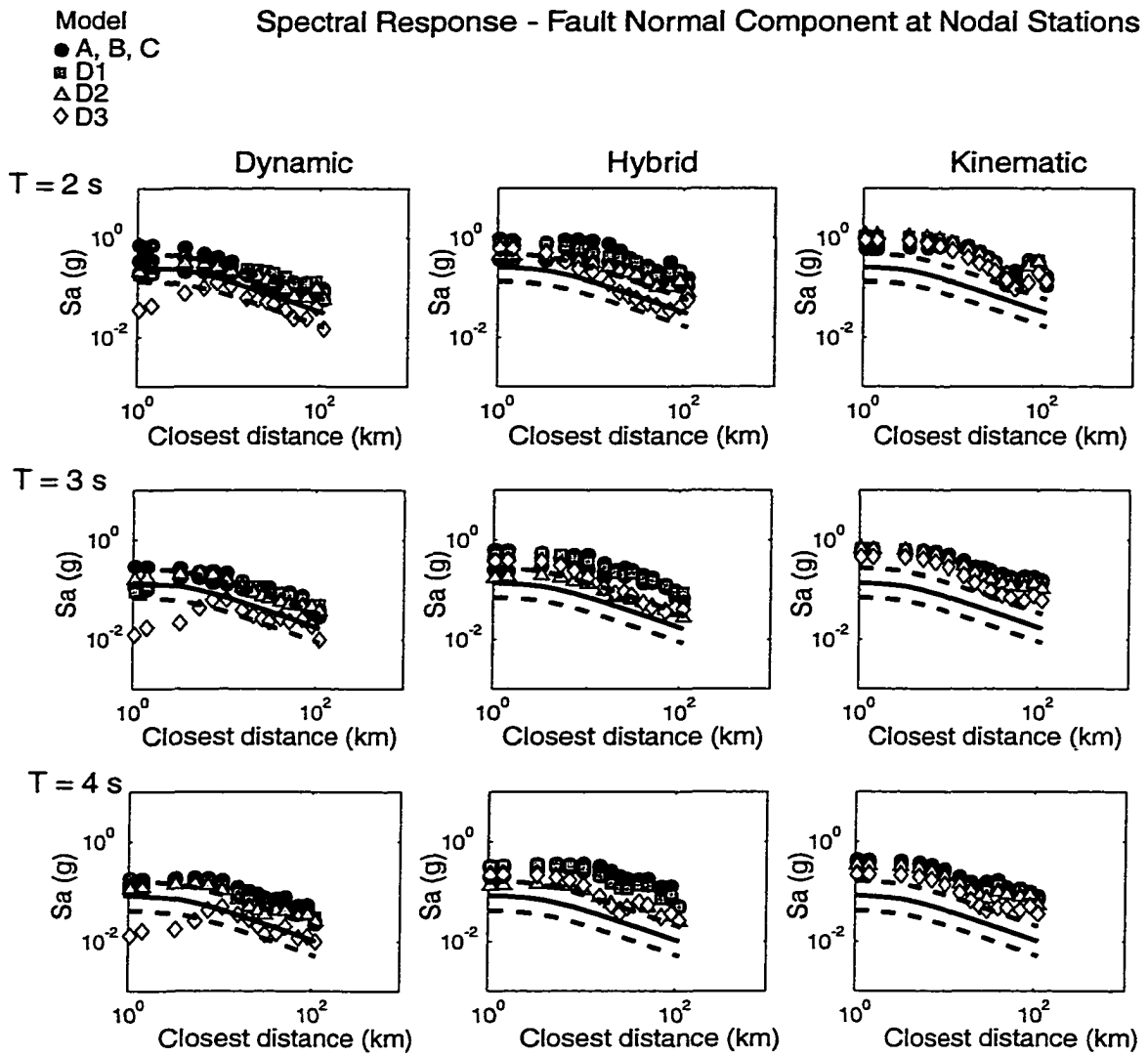


Figure 6.9b. See caption for Figure 6.9a.

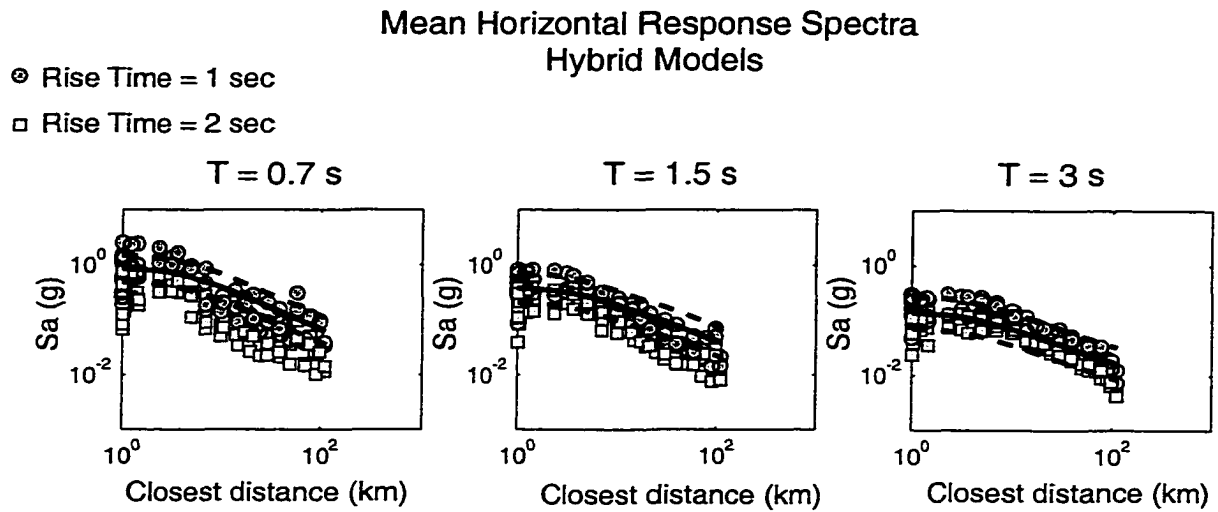


Figure 6.10. Effect of a longer rise time. Comparison of empirical average horizontal spectral acceleration attenuation (solid line) of Abrahamson and Silva (1997) for a M 7 strike-slip earthquake with simulated values from hybrid models with a rise time of 1 sec (circles) and 2 sec (squares). Only the non-nodal stations are shown. The amplitudes of the 2 sec models are systematically lower than those of the 1 sec models.

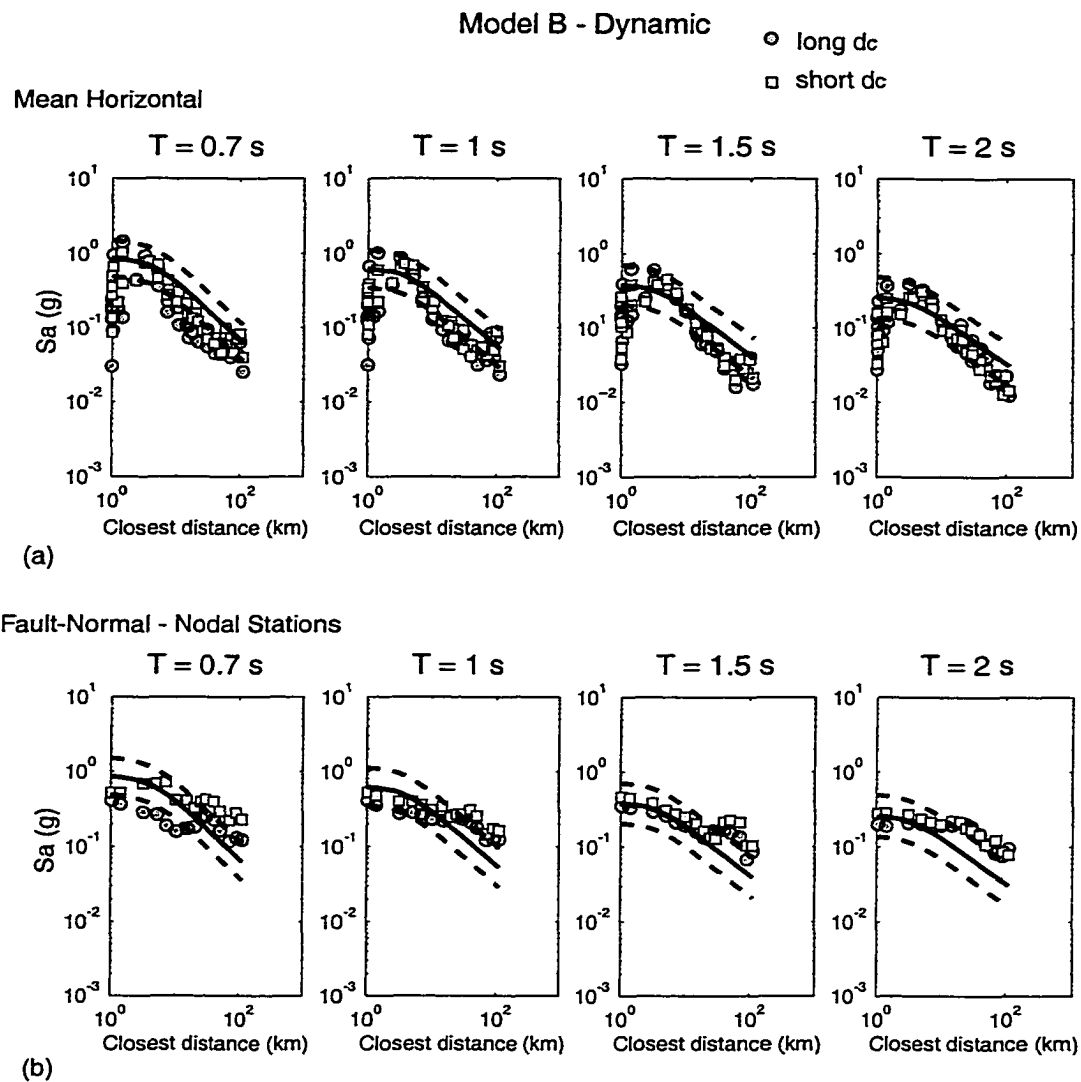


Figure 6.11. Effect of a shorter slip-weakening distance (d_c). (a) Comparison of empirical average horizontal spectral acceleration attenuation (solid line) of Abrahamson and Silva (1997) for a M 7 strike-slip earthquake with simulated values from the dynamic model B as shown in Figure 6-8 (circles) and with a shorter d_c (squares). (b) Same as (a) for the fault-normal component at the nodal stations.

References

- Abrahamson, N. A. and W. J. Silva (1997). Empirical response spectral attenuation relations for shallow crustal earthquakes, *Seism. Res. Lett.* **68**, 94-128.
- Aki, K. (1979). Characterization of barriers on an earthquake fault, *J. Geophys. Res.*, **73**, 5359-5376.
- Aki, K. (1987). Magnitude-frequency relation for small earthquakes: a clue to the origin of f_{max} of large earthquakes, *J. Geophys. Res.*, **92**, 1349-1355.
- Aki, K., and P.G. Richards (1980). *Quantitative Seismology*, W.H. Freeman, San Francisco.
- Andrews, D.J. (1976a). Rupture propagation with finite stress in antiplane strain, *J. Geophys. Res.*, **81**, 3575-3582.
- Andrews, D.J. (1976b). Rupture velocity of plane strain shear cracks, *J. Geophys. Res.*, **81**, 5679-5687.
- Andrews, D.J. (1980). Fault impedance and earthquake energy in the Fourier transform domain, *Bull. Seismol. Soc. Am.*, **70**, 1683-1698.
- Andrews, D.J. (1994). Dynamic growth of mixed mode shear cracks, *Bull. Seismol. Soc. Am.*, **84**, 1184-1198.
- Andrews, D.J. (1985). Dynamic plane-strain shear rupture with a slip-weakening friction law calculated by a boundary integral method, *Bull. Seismol. Soc. Am.*, **75**, 1-21.
- Andrews, D.J., Y. Ben-Zion (1997). Wrinkle-like slip pulse on a fault between different materials, *J. Geophys. Res.*, **102**, 553-571.
- Andrews, D. J., J. Boatwright (1998). Dynamic simulations of spontaneous rupture with heterogeneous stress drop, *Seism. Res. Lett.* **69**, 142.
- Angelier, J. (1984). Tectonic analysis of fault slip data, *J. Geophys. Res.*, **89**, 5835-5848.
- Angelier, J., A. Tarantola, B. Valette, and S. Manoussis (1982). Inversion of field data infault tectonics to obtain the regional stress – 1. Single phase fault populations: a new method of computing the stress tensor, *Geophys. J. R. Astr. Soc.* **69**, 607-621.

- Aochi, H. and M. Matsu'ura (1998). Slip- and time-dependent fault constitutive law and its significance in earthquake generation cycles (1999). *Geophys. J. R. Astr. Soc.*, submitted.
- Archuleta, R. J. (1982). Hypocenter for the 1979 Imperial Valley earthquake, *Geophys. Res., Lett.*, **9**, 625-628
- Archuleta, R. J. (1984). A faulting model for the 1979 Imperial Valley earthquake, *J. Geophys. Res.*, **89**, 4559-4585.
- Arculeta, R.J. and S. Day (1980). Dynamic rupture in a layered medium: the 1966 Parkfield earthquake, *Bull. Seismol. Soc. Am.*, **70**, 671-689.
- Arculeta, R.J. and G. Frazier (1978). Three-dimensional numerical simulations of dynamic faulting in a half-space, *Bull. Seismol. Soc. Am.*, **68**, 541-572.
- Árnadóttir, T., and P. Segall (1994). The 1989 Loma Prieta earthquake imaged from inversion of geodetic data, *J. Geophys. Res.*, **99**, 21835-21,855.
- Awata, Y., K. Mizuno, Y. Sugiyama, R. Imura, K. Shimokawa, K. Okumura, E. Tsukuda, and K. Kimura (1996). Surface fault ruptures on the northwest coast of Awaji Island associated with the Hyogoken Nanbu earthquake of 1995, Japan, *J. Seismol. Soc. Japan*, **49**, 113-124.
- Barenblatt, G.I. (1959). The formation of equilibrium cracks during brittle fracture: general ideas and hypotheses, *J. Appl. Math. Mech.*, **23**, 622-636.
- Beeler, N.M., T.E. Tullis, M.L. Blanpied, and J.D. Weeks (1996). Frictional behavior of large displacement experimental faults, *J. Geophys. Res.*, **101**, 8697-8715.
- Belardinelli, M.E., M. Cocco, O. Coutant, and F. Cotton (1999). Redistribution of dynamic stress during coseismic ruptures: evidence for fault interaction and earthquake triggering, *J. Geophys. Res.*, **104**, 14,925-14,945.
- Ben-Zion, Y., and J.R. Rice (1997). Dynamic simulations of slip on a smooth fault in an elastic solid, *J. Geophys. Res.*, **102**, 17771-17784.

- Bernard, P., A. Herrero, and C. berge (1996). Modeling directivity of heterogeneous earthquake ruptures, *Bull. Seism. Soc. Am.* **86**, 1149-1160.
- Beroza, G.C. (1991). Near source modeling of the Loma Prieta earthquake: Evidence for heterogeneous slip and implications for earthquake hazard, *Bull. Seismol. Soc. Am.*, **81**, 1603-1621.
- Beroza, G.C. and T. Mikumo (1996). Short slip duration in dynamic rupture models in the presence of heterogeneous fault properties, *J. Geophys. Res.*, **101**, 22449-22460.
- Beroza, G. C. and P. Spudich (1988),. Linearized inversion for fault rupture behavior: application to the 1984 Morgan Hill, California earthquake, *J. Geophys. Res.*, **93**, 6275-6296.
- Beroza, G. C., and M. D. Zoback (1993). Mechanism diversity of the Loma Prieta aftershocks and the mechanics of mainshock-aftershock interaction, *Science*, **259**, 210-213.
- Blanpied, M.L., D.A. Lockner, and J. D. Byerlee (1995). Frictional slip of granite at hydrothermal conditions, *J. Geophys. Res.*, **100**, 13,045-13,064.
- Blanpied, M.L., T.E. Tullis, and J.D. Weeks (1998). Effects of slip, slip rate, and shear heating on the friction of granite, *J. Geophys. Res.*, **103**, 489-511.
- Boatwright, J., and M. Cocco (1996). Frictional constraints on crustal faulting, *J. Geophys. Res.*, **101**, 13895-13909.
- Boatwright, J. and H. R. Quin (1986). The seismic radiation from a 3-D dynamic model of a complex rupture process. Part 1. Confined rupture, in *Earthquake Source Mechanism*, S. Das, J. Boatwright, and C. Scholz, Editors, American Geophysical Union, Washington, D. C.
- Bouchon, M. (1997). The state of stress on some faults of the San Andreas system as inferred from near-field strong motion data, *J. Geophys. Res.*, **102**, 11731-11744.
- Bouchon, M., and D. Streiff (1997). Propagation of a shear crack on a nonplanar fault: A method of calculation, *Bull. Seismol. Soc. Am.*, **87**, 61-66.
- Boore, D. M., and W. B. Joyner (1997). Site amplifications for generic rock sites. *Bull. Seism. Soc. Am.* **87**, 327-341.

- Boore, D. M., W. B. Joyner, and T. E. Fumal (1997). Equations for estimating horizontal response spectra and peak acceleration from Western North American earthquakes: a summary of recent work, *Seism. Res. Lett.* **68**, 128-153.
- Brune, J. N. (1970). Tectonic stress and the spectra of seismic shear waves from earthquakes, *J. Geophys. Res.*, **75**, 4997-5009.
- Brune, J. N., T. L. Henvey, and R. F. Fox (1969). Heat flow, stress, and rate of slip along the San Andreas fault, California, *J. Geophys. Res.*, **74**, 3821-3827.
- Byerlee, J.D. (1990). Friction, overpressure, and fault normal compression, *Geophys. Res. Lett.*, **17**, 2109-2112.
- Byerlee, J.D. (1993). Model for episodic flow of high-pressure water in fault zones before earthquakes, *Geology*, **21**, 303-306.
- Cohee, B. P. and G. C. Beroza (1994). Slip distribution of the 1992 Landers earthquake and its implications for earthquake source mechanics. *Bull. Seismol. Soc. Am.*, **84**, 692-712.
- Cotton, F. and M. Campillo (1995). Frequency domain inversion of strong motions: application to the 1992 Landers earthquake, *J. Geophys. Res.*, **100**, 3961-3975.
- Das, S. (1981). Three-dimensional spontaneous rupture propagation and implications for the earthquake source mechanics, *Geophys. J. R. Astr. Soc.*, **67**, 375-393.
- Das, S., and K. Aki (1977). Fault planes with barriers: A versatile earthquake model, *J. Geophys. Res.*, **82**, 5648-5670.
- Das, S. and B. V. Kostrov (1987). On the numerical boundary integral equation method for three-dimension dynamic shear crack problems, *J. Appl. Mech.*, **54**, 99-104.
- Das, S. and B. V. Kostrov (1990). Inversion for seismic slip rate and distribution with stabilising constraints: application to the 1986 Anreanof Islands earthquake, *J. Geophys. Res.*, **95**, 6899-6913.
- Day, S.M. (1982). Three-dimensional simulation of spontaneous rupture: the effect of nonuniform prestress, *Bull. Seismol. Soc. Am.*, **72**, 1881-1902.

- Day, S.M., G. Yu, and D. Wald (1998). Dynamic stress changes during earthquake rupture, *Bull. Seismol. Soc. Am.*, **88**, 512-522.
- Dieterich, J. H. (1978). Time dependent friction and the mechanics of stick-slip, *Pure Appl. Geophys.*, **116**, 790-806.
- Dieterich, J. H. (1979). Modeling of rock friction - 1. experimental results and constitutive equations, *J. Geophys. Res.*, **84**, 2169-2175.
- Dieterich, J.H. (1981). Constitutive properties of faults with simulated gouge, in *Mechanical Behavior of Crustal Rocks, Geophys. Monogr. Ser.*, vol. 24, edited by N.L.Carter, M. Friedman, J.M.Logan, and D.W.Stearns, pp.102-120, AGU, Washington, D.C.
- Dieterich, J.H. (1986). A model for the nucleation of earthquake slip, in *Earthquake Source Mechanics, Geophys. Monogr. Ser.*, vol. 37, edited by S. Das, J. Boatwright, and C.H. Scholz, pp.37-47, AGU, Washington, D.C.
- Dieterich, J.H. (1987). Nucleation and triggering of earthquake slip: Effect of periodic stresses, *Tectonophysics*, **144**, 127-139.
- Dieterich, J.H. (1994). A constitutive law for rate of earthquake production and its application to earthquake clustering, *J. Geophys. Res.*, **99**, 2601-2618.
- Dieterich, J.H., and B.D. Kilgore (1994). Direct observation of frictional contacts; New insights for state-dependent properties, *Pure and Applied Geophysics*, **143**, 283-302.
- Dieterich, J.H., and B. Kilgore (1996a). Implications of fault constitutive properties for earthquake prediction, *Proc. Natl. Acad. Sci. USA*, **93**, 3787-3794.
- Dieterich, J.H., and B.D. Kilgore (1996b). Imaging surface contacts; power law contact distributions and contact stresses in quartz, calcite, glass and acrylic plastic, *Tectonophysics*, **256**, 219-239.
- Etchecopar, A., G. Vasseur, and M. Daignieres (1981). An inverse problem in microtectonics for the determination of stress tensors from fault striation analysis, *J. Struct. Geol.*, **3**, 51-65.

- Florensov, N.A., and V.P. Solonenko (1965). The Gobi-Altai Earthquake, Academy of Sciences of the USSR, Siberian Dept., available from U.S. Dept. of Commerce, Springfield, VA, 424 pp.
- Fuis, G. S., W. Mooney, J. Healy, G. McMechan, and W. Lutter (1984). A seismic refraction survey of the Imperial Valley region, California, *J. Geophys. Res.*, **89**, 1165-1189.
- Fukuyama, E., and T. Mikumo (1993). Dynamic rupture analysis: inversion for the source process of the 1990 Izu Oshima, Japan earthquake (M6.5), *J. Geophys. Res.*, **88**, 2191-2198.
- Graves, R. W. (1998). Three-dimensional finite-difference modeling of the San Andreas fault: source parameterization and ground-motion levels, *Bull. Seism. Soc. Am.* **88**, 881-897.
- Guatteri, M., and M. Cocco (1996). On the variation of slip direction during earthquake rupture: Supporting and conflicting evidence from the 1989 Loma Prieta earthquake, *Bull. Seismol. Soc. Am.*, **86**, 1935-1951.
- Guatteri, M., and P. Spudich (1996). Inversion of earthquake ground motions to determine fault constitutive relations, XXI meeting of the European Geophysical Society, The Hague.
- Guatteri, M., and P. Spudich (1998). Coseismic changes of slip direction: the effect of absolute stress on dynamic rupture, *Bull. Seismol. Soc. Am.*, **88**, 777-789.
- Guatteri, M., and P. Spudich (2000). What can strong motion data tell us about slip-weakening fault-friction laws?, *Bull. Seismol. Soc. Am.*, **90**, 98-116.
- Guatteri, M., P. Spudich, and G. C. Beroza (2001). Inferring rate and state friction parameters from a rupture model of the 1995 Hyogo-ken Nanbu (Kobe) earthquake, *J. Geophys. Res.*, in press.
- Hanks, T. C. (1982). f_{\max} , *Bull. Seismol. Soc. Am.*, **72**, 1867-1880.
- Harris, R. A., R. J. Archuleta, and S. M. Day (1991). Fault steps and the dynamic rupture process: 2-D numerical simulations of a spontaneously propagating shear fracture, *Geophys. Res. Lett.*, **18**, 893-896.
- Harris, R. A., and S. M. Day (1993). Dynamics of fault interaction: parallel strike-slip faults, *J. Geophys. Res.*, **98**, 4461-4472.

- Harris, R.A., and R. W. Simpson (1998). Suppression of large earthquakes by stress shadows: A comparison of Coulomb and rate-and-state failure, *J. Geophys. Res.*, **103**, 24439-24451.
- Hartzell, S. H. (1989). Comparison of seismic waveform inversion results for the rupture history of a finite fault; application to the 1986 North Palm Springs, California, earthquake, *J. Geophys. Res.*, **94**, 7515-7534.
- Hartzell, S. H., and T.H. Heaton (1983). Inversion of strong ground motion and teleseismic waveform data for the fault rupture history of the 1979 Imperial Valley, California, earthquake, *Bull. Seismol. Soc. Am.*, **73**, 1553-1583.
- Hartzell, S., P. Liu, and C. Mendoza (1996). The 1994 Northridge, California earthquake: investigation of rupture velocity, risetime, and high frequency radiation, *J. Geophys. Res.* **101**, 20091-20108.
- Hartzell, S., S. Harmsen, A. Frankel, and S. Larsen (1999). Calculation of broadband time histories of ground motion: comparison of methods and validation using strong-ground motion from the 1994 Northridge earthquake, *Bull. Seism. Soc. Am.* **89**, 1484-1504.
- Haskell, N. (1964). Total energy and energy spectral density of elastic wave radiation from propagating faults, *Bull. Seismol. Soc. Am.*, **54**, 1811-1842.
- Heaton, T.H. (1982). Tidal triggering of earthquakes. *Bull. Seismol. Soc. Am.*, **72**, 2181-2200.
- Heaton, T.H. (1990). Evidence for and implications of self-healing pulses of slip in earthquake rupture, *Phys. Earth Planet. Inter.*, **64**, 1-29.
- Herrero, A., and P. Bernard (1994). Akinematic self-similar rupture process for earthquake, *Bull. Seism. Soc. Am.* **84**, 1216-1228.
- Hisada, Y. (2000). A theoretical omega-square model considering the spatial variation in slip and rupture velocity, *Bull. Seism. Soc. Am.* **90**, 387-400.
- Husseini, M. I., D. B. Jovanovich, M. J. Randall and L. B. Freund (1975). The fracture energy of earthquakes, *Geophys. J. R. Astr. Soc.*, **43**, 367-385.
- Ida, Y. (1972). Cohesive force across the tip of a longitudinal shear crack and Griffith's specific surface energy, *J. Geophys. Res.*, **84**, 3796-3805.

- Ida, Y. (1973). The maximum acceleration of seismic ground motion, *Bull. Seismol. Soc. Am.*, **63**, 959-968.
- Ide, S. and M. Takeo (1996). The dynamic rupture process of the 1993 Kushiro-oki earthquake, *J. Geophys. Res.*, **101**, 5661-5675.
- Ide, S., M. Takeo, and Y. Yoshida (1996). Source process of the 1995 Kobe earthquake: Determination of spatio-temporal slip distribution by Bayesian modeling, *Bull. Seismol. Soc. Am.*, **86**, 547-566.
- Ide, S and M. Takeo (1997). Determination of constitutive relations of fault slip based on seismic wave analysis, *J. Geophys. Res.*, **102**, 27379-27391.
- Ikeda, R., Y. Iio, and K. Omura (1996). Active fault zone drilling in the Hanshin-Awaji area: Drilling and in-situ stress measurements at Nojima-Hirabayashi, Iwaya, and Kabutoyama, (in Japanese), *Proc. Symposium of Fault Dissection Project*, Kyoto Univ., December, 1996.
- Ikeda, R., Y. Iio, and K. Omura (1997). Active fault zone drilling in the Hanshin-Awaji area (2): In-situ crustal stress measurements in the three deep boreholes (in Japanese), Japan Earth and Planet. Sci. Joint Meeting, A22-02, March 25-28, 1997.
- Ito, H., Y. Kuwahara, and O. Nishizawa (1997). Stress measurement by the hydraulic fracturing in the 1995 Hyogoken-Nanbu earthquake source region, *Proc. Internat. Symp. on Rock Stress*, Kumamoto, Japan, Oct. 7-10, October 1997.
- Kakimi, T., Y. Kinugasa, Y. Suzuki, K. Kodama, and T. Mitsunashi (1977). Geological research on the Izu-Hanto-oki earthquake of 1974, *Spec. Rept. Geol. Surv. Japan*, No. 6, 35 pp.
- Kamae, K., and K. Irikura (1998). Source model of the 1995 Hyogo-ken Nanbu earthquake and simulation of near-source ground motion, *Bull. Seism. Soc. Am.* **88**, 400-412.
- Kamae, K., K. Irikura, and A. Pitarka (1998). A technique for simulating strong ground motion using Hybrid Green's function, *Bull. Seism. Soc. Am.* **88**, 357-367.
- Kilb, D., M. Ellis, J. Gomberg, and S. Davis (1997). On the origin of diverse aftershock mechanism following the 1989 Loma Prieta earthquake, *Geophys. J. R. Astr. Soc.* **128**, 557-570.

- Lapusta, N. , J.R. Rice, Y. Ben-Zion, and G. Zheng (1999). Elastodynamic analysis for slow tectonic loading with spontaneous rupture episodes on faults with rate- and state-dependent friction, submitted to *J. Geophys. Res.*
- Lockner, D., H. Naka, H. Tanaka, H. Ito, and R. Ikeda (2000). Permeability and strength of core samples from the Nojima fault of the 1995 Kobe earthquake, *U.S.G.S Open File Report 00-129*.
- Luenberger, D. G. (1984). Linear and nonlinear programming, *Addison-Wesley Publishing Co.*, Reading, MA.
- Mai, P. M., and G. C. Beroza (1999). Characterization of complex earthquake slip as a spatial random field, *EOS Transactions, American Geophysical Union* **80**, no. 46, p. 707.
- Mai, P. M., and G. C. Beroza (2000). Source scaling properties from finite-fault-rupture models, *Bull. Seism. Soc. Am.* **90**, 604-615.
- Marone, C.J., C.H. Scholz, and R. Bilham (1991). On the mechanics of earthquake afterslip, *J. Geophys. Res.*, **96**, 8441-8452.
- Marone, C.J., and B.D. Kilgore (1993). Scaling of the critical slip distance for seismic faulting with shear strain in fault zones, *Nature*, **362**, 618-621.
- Mikumo T., and T. Miyatake. (1978). Dynamical rupture process on a three-dimensional fault with non-uniform frictions and near-field seismic waves, *Geophys. J. R. Astr. Soc.*, **54**, 417-438.
- Mikumo, T. and T. Miyatake (1993). Dynamic rupture processes on a dipping fault, and estimates of stress drop and strength excess from the results of waveform inversion. *Geophys. J. Int.*, **112**, 481-496.
- Miyatake, T. (1980). Numerical simulations of earthquake source process by a three-dimensional crack model; Part I, Rupture process, *J. Phys. Earth.* **28**, 565-598.
- Miyatake, T. (1992). Reconstruction of dynamic rupture process of an earthquake with constraints of kinematic parameters, *Geophys. Res. Let.*, **19**, 349-352.
- Nakatani, M. (1997). Experimental study of time-dependent phenomena in frictional faults as a manifestation of stress-dependent thermally activated process, Ph.D. Thesis, University of Tokyo.

- Ohnaka, M., and Y. Kuwahara (1990). Characteristic features of local breakdown near a crack-tip in the transition zone from nucleation to unstable rupture during stick-slip shear failure, *Tectonophysics*, **175**, 197-220.
- Ohnaka, M., Y. Kuwahara, and K. Yamamoto (1987). Constitutive relations between dynamic physical parameters near a tip of the propagating slip zone during stick-slip shear failure, *Tectonophysics*, **144**, 109-117.
- Ohnaka, M. and T. Yamashita (1989). A cohesive zone model for dynamic shear faulting based on experimentally inferred constitutive relation and strong motion source parameters. *J. Geophys. Res.*, **94**, 4089-4104.
- Okubo, P. G. (1989). Dynamic rupture modeling with laboratory-derived constitutive relations, *J. Geophys. Res.*, **94**, 12321-12355.
- Okubo, P. G. and J. H. Dieterich (1984). Effect of physical fault properties on friction instabilities produced on simulated faults, *J. Geophys. Res.*, **89**, 5817-5827.
- Okubo, P. G. and J. H. Dieterich (1986). State variable fault constitutive relations for dynamic slip, in: *Earthquake Source Mechanism*, S. Das, J. Boatwright, and C. Scholz, Editors, American Geophysical Union, Washington, D. C., 25-35.
- Olsen, K. B., and R. J. Archuleta (1996). Three-dimensional simulation of earthquakes on the Los Angeles faults system, *Bull. Seism. Soc. Am.* **86**, 575-596.
- Olsen, K. B., R. J. Archuleta, and J. R. Matarrese (1995). Magnitude 7.75 earthquake on the San Andreas fault: three-dimensional ground motion in Los Angeles, *Science* **270**, 1628-1632.
- Olsen, K.B., R. Madariaga, and R.J. Archuleta (1997). Three-dimensional dynamic simulation of the 1992 Landers earthquake, *Science*, **278**, 834-838.
- Olson, A. H. and R. J. Apsel (1982). Finite faults and inverse theory with applications to the 1979 Imperial Valley earthquake, *Bull. Seismol. Soc. Am.*, **72**, 1969-2001.
- Olson, A. H., J. A. Orcutt, and G. A. Frazier (1984). The discrete wavenumber finite element method of synthetic seismograms, *Geophys. J. R. Astr. Soc.*, **77**, 421-460.

- Otsuki, K., J. Minagawa, M. Aono, and M. Ohtake (1997). On the curved striations of Nojima seismic fault engraved at the 1995 Hyogoken-Nambu earthquake, Japan, *J. Seismol. Soc. Japan*, **49**, 451-460.
- Palmer, A.C. and J.R. Rice (1973). The growth of slip surfaces in the progressive failure of overconsolidated clay slopes, *Proc. R. Soc. London Ser. A* **332**, 527-548.
- Papageorgiou, A. S., and K. Aki (1983). A specific barrier model for the quantitative description of inhomogeneous faulting and the prediction of strong ground motion, I, Description of the model, *Bull. Seismol. Soc. Am.*, **73**, 693-722.
- Philip, H., and F. Megard (1977). Structural analysis of the superficial deformation of the 1969 Pariahuanca earthquakes (central Peru), *Tectonophys.*, **38**, 259-278.
- Pitarka, A., P. Somerville, Y. Fukushima, T. Uetake, and K. Irikura (2000). Simulation of near-fault strong-ground motion using Hybrid Green's functions, *Bull. Seism. Soc. Am.* **90**, 566-586.
- Quin, H. (1990). Dynamic stress drop and rupture dynamics of the October 15, 1979 Imperial Valley, California, earthquake, *Tectonophys.*, **175**, 93-117.
- Quin, H.R., and S.X. Das (1989). A hybrid boundary integral equation method for the computation of source time functions for 3D rupture propagation, *Geophys. J. R. Astr. Soc.*, **96**, 163-177.
- Reinen, L. A., and J. D. Weeks (1993). Determination of rock friction parameters using an iterative least squares inversion method, *J. Geophys. Res.*, **98**, 15937-15950.
- Rice, J.R. (1992). Fault stress states, pore pressure distributions, and the weakness of the San Andreas fault, in *Fault Mechanics and Transport Properties of Rocks*, B. Evans and T-F. Wong, eds., Academic Press, San Diego, 475-503.
- Rice, J.R., and A. L. Ruina (1983). Stability of steady frictional slipping, *J. Appl. Mech.* **50**, 343-349.
- Ruina, A. (1983). Slip instability and state variable friction laws, *J. Geophys. Res.* **88**, 10359-10370.
- Sharp, R. V., J. J. Lienkaemper, M. G. Bonilla, D. B. Burke, B. F. Fox, D. G. Herd, D. M. Miller, D. M. Morton, D. J. Ponti, M. J. Rymer, J. C. Tinsley, J. C. Yount, J. E. Kahle, E. W. Hart, and K. E.

- Sieh (1982). Surface faulting in the central Imperial Valley, The Imperial Valley, California, Earthquake, October 15, 1979, *U. S. Geol. Surv. Prof. Pap.*, **1254**, 119-144.
- Scholz, C.H. (1988). The critical slip distance for seismic faulting, *Nature*, **336**, 761-763.
- Scholz, C.H. (1990). The mechanics of earthquakes and faulting, *Cambridge Univ. Press*.
- Shibazaki, B., and M. Matsu'ura (1998). Transition process from nucleation to high-speed rupture propagation; scaling from stick-slip experiments to natural earthquakes, *Geophysical Journal International*, **132**, 14-30.
- Sleep, N.H. (1997). Application of a unified rate and state friction theory to the mechanics of fault zones with strain localization, *J. Geophys. Res.*, **102**, 2875-2895.
- Somerville, P. G., N. F. Smith, R. W. Graves, and N. A. Abrahamson, (1997). Modification of empirical strong ground motion attenuation relations to include the amplitude and duration effects of rupture directivity, *Seism. Res. Lett.* **68**, 199-222.
- Somerville, P. G., K. Irikura, R. Graves, S. Sawada, D. Wald, N. Abrahamson, Y. Iwasaki, T. Kagawa, N. Smith, and A. Kowada (1999). Characterizing crustal earthquake slip models for the prediction of strong ground motion, *Seism. Res. Lett.* **70**, 59-80.
- Spudich, P. (1992). On the inference of absolute stress levels from seismic radiation, *Tectonophys.*, **211**, 99-106.
- Spudich, P., and R. J. Archuleta (1987). Techniques for earthquake ground-motion calculation with applications to source parameterization of finite faults, in *Seismic strong motion synthetics*, editor B.A. Bolt, Academic Press, Inc.
- Spudich, P., and J. Boatwright (1990). Dynamically consistent inversions of earthquake ground motion data to infer fault constitutive laws, Abstract with program, International Symposium on Earthquake Source Physics and Earthquake Prediction, Tokyo, Japan, 151-154.
- Spudich, P., and E. Cranswick (1984). Direct observation of rupture propagation during the 1979 Imperial Valley earthquake using a short baseline accelerometer array, *Bull. Seismol. Soc. Am.*, **74**, 2083-2114.

- Spudich, P., M. Guatteri, K. Otsuki, and J. Minagawa (1998). Use of fault striations and dislocation models to infer tectonic shear stress during the 1995 Hyogo-ken Nanbu (Kobe) earthquake, *Bull. Seismol. Soc. Am.*, **88**, 413-427.
- Steidl, J. H., R. J. Archuleta, and S. H. Hartzell (1991). Rupture history of the 1989 Loma Prieta, California earthquake, *Bull. Seismol. Soc. Am.*, **81**, 1573-1602.
- Toda, S., R.S. Stein, P.A. Reasenberg, J.H. Dieterich, and A. Yoshida (1998). Stress transferred by the 1995 Mw = 6.9 Kobe, Japan, shock: Effect on aftershocks and future earthquake probabilities, *J. Geophys. Res.*, **103**, 24543-24565.
- Tse, S.T., and J.R. Rice (1986). Crustal earthquake instability in relation to the depth variation of frictional slip properties, *J. Geophys. Res.*, **91**, 9452-9472.
- Tsukahara, H., R. Ikeda, and K. Omura (1996). In-situ stress measurement in an earthquake focal area, *Tectonophys.*, **262**, 281-290.
- Tsukahara, H., R. Ikeda, and M. Ando (1997). Stress state of the Arima-Takatsuki-Rokko fault zone, (3) results at Nojima-Ogura, Abstracts of Japan Earth and Plan. Sci. Joint Meeting, 16
- Tsutsumi, A., and T. Shimamoto (1997). High-velocity frictional properties of gabbro, *Geophysical Research Letters*, **24**, 699-702.
- Virieux, J. and R. Madariaga (1982). Dynamic faulting studied by a finite difference method, *Bull. Seismol. Soc. Am.*, **72**, 345-369.
- Wald, D. J. (1996). Slip history of the 1995 Kobe, Japan, earthquake determined from strong motion, teleseismic, and geodetic data, *J. Phys. Earth*, **44**, 489-503.
- Wald, D. J. and T. H. Heaton (1994). Spatial and temporal distribution of slip for the 1992 Landers, California earthquake, *Bull. Seismol. Soc. Am.*, **84**, 668-691.
- Wald, D. J., D. V. Helmberger, and T. H. Heaton (1991). Rupture model of the 1989 Loma Prieta earthquake from the inversion of strong motion and broadband teleseismic data, *Bull. Seismol. Soc. Am.*, **81**, 1540-1572.

- Weeks, J.D., and T.E. Tullis (1985). Frictional sliding of dolomite; a variation in constitutive behavior, *J. Geophys. Res.*, **90**, 7821-7826.
- Weisberg, S. (1985). Applied linear regression, *Wiley, New York*.
- Yoshida, S., K. Koketsu, B. Shibasaki, T. Sagiya, T. Kato, and Y. Yoshida (1996). Joint inversion of near- and far-field waveforms and geodetic data for the rupture process of the 1995 Kobe earthquake, *J. Phys. Earth*, **44**, 437-454.
- Zhao, D. H. Kanamori, H. Negishi, and D. Wiens (1996). Tomography of the source area of the 1995 Kobe earthquake; evidence for fluids at the hypocenter, *Science*, **274**, 1891-1894.
- Zoback, M. D., and G. C. Beroza (1993). Evidence for near-frictionless faulting in the October 17, 1989 (M=6.9) Loma Prieta, California earthquake and its aftershocks, *Geology*, **21**, 181-185, 1993.